ELUCIDATING THE PUMPING MECHANISM OF BACTERIORHODOPSIN USING DYNAMIC NUCLEAR POLARIZATION ENHANCED MAGIC ANGLE SPINNING NMR

by

Qing Zhe Ni

B.S., Chemistry (2010)
Florida State University

Submitted to the Department of Chemistry
in Partial Fulfillment of the Requirement for the Degree of
Doctor of Philosophy in Chemistry

at the
Massachusetts Institute of Technology
February 2018

© 2018 Massachusetts Institute of Technology. All rights reserved

Signature of Author_ Signature redacted
Department of Chemistry
November 21, 2017

Certified by_____ Signature redacted
Robert G. Griffin
Arthur Amos Noyes Professor of Chemistry
Thesis Supervisor

Accepted by_____ Signature redacted
Robert W. Field
Haslam and Dewey Professor of Chemistry
Chairman, Department Committee on Graduate Students

MASSACHUSETTS INSTITUTE OF TECHNOLOGY
APR 13 2018
LIBRARIES
ARCHIVES

This doctoral thesis has been examined by a committee of the department of chemistry as follows:

Professor Troy Van Voorhis___ Signature redacted _____
Chairman

Professor Robert G. Griffin_____ Signature redacted _____
Thesis Supervisor

Professor Robert W. Field_____ Signature redacted _____
Thesis Committee Member

Elucidating the Pumping Mechanism of Bacteriorhodopsin Using Dynamic Nuclear Polarization Enhanced Magic Angle Spinning NMR

by

Qing Zhe Ni
Submitted to the Department of Chemistry
on December 16th, 2017 in Partial Fulfillment of the Requirement for the
Degree of Doctor of Philosophy in Chemistry

Abstract

Bacteriorhodopsin (bR) is comprised of 7 trans-membrane helices that enclose a retinylidene chromophore formed by a Schiff base (SB) between the retinal and Lys216. Due to bR's relative availability, it serves as a model for other members of the rhodopsin family, ion channels and GPCRs. Since its discovery in the 1970's, bR has been intensely studied by various methods including: X-ray crystallography, EM, FT-IR, molecular simulations, and NMR, etc. Despite numerous advances, details of its pump mechanism remain elusive due to experimental limitations in sensitivity and/or resolution. Here, dynamic nuclear polarization (DNP) is employed to boost the ^{1}H NMR signal. With an enhancement of 75, multidimensional spectra of low gyromagnetic nuclei were made possible. The cryogenic experimental temperature also traps the various bR photocycle intermediates, allowing them to be studied in situ. We are able to answer the one lingering question regarding bR's primary proton transfer pathway and conduct distance measurements near the active site.

The pathway of bR's primary proton transfer has been the subject of scrutiny for many years. DNP MAS NMR bond length measurements of the SB proton reveal an elongated N-H bond in L, the transfer of ^{1}H in deprotonated M_0, and a tight N-H bond in N intermediate. The ^{1}H chemical shift of ~3.6 ppm in M_o indicates an alcohol hydrogen donor partner. This strongly supports the SB H^+ being relayed from the SB to Asp85 via Thr89 as the pathway for bR's primary proton transfer.

Distance measurements obtained here are the first set of long-range DNP MAS NMR measurements conducted on a uniformly labeled bR system. We find that the SB-D85 distance shrinks in the first half of the photocycle and is released after the primary proton transfer. The decrease in distance between the two indicates helix C and helix G are moving toward each other, which could be the reason why functional L is difficult to achieve. The subsequent release of helix G provides an additional gate to the release of the torsion energy in the chromophore. Meanwhile, the SB-D212 distance hardly changes.

Thesis Supervisor: Robert G. Griffin
Title: Professor of Chemistry and Director of the Francis Bitter Magnet Laboratory

Dedicated to my boy, Brighton Nicholas Can and my grandmother Chen Xiang Zi.

Acknowledgements

I would like to thank my thesis advisor, Robert Griffin, for his guidance and support over the years. His passion for science and tenacious work ethic has shaped me as a scientist. The plethora research opportunities at the Bitter have made my years at MIT very exciting. Rather than being hesitant of the unfamiliar, the environment trains one to take chances when new ideas arise and acquires the skillsets needed to be an independent scientist. A big part of my thesis was under the guidance of Dr. Judith Herzfeld. Her attention to detail and her ability decipher data and correlate them to the mechanism of a protein is truly amazing. As a female scientist, she resembles many of the qualities that I strive to have. Due to all these influences, I have been trained to handle all the different aspects of a research project, from designing and performing experiments to analyzing data and writing papers. Part of being at the Francis Bitter laboratory allowed me to gain a lot of experiences with both the hardware and software of DNP/NMR and using this technique to answer relevant questions that would be impossible otherwise.

My husband, Thach Can (Cody), has been my rock from the first day we met. I thank him for always being there with a kind and helping heart. His quantitative mindset is complementary to my scientific approach and ardor for arts and music. We went from classmates who did QM psets together to best friends and more. I am thankful for the arrival of our son and all the joy and laughter he has bestowed upon us. Lily, our precious little 5lbs Pomeranian, is my and many others' ray or sunshine. Her innocence and fun loving nature makes her a blessing to anyone who comes across her path. I would like to thank my parents, it wasn't easy to leave everything behind and embark on a journey of the unknown to the United States. Robert Davison, a dear friend to the family, thank you for your kindness and support.

I had the privilege to work with many talented scientists. Coworkers whom had a positive influence on me: Eugenio Daviso, Christry George, Robert Silvers, Yongchao Su, Salima Bahri, Alexander Barnes, Evgeny Markhasin, Loren Andreas, Michael Colvin, Kevin Donovan, Matthew Eddy, Kong Ooi Tan, Chen Yang, Marcel Reese, Marvin Bayro, and Bjorn Corzilius. In particular, I would like to thank the following members: Eugenio for working days and nights on the instrumentation, even when things got tough, we kept on going as a team. Together we were able to bring the instrumentation to the point it is now, a fully operational DNP MAS NMR that provides the highest enhancements ever reported.

Xander for reaching out to me my first year and introducing me to the 250GHz/380MHz instrumentation. Jeff Byrant, Ajay Thakkar, Mike Mullins are the technical staff who has helped with the troubleshooting every part of the 250GHz/380MHz. Sudheer Jawla, Bill Guss, Ivan Mastovsky and Richard Temkin for they everlasting support with the gyrotron. Jillian Haggerty (Jill) is a wonderful lady who has been absolutely amazing to me all these years.

Table of Contents

List of Figures

Chapter 1: Introduction

1.1 Motivation

In structural biology, membrane proteins are gateways to cells. They serve as the entry and exit for ions, nutrients, drugs, waste products, proteins and DNA. They are also responsible for the communication between cells and their environments. Any mutations can result in diseases such as: heart disease where malfunctioning ion channels plays a role, cystic fibrosis caused by mutations in the cystic fibrosis transmembrane conductance regulator chloride ion channel. While 30% of the human genome codes for membrane proteins, little is known about them. Membrane proteins are difficult to study because they become unstable once extracted from their native environments and are challenging to crystallize for X-ray crystallography studies. Solution NMR is a useful technique for solving the structure of small proteins, but it is limited to small molecules due to an increase in linewidth as a result of slower tumbling rate.

Solid state NMR is the powerful method of choice for the study of many biological systems in their native environment including membrane proteins. Due to its similar homology and relative stability, Bacteriorhodopsin (bR) is an ideal model for members of the rhodopsin family as well as for GPCRs, an important class of membrane proteins that functions as signaling and cellular response. Understanding a biological system goes far beyond the structure of a protein, it seeks for answers to functionalities.

Studies of bR using solid state NMR started in the 1980's mainly by Griffin and Herzfeld.(1-5) Many questions to bR's function were answered, for example, the configuration of the retinal was determined by the use the dihederal angle measurements.(6) Different photocycle intermediates were successfully trapped and examined in situ.(7-10) Presence of complex counterion was established from ^{15}N chemical shifts of the intermediates. Many of the results from MAS NMR were complimentary to results reported from X-ray crystallography, FT IR, EM and molecular simulations.(11-20) It came to a period where in order to dive deeper into the investigation of bR, advancements in technology are needed to boost the NMR sensitivity and improve the resolution of the data. The low sensitivity of NMR can be circumvented by the addition of dynamic nuclear polarization (DNP). (21, 22) DNP was developed in Griffin's group at MIT and for the past decade, it has expanded commercially worldwide.(23-31) In DNP, the large polarization of the electron is transferred to the protons of the system, resulting in the NMR signal being enhanced. The

boost in sensitivity translated into months of savings in acquisition time. Concurrently, new developments in probes, spectrometer hardware has led MAS NMR to higher fields and to faster spinning rates. With the advantages offered from DNP MAS NMR, we are able to tackle the remaining mysterious in bR. In the following chapters applies DNP NMR methodology to gain insight into the function of bR through distance measurements with dipolar recoupling and ^{1}H local environments at the active site.

1.2 Thesis outline

My PhD has focused mainly on novel applications of dynamic nuclear polarization (DNP) at higher fields, and using this technology to understand something that would be impossible otherwise, even though improving technical details on the side was unavoidable. We start with introductory **Chapter 2** that goes over what DNP is, how it works, and the latest research that is being done in the field.(23, 32) In **Chapter 3**, we investigate how $^{13}CH_3$ and $-^{15}NH_3^+$ signals disappear due to the interference of the molecular motions with the ^{1}H decoupling at a broad range of temperatures (77K to 300K), with a special emphasize around DNP experimental temperatures.(33) We investigate the effect of these dynamic processes on the NMR lineshapes and signal intensities in several systems: (1) microcrystalline APG, (2) membrane protein bR, (3) amyloid fibrils PI3-SH3, (4) monomeric alanine–CD_3 and (5) the protonated and deuterated dipeptide N-Ac-VL over 78-300 K. In APG, the 3-site hopping of the Ala-C_β peak disappears completely at 112 K, concomitant with the attenuation of CP signals from other ^{13}C's and ^{15}N's. In bR and PI3-SH3, the methyl groups are attenuated at ~95 K while all other ^{13}C's remain unaffected. ^{2}H labeling can assist with recovering the spectral intensity.

Chapter 4 and **Chapter 5** are focused on understanding the ion motive pumping mechanism of the membrane protein, Bacteriorhodopsin using DNP MAS NMR. Despite numerous studies by different techniques, details of the bR pump mechanism remain elusive. DNP NMR experiments are done at cryogenic temperatures, which also trap the various bR photocycle intermediates, allowing them to be studied in situ. Distance measurements obtained from 3D fs-REDOR. Schiff base (SB)-D85 distance, **Chapter 4**, shrinks in the first half of the photocycle and is released after the primary proton transfer. The decrease in distance between the two indicates helix C and helix G are moving toward each other. The subsequent release of helix G provides an additional gate to the release of the torsion energy in the chromophore. Meanwhile, the SB-D212 distance hardly changes.

One question remains unanswered is bR's primary proton transfer pathway presented in **Chapter 5**. Here we study bR's active site in the various intermediates of the photocycle. The active site is comprised of a retinylidene chromophore that interacts via its SB with nearby water molecules and amino acid residues. Bond length measurements of the SB proton reveal an elongated N-H bond in L, the transfer of ^{1}H in deprotonated M_0, and a tight N-H bond in N intermediate. The ^{1}H chemical shift of ~3.6 ppm in M_0 indicates an alcohol hydrogen donor partner. This strongly supports the H^{+} being relay from the SB to Asp85 via Thr89 as the pathway for bR's primary proton transfer.

Lastly, **Chapter 6** describes the studies of pharmaceutical formulations using DNP MAS NMR. MAS should be widely applicable to studies of the structure of active pharmaceutical ingredients (API) and formulations.(34) However, the low sensitivity encountered in spectroscopy of natural abundance APIs present at low concentration has limited the success of MAS experiments. Here, we demonstrate that DNP polarizing agents can be added *in*-situ during the preparation of amorphous solid dispersions (ASDs) via spray drying and hot-melt extrusion so that ASDs can be examined during drug development.

1.3 References

1. Herzfeld J & Berger AE (1980) SIDEBAND INTENSITIES IN NMR-SPECTRA OF SAMPLES SPINNING AT THE MAGIC ANGLE. *Journal of Chemical Physics* 73(12):6021-6030.
2. Harbison GS, *et al.* (1984) Dark-Adapted Bacteriorhodopsin Contains 13-Cis,15-Syn and All-Trans,15-Anti Retinal Schiff-Bases. *Proceedings of the National Academy of Sciences of the United States of America-Biological Sciences* 81(6):1706-1709.
3. Lugtenburg J, *et al.* (1986) Mechanism for the Opsin Shift of Retinals Absorption in Bacteriorhodopsin. *J. Am. Chem. Soc.* 108(11):3104-3105.
4. Degroot HJM, Harbison GS, Herzfeld J, & Griffin RG (1989) Nuclear Magnetic-Resonance Study of the Schiff-Base in Bacteriorhodopsin - Counterion Effects on the N-15 Shift Anisotropy. *Biochemistry* 28(8):3346-3353.
5. McDermott AE, *et al.* (1991) Mechanism of Proton Pumping in Bacteriorhodopsin by Solid-State NMR - The Protonation State of Tyrosine in the Light-Adapted and M-States. *Biochemistry* 30(34):8366-8371.
6. Lansing JC, *et al.* (2002) Chromophore distortions in the bacteriorhodopsin photocycle: Evolution of the H-C14-C15-H dihedral angle measured by solid- state NMR. *Biochemistry* 41(2):431-438.
7. Hu JGG, Sun BQQ, Petkova AT, Griffin RG, & Herzfeld J (1997) The predischarge chromophore in bacteriorhodopsin: A N-15 solid-state NMR study of the L photointermediate. *Biochemistry* 36(31):9316-9322.
8. Hu JGG, Griffin RG, & Herzfeld J (1997) Interactions between the protonated Schiff base and its counterion in the photointermediates of bacteriorhodopsin. *J. Am. Chem. Soc.* 119(40):9495-9498.
9. Hu JG, *et al.* (1998) Early and late M intermediates in the bacteriorhodopsin photocycle: A solid-state NMR study. *Biochemistry* 37(22):8088-8096.
10. Petkova AT, *et al.* (1999) Arginine activity in the proton-motive photocycle of bacteriorhodopsin: Solid-state NMR studies of the wild-type and D85N proteins. *Biochemistry* 38(5):1562-1572.
11. Rothschild KJ, Zagaeski M, & Cantore WA (1981) Conformational changes of bacteriorhodopsin detected by Fourier transform infrared difference spectroscopy. *Biochem. Biophys. Res. Commun.* 103(2):483-489.
12. Eisenstein L, *et al.* (1987) FTIR difference studies on apoproteins. Protonation states of aspartic and glutamic acid residues during the photocycle of bacteriorhodopsin. *J. Am. Chem. Soc.* 109(22):6860-6862.
13. Roepe P, *et al.* (1988) FTIR Evidence for Tryptophan Perturbations During the Bacteriorhodopsin Photocycle. *J. Am. Chem. Soc.* 110(21):7223-7224.
14. Grigorieff N, Ceska TA, Downing KH, Baldwin JM, & Henderson R (1996) Electron-crystallographic Refinement of the Structure of Bacteriorhodopsin. *J. Mol. Biol.* 259(3):393-421.
15. Luecke H, Schobert B, Richter H-T, Cartailler J-P, & Lanyi JK (1999) Structure of bacteriorhodopsin at 1.55 Å resolution *J. Mol. Biol.* 291(4):899-911.
16. Bondar AN, Fischer S, Smith JC, Elstner M, & Suhai S (2004) Key role of electrostatic interactions in bacteriorhodopsin proton transfer. *J. Am. Chem. Soc.* 126(44):14668-14677.
17. Bondar AN, Elstner M, Suhai S, Smith JC, & Fischer S (2004) Mechanism of primary proton transfer in bacteriorhodopsin. *Structure* 12(7):1281-1288.
18. Bondar AN, Suhai S, Fischer S, Smith JC, & Elstner M (2007) Suppression of the back proton-transfer from Asp85 to the retinal Schiff base in bacteriorhodopsin: A theoretical analysis of structural elements. *Journal of Structural Biology* 157(3):454-469.
19. Bondar AN, Baudry J, Suhai S, Fischer S, & Smith JC (2008) Key Role of Active-Site Water Molecules in Bacteriorhodopsin Proton-Transfer Reactions. *Journal of Physical Chemistry B* 112(47):14729-14741.
20. Bondar AN (2009) BACTERIORHODOPSIN PROTON PUMPING MECHANISM: INSIGHTS FROM COMPUTER SIMULATIONS. *Revue Roumaine De Chimie* 54(6):433-439.

21. Mak-Jurkauskas ML, *et al.* (2008) Energy transformations early in the bacteriorhodopsin photocycle revealed by DNP-enhanced solid-state NMR. *Proc. Natl. Acad. Sci. U. S. A.* 105(3):883-888.
22. Bajaj VS, Mak-Jurkauskas ML, Belenky M, Herzfeld J, & Griffin RG (2009) Functional and shunt states of bacteriorhodopsin resolved by 250 GHz dynamic nuclear polarization-enhanced solid-state NMR. *Proceedings of the National Academy of Sciences* 106(23):9244-9249.
23. Ni QZ, *et al.* (2013) High Frequency Dynamic Nuclear Polarization. *Acc. Chem. Res* 46(9):1933-1941.
24. Akbey U & Oschkinat H (2016) Structural biology applications of solid state MAS DNP NMR. *J. Magn. Reson.* 269:213-224.
25. Becker-Baldus J, *et al.* (2015) Enlightening the photoactive site of channelrhodopsin-2 by DNP-enhanced solid-state NMR spectroscopy. *Proceedings of the National Academy of Sciences* 112(32):9896-9901.
26. Cheng CY & Han SI (2013) Dynamic Nuclear Polarization Methods in Solids and Solutions to Explore Membrane Proteins and Membrane Systems. *Annual Review of Physical Chemistry, Vol 64,* Annual Review of Physical Chemistry, eds Johnson MA & Martinez TJ), Vol 64, pp 507-532.
27. Fernandez-de-Alba C, *et al.* (2015) Matrix-Free DNP-Enhanced NMR Spectroscopy of Liposomes Using a Lipid-Anchored Biradical. *Chemistry-a European Journal* 21(12):4512-+.
28. Fricke P, *et al.* (2016) High resolution observed in 800 MHz DNP spectra of extremely rigid type III secretion needles. *J. Biomol. NMR* 65(3-4):121-126.
29. Gupta R, *et al.* (2016) Dynamic Nuclear Polarization Enhanced MAS NMR Spectroscopy for Structural Analysis of HIV-1 Protein Assemblies. *Journal of Physical Chemistry B* 120(2):329-339.
30. Jakdetchai O, *et al.* (2014) Dynamic Nuclear Polarization-Enhanced NMR on Aligned Lipid Bilayers at Ambient Temperature. *J. Am. Chem. Soc.* 136(44):15533-15536.
31. Kaplan M, *et al.* (2015) Probing a cell-embedded megadalton protein complex by DNP-supported solid-state NMR. *Nat. Methods* 12(7):649-+.
32. Can TV, Ni QZ, & Griffin RG (2015) Mechanisms of dynamic nuclear polarization in insulating solids. *J. Magn. Reson.* 253:23-35.
33. Ni QZ, *et al.* (2017) Peptide and Protein Dynamics and Low-Temperature/DNP Magic Angle Spinning NMR. *J. Phys. Chem. B* 121(19):4997-5006.
34. Ni QZ, *et al.* (2017) In Situ Characterization of Pharmaceutical Formulations by Dynamic Nuclear Polarization Enhanced MAS NMR. *J. Phys. Chem. B* 121(34):8132-8141.

Chapter 2: High Frequency Dynamic Nuclear Polarization

Adapted from Q.Z. Ni, E. Daviso, Thach V. Can, Evgeny Markhasin, Sudheer K. Jawla, Timothy M. Swager, Richard J. Temkin, Judith Herzfeld and Robert G. Griffin, Accounts of Chemical Research 46 (2013) 1933-1941

During the three decades 1980-2010, magic angle spinning (MAS) NMR has developed into the method of choice to examine many chemical, physical and biological problems. In particular, a variety of dipolar recoupling methods to measure distances and torsion angles can now constrain molecular structures to high resolution. However, applications are often limited by the low sensitivity of the experiments, due in large part to the necessity of observing spectra of low-g nuclei such as the I = ½ species ^{13}C or ^{15}N. The difficulty is still greater when quadrupolar nuclei, such as ^{17}O or ^{27}Al, are involved. This problem has stimulated efforts to increase the sensitivity of MAS experiments. A particularly powerful approach is dynamic nuclear polarization (DNP) which takes advantage of the higher equilibrium polarization of electrons (which conventionally manifests in the great sensitivity advantage of EPR over NMR). In DNP, the sample is doped with a stable paramagnetic polarizing agent and irradiated with microwaves to transfer the high polarization in the electron spin reservoir to the nuclei of interest. The idea was first explored by Overhauser and Slichter in 1953. However, these experiments were carried out on static samples, at magnetic fields that are low by current standards. To be implemented in contemporary MAS NMR experiments, DNP requires microwave sources operating in the subterahertz regime — roughly 150-660 GHz — and cryogenic MAS probes. In addition, improvements were required in the polarizing agents, because the high concentrations of conventional radicals that were required to produce significant enhancements compromise spectral resolution.

In the last two decades scientific and technical advances have addressed these problems and brought DNP to the point where it is achieving wide applicability. These advances include the development of high frequency gyrotron microwave sources operating in the subterahertz frequency range. In addition, low temperature MAS probes were developed that permit in-situ microwave irradiation of the samples. And, finally, biradical polarizing agents were developed that increased the efficiency of DNP experiments by factors of ~4 at considerably lower paramagnet concentrations than required with monoradicals. Collectively these developments have made it possible to apply DNP to a number of different scientific problems, most prominently in the biological and material sciences, and achieve signal enhancements of ~100 on a routine basis. This Account

reviews these developments, including the primary mechanisms used to transfer polarization in high frequency DNP, and the current choice of microwave sources and biradical polarizing agents. In addition, we illustrate the utility of the technique with a description of applications to membrane and amyloid proteins that emphasizes the unique structural information that is available in these two cases.

2.1. Introduction

Magic angle spinning (MAS) nuclear magnetic resonance (NMR) has emerged as a powerful, nondestructive method that can be used to characterize the structure and dynamics of systems that are not accessible by either solution NMR or crystallography. In particular, the last three decades have witnessed the development of MAS techniques to probe various anisotropic interactions at the molecular and atomic scale via dipole recoupling techniques [1]. As a consequence, it is possible to measure internuclear distances in amorphous and powder samples as well as in crystals. In principle, these measurements provide copious high resolution information about the structure and dynamics of a variety of biological systems such as peptides [2], membrane proteins [3-5], nanocrystals [6], amyloids [7-10], and materials science. Given this versatility, the recent rapid expansion of MAS NMR is expected to continue.

Despite the outstanding progress in this field, there remains an acute sensitivity problem since MAS NMR usually involves direct detection of ^{13}C, ^{15}N or another low-g species. Cross polarization (CP) techniques and operation at higher magnetic fields have helped to address this issue. However, significantly higher sensitivity would help to bring MAS NMR into a regime where it is truly widely applicable. The subject of this Account is recent 10^2-10^3 fold improvements in MAS NMR sensitivity based on high frequency dynamic nuclear polarization (DNP). As we will see, high frequency DNP is significantly changing the landscape of what is possible with MAS NMR. This article illustrates this point with a discussion of polarization transfer mechanisms, polarizing agents, instrumentation, and recent applications of MAS DNP to complex heterogeneous systems.

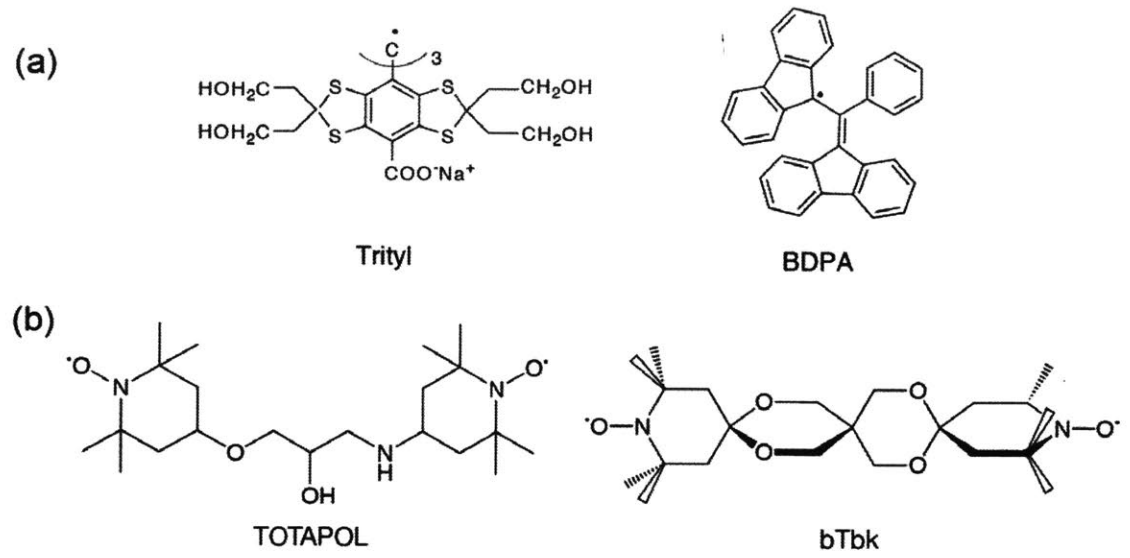

Figure 2.1: Polarizing agents commonly used for high field DNP experiments. (a) narrow line radicals trityl and BDPA used for the SE; (b) TEMPO based biradicals TOTAPOL and bis-TEMPO-bis-ketal (bTbk) used for the CE.

2.2. DNP Mechanism

DNP enhances NMR signals by transferring the large polarization of electrons to nearby nuclei via microwave (μw) irradiation of electron-nuclear transitions [11]. Contemporary MAS DNP experiments on *insulating* solids are usually based either on the solid effect (SE), coupling an electron-nuclear spin pair, or the cross effect (CE), utilizing a pair of electrons in the form of a biradical and a nuclear spin. A third mechanism, thermal mixing (TM), involves multiple electrons and a homogeneously broadened EPR spectrum. However, at the high fields and low temperatures (80-110 K) currently used in MAS experiments, TM has thus far not provided an important polarization pathway. In all of these mechanisms it is necessary to add a stable paramagnetic polarizing agent to the sample and the most commonly used radicals are shown in Figure 2.1. Trityl and BDPA (or water soluble BDPA [12]) support the SE, whereas the TEMPO based biradicals TOTAPOL[13] and bTbk[14] are used for the CE. The detailed polarization transfer schemes discussed below are closely linked to the shapes of the high field EPR spectra of these molecules.

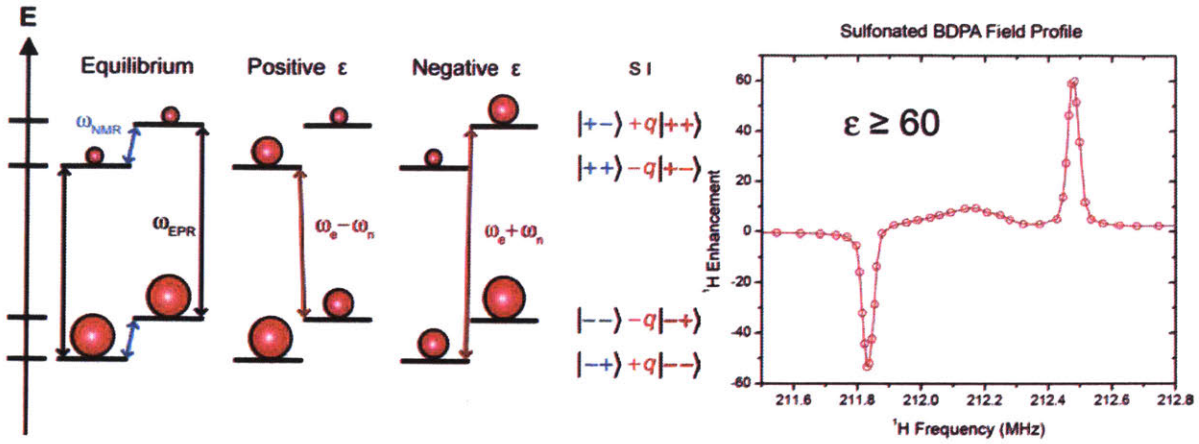

Figure 2.2: (*left*) Energy level diagram illustrating DNP via the solid effect (SE). At thermal equilibrium (*left*), populations are governed by the Boltzmann distribution. Mixing of states in the nuclear and electron spin subspaces (right), leads to partially allowed double quantum (DQ) and zero quantum (ZQ) transitions, and positive and negative enhancements, $\mathcal{E}$, respectively. The mixing of states is proportional to a constant *q*, which is inversely proportional to B_0. Therefore, the enhancement in the Solid Effect DNP scales as B_0^{-2}. (*right*) A plot of the enhancement from SA-BDPA[12] as a function of magnetic field (^{1}H frequency) showing the positive and negative enhancements. ω_{NMR} and ω_{EPR} are the NMR and EPR frequencies and $\omega_e \pm \omega_n$ are the sum and difference of the EPR and NMR frequencies.

2.2.1. Solid Effect

The SE can be understood using a two-spin model involving one electron and one nucleus, interacting via an electron-nuclear dipole coupling, and irradiation at nominally forbidden electron transitions at $\omega_{\mu w} = \omega_{0S} \pm \omega_{0I}$ illustrated in Figure 2.2. The Hamiltonian applicable to the two spin system is

$$\hat{H} = \omega_{OS}\hat{S}_z - \omega_{OI}\hat{I}_z + C\hat{S}_z\hat{I}_+ + C^*\hat{S}_z\hat{I}_- \qquad (2.1.1)$$

where ω_{0S} and ω_{0I} are the electron and nuclear Larmor frequencies, respectively, $C = (-3/2)(\gamma_S\gamma_I / r_{IS}^3)\sin\theta\cos\theta e^{-i\theta}$ is the usual term in the electron-nuclear dipole Hamiltonian [16] and ***S*** and ***I*** are spin operators for electrons and nuclei, respectively. First order perturbation theory yields the mixed eigenstates shown in the figure where the mixing coefficient $q = C/\omega_{0I} \ll 1$. The other terms in the electron-nuclear dipolar Hamiltonian (*A, B, E* and *F* in Van Vleck notation) are also mix states, but the contributions are relatively small. Irradiation of the partially allowed transitions by μw's gives rise to either positive (double

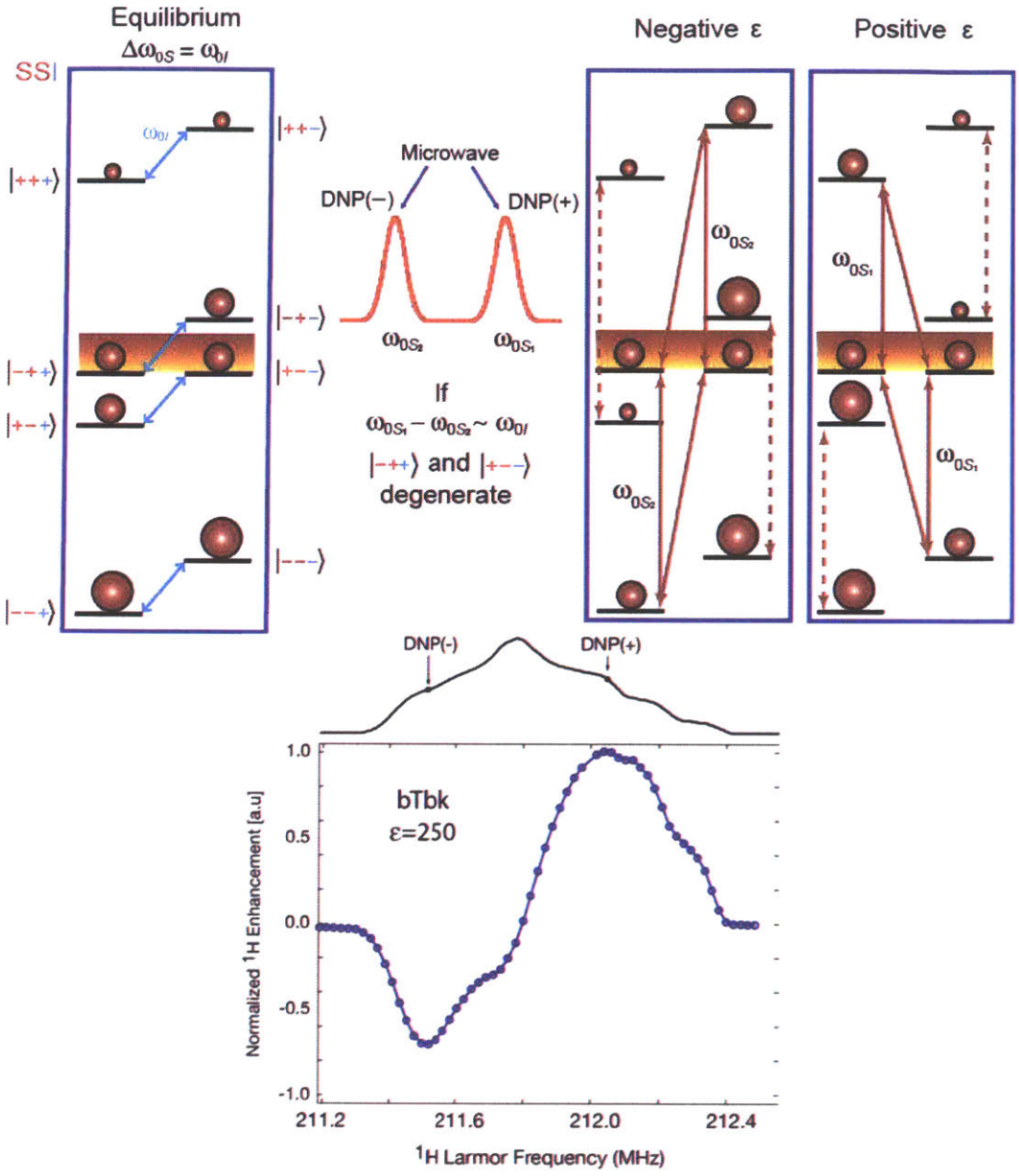

Figure 2.3: Energy diagram illustrating DNP via the CE. At equilibrium (left), under the matching condition, there is degeneracy and 1:1 population of the two shaded levels. The EPR spectrum of an ideal biradical for CE (middle) has two narrow lines separated by the nuclear Larmor frequency. Saturation of transitions near the first (second) EPR line gives rise to a positive (negative) DNP enhancement (right). (*bottom*) Field profile for bTbk with an enhancement $\varepsilon = 250$[14]

quantum) or negative (zero quantum) enhancement of the nuclear polarization as illustrated on the right of Figure 2.2.

The SE is the dominant DNP mechanism in systems where the polarizing agent exhibits a homogeneous EPR linewidth (δ) and an inhomogeneous spectral breadth (Δ) smaller than the nuclear Larmor frequency ($\delta,\Delta < \omega_{0I}$). This condition is satisfied by radicals with high molecular symmetry such as BDPA[17], SA-BDPA[12], and trityl OX063[18], where the g tensors are nearly isotropic and the hyperfine interaction is small. However, as the SE relies on the mixing of nuclear states by electron-nuclear coupling, the enhancement scales as ω_{0I}^{-2}. Therefore, the SE becomes less efficient at high magnetic fields (> 3 T). Nevertheless, recent research suggests that SE can be very efficient at high field provided that high microwave power, and a large $\omega_{1S} = \gamma_e B_{1S}$ is available. Enhancements as high as ~144 have been achieved at 5 T. Finally, the SE can also be the dominant mechanism when transition metals complexes, e.g. with Gd^{3+}, are used as polarizing agents. Since the broadening of the EPR line in these systems is mainly induced by the zero field splitting, the EPR line narrows at higher magnetic fields and metal-based polarizing agents may show improved performances at higher fields[19].

2.2.2. Cross effect

When $\Delta > \omega_{0I} > \delta$, DNP is governed by the CE and scales with ω_{0I}^{-1}, leading to larger enhancements at higher magnetic fields. At high fields, where the EPR spectrum is dominated by g-anisotropy and inhomogeneously broadened, a three spin quantum mechanical treatment is possible.[20-22] The Hamiltonian for the nuclear spin and two electrons is

$$\hat{H} = \omega_{0S_1} S_{1z} + \omega_{0S_2} S_{2z} - \omega_{0I} I_z + \left(A_1 S_{1z} + A_2 S_{2z}\right) I_z + \left(B_1 S_{1z} + B_2 S_{2z}\right) I_x + d\left(3 S_{1z} S_{2z} - \vec{S}_1 \bullet \vec{S}_2\right) - 2J\vec{S}_1 \bullet \vec{S}_2 \qquad (2.1.2)$$

where the first three terms represent electron and nuclear Zeeman interactions, the fourth and fifth describe the electron-nuclear coupling (with A and B denoting the secular and psuedosecular hyperfine couplings[23]), the sixth represents the electron-electron dipolar coupling and the last describes exchange coupling. This leads to the energy level diagram for the CE is shown in Figure 2.3, and electron-electron-nuclear polarization transfer is maximized when the central energy levels are degenerate. This occurs when the matching condition $\left|\omega_{OS_1} - \omega_{OS_2}\right| = \omega_{OI}$ is fulfilled, where ω_{OS_1} and ω_{OS_2} are the Larmor frequencies of dipolar coupled electrons S_1 and S_2. The degeneracy leads to saturation of the four

connected levels and enhanced nuclear polarization. A field profile obtained from bTbk is shown at the bottom of Figure 2.3, and roughly represents the negative 1st derivative of the EPR spectrum. Also shown are the positions in the EPR powder pattern that are irradiated for optimal positive and negative enhancements.

Initially, high-field CE DNP experiments were performed with mono-radical species, such as TEMPO[24, 25]. In this situation, the frequency matching condition is fulfilled only for the fraction of the radicals that adopt the correct relative orientation of their g-tensors. In order to improve CE DNP, we introduced biradicals such as bis-TEMPO-n-ethylene glycol (BTnE)[20] and TOTAPOL [13], consisting of two tethered TEMPO moieties to obtain relatively short (~12 Å) electron-electron distances independent of concentration. With these polarizing agents, which have an e-e dipole coupling of 20-30 MHz, the enhancements were ~4-fold higher at an ~4-fold lower e concentration. Figure 2.4 shows recent results obtained using TOTAPOL from two standard samples, urea and proline. The observed e=181 and e=134 are ~2-fold higher than we initially reported for TOTAPOL at this field [26] due to improvements in instrumentation – primarily gyrotron output power and lower temperatures (*vide infra*).

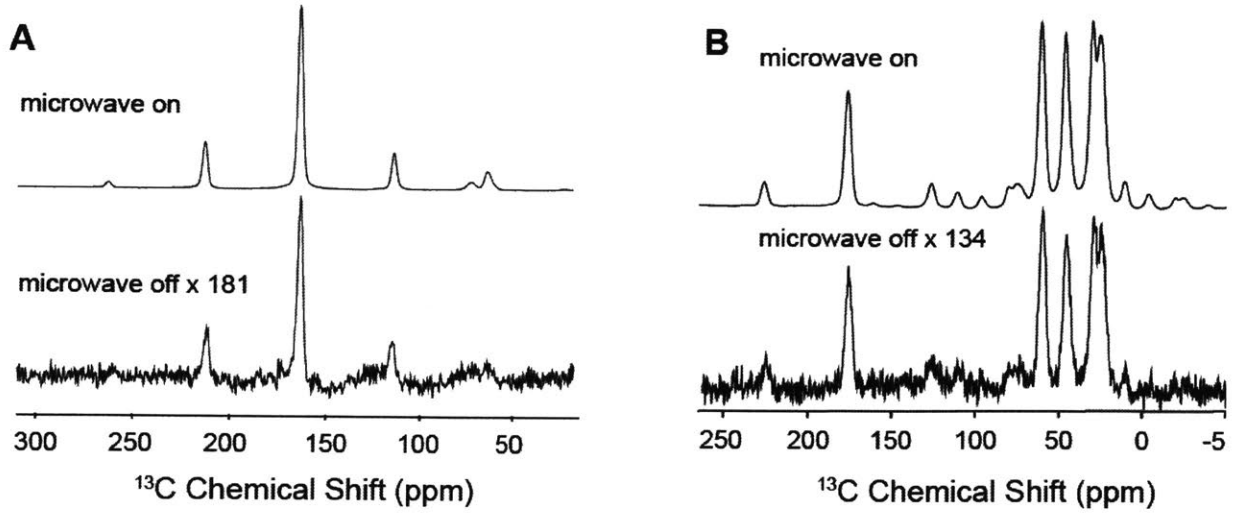

Figure 2.4: ^{13}C CP MAS NMR spectra of (A) 1M U-[^{13}C-^{15}N] urea and (B) 0.5 M U-[^{13}C-^{15}N] proline at 80 K with and without microwave irradiation. The DNP enhancements are e=181 and e=134, respectively. Both samples contained 10 mM TOTAPOL in a 60/30/10 ratio of d_8-glycerol/D_2O/H_2O. Experimental parameters are: 4 scans, recycle delay 4 s, microwave power ~12.5 W, $gB_1(^1H)$=83 kHz, $gB_1(^{13}C)$=71 kHz, $\omega_r/2\pi$ = 5 kHz.

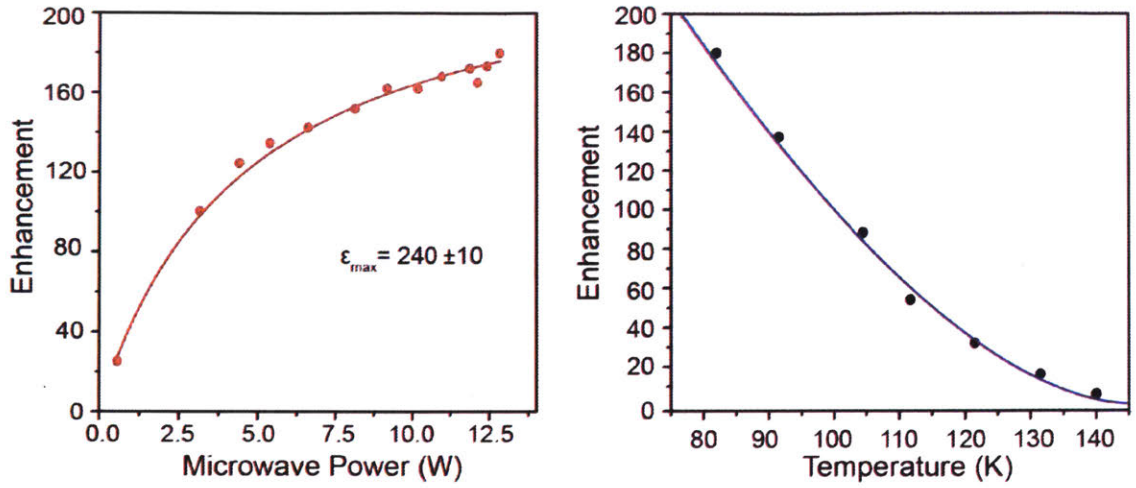

Figure 2.5: ^{13}C CP DNP enhancements of U-1M[^{13}C , ^{15}N] urea with 10 mM TOTAPOL plotted as a function of μw power at 80 K (*left*) and as a function of temperature at 12.5 W μw (*right*). $\omega_r/2\pi$ = 7 kHz.

2.3. Optimizing DNP Signal Enhancements

DNP enhancements are governed by a number of factors, including microwave power, concentration and design of the polarizing agent, temperature, solvent, and the relaxation times of the solvent and solute. We now review recent results aimed at optimizing the efficiency of DNP experiments with a focus on the influence of these parameters on the enhancements.

2.3.1 Microwave Power

Gyrotrons [17, 27, 28] are capable of producing 10's of watts of μw power with excellent frequency stability and low phase noise, making them the current microwave source of choice for DNP experiments. In particular, the low Q of the microwave circuit in the MAS NMR probe necessitates copious power to generate a sufficient B_1 to excite DNP transitions. Furthermore, since the gyrotron is a fast wave device, it can operate at high powers for extended periods of time, as is required for multidimensional NMR experiments that involve signal averaging. Figure 2.5 (left) shows the enhancement as a function of μw power at 80 K obtained with a frequency tunable 250 GHz gyrotron[29]. The enhancement increases with power, does not saturate at our maximum available power of 12.5 W, and extrapolates to a limiting value e_{max}~240. Similar dependences of e on μw power have been published elsewhere. [30, 31] An alternative microwave source, that we explored sometime ago and

currently in use in some labs[32], is a low power (~10-100 mW) Gunn diode. However, the enhancements are lower: on one sample, e ~25 with 10 mW from the Gunn diode versus e=185 with 1 W from the gyrotron[33]. Thus, the data in Figure 5 suggest that with current technology the gyrotron is the microwave source of choice for DNP experiments, especially at microwave/ ^{1}H NMR frequencies ≥ 263 GHz/400 MHz for e/^{1}H. Currently gyrotron-based DNP spectrometers are operating at microwave/ ^{1}H NMR frequencies up to 460 GHz/700 MHz[30] and are expected to go still higher. Nevertheless, microwave technology does improve with time, and it is possible that alternatives to the gyrotron and Gunn diode will be available in the future.

2.3.2 Temperature and polarizing agents

Both the sample temperature and the nature of the polarizing agent profoundly influence the DNP enhancements. Lower temperatures improve both the SE and CE enhancements, most likely due to longer electron and proton relaxation times. Figure 2.5 (*right*) plots recent data showing the temperature dependence of the ^{1}H DNP signal enhancement in the range 80-140 K at 250 GHz/380 MHz with the TOTAPOL/urea sample described above. Note that the DNP enhancement increases as the temperature approaches 80 K, by a factor of 3.6 in the range 110 to 80 K.

It is well known that high concentrations of paramagnets dramatically broaden NMR linewidths and attenuate integrated NMR signal intensities. It is for this reason that we developed biradical polarizing agents with a ~20-30 MHz intramolecular e-e dipole coupling which yield ~4-fold larger enhancements at ~4-fold lower electron concentration than monoradicals such as TEMPO[20]. Our experiments performed on urea, proline, bacteriorhodopsin (bR), and PI3-SH3 fibrils [34, 35]suggest that optimal radical concentration of TOTAPOL is 10-20 mM.

Finally, we note that biradicals such as bTbk[14] (Figure 2.1) and bTbk-py[36] have the TEMPO moieties locked at ~90° with respect to one another, and therefore yield a relative orientation of the two g-tensors that better satisfies the CE matching condition. These polarizing agents have produced enhancements as large as 250 (Figure 2.3).[14]

It was previously reported that ^{2}H labeled solvents improve ^{1}H DNP enhancements, and that even with 90-95% ^{2}H labeling we can still efficiently CP to low gamma nuclei in the target molecule.[20, 37] Thus, while ^{1}H dilution attenuates relaxation processes, even dilute

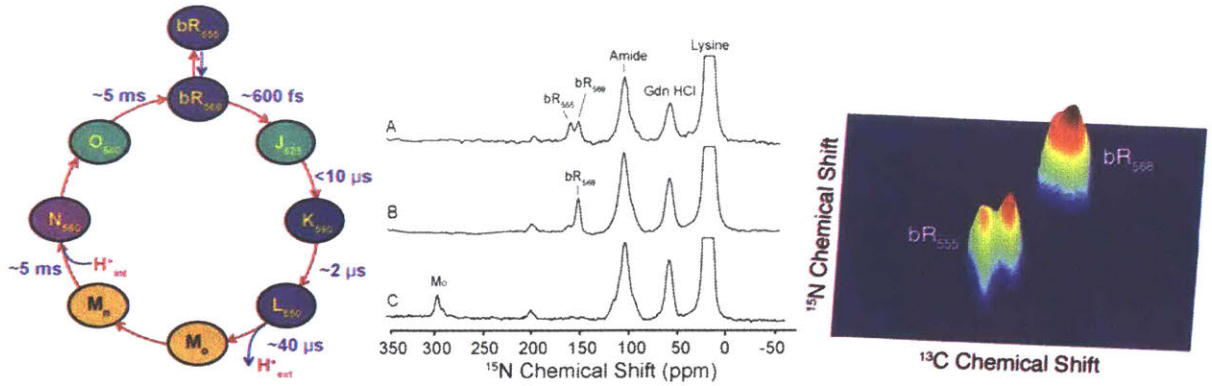

Figure 2.6: (*left*) The ion-motive photocycle of bR. The subscript for each intermediate represents the wavelength (in nm) of maximum visible absorption. (*middle*) ^{15}N CP DNP spectra [ζ-^{15}N-Lys] bR prepared with 15 mM TOTAPOL in 60/30/10 volume ratio of d_8-glycerol/D_2O/H_2O in 0.3 M guanidinium hydrochloride at pH 10. (A) the dark adapted (DA) state comprises a thermal equilibrium mixture of bR_{555} and bR_{568} (B) Light adapted (LA), bR_{568}, accumulated by 532 nm irradiation of the rotating sample for 4 hours at 273 K (C) the Mo intermediate created by 532 nm irradiation of rotating LA at 230 K. The spectra of all three intermediates were obtained in roughly 2 hours with a spinning frequency of 7 kHz. (*right*) 2D spectrum obtained from DA bR illustrating the splittings observed at low temperature doe to inequivalent sites.

protons mediate ^1H-^1H spin diffusion, with the overall result of a higher enhancement. For example, Akbey et al. [38] reported that perdeuteration of the α-spectrin-SH3 domain led to three to five times higher DNP enhancement (e~148) than obtained with protonated SH3. In a more recent example we prepared 98% perdeuterated U-[^2H,^{13}C,^{15}N] bR and with 15 mM TOTAPOL and observed e= 72, whereas for U-[^1H, ^{13}C,^{15}N]-bR we obtained e~35-43. [34, 39] Thus, perdeuterated proteins will likely be important for biological applications of DNP.

2.4 Applications of DNP MAS NMR

2.4.1 Bacteriorhodopsin

To date one of the most interesting examples of the application of DNP is to the light-driven ion pump bR, which is a 26.6 kDa trans-membrane protein containing a retinal chromophore. bR has been studied intensively since its discovery in the 1970's[40, 41], but the mechanism by which it enforces vectorial action is still not understood and MAS NMR studies can potentially elucidate the relevant structural details of the intermediates in its photocycle (Figure 2.6 (*left*)). However, many of the intermediates can only be cryo-trapped at low (~5%) concentrations, so that high signal-to-noise, and therefore DNP, is required to observe their MAS NMR spectra. [34, 39]

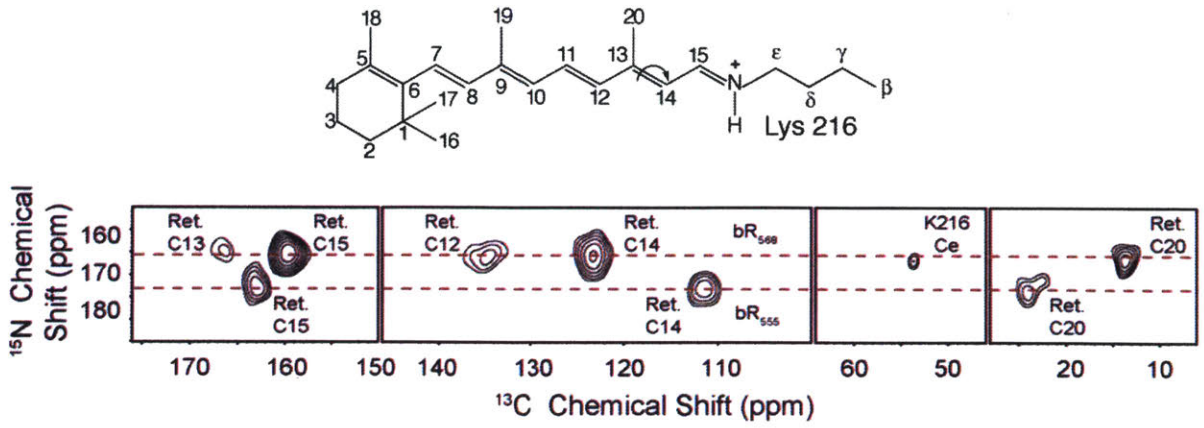

Figure 2.7: ^{15}N-^{13}C spectrum obtained from dark adapted U-[^{13}C,^{15}N]-bR after selective excitation of the ^{15}N Schiff base, CP to the ^{13}C-15 of the retinal and ^{13}Cε of Lys216, followed by RFDR mixing. The spectrum shows cross-peaks between the Schiff base ^{15}N and ^{13}C-12,13,14,15,20 on the retinal chromophore and ^{13}Cε Lys216 [27,33]. The arrow indicates the *trans-cis* isomerization of the C13=C14 bond that occurs during the photocycle.

The retinal cofactor is covalently bonded to Lys216 via a protonated Schiff base linkage, and the sensitivity of the unique ^{15}N chemical shift of the Schiff base to its local environment provides an excellent marker and probe of each photocycle intermediate. In the dark-adapted (DA) state, bR exhibits two conformations: bR_{555} and bR_{568} in a ratio of 60:40 (Figure 2.6 (middle, A). After irradiation at 532 nm, DA is converted to light adapted (LA) state in which only bR_{568} remains (Figure 2.6 (middle, B)). Upon the absorption of a photon, the retinal isomerizes and cycles the protein through several intermediates that can be cryo-trapped for observation *in situ*. Figure 2.6 (middle, C) shows the 1D spectrum of M_o. With low temperature DNP it is possible to perform 2D spectroscopy and a ^{13}C-^{15}N spectrum of DA bR is shown in Figure 2.6 (*right*) showing that at 90 K there are actually four forms of bR present – two each of the bR_{555} and bR_{568}.

We have also published the first DNP MAS NMR spectra of the K and L intermediates [34, 39]. While the K state showed just one Schiff base signal, it relaxed to several L states, of which all but one are dead ends (relaxing back to bR). The data for the functional L state (the one that relaxes to M) suggest that its Schiff base has a strong counterion. One of the possible explanations would support the hypothesis that bR is an inward OH^- pump, rather than an outward H^+ pump.

With the sensitivity available from DNP, it is also possible to record 3D correlation spectra for the individual resonances in the DA state which has an effective molecular weight of ~ 85 kDa. Figure 2.7 shows cross-peaks between the Schiff base ^{15}N and ^{13}C-12,13,14,15,20 of the retinal and ^{13}C-ε of Lys216 in the dark adapted state of bR. The experiment has been

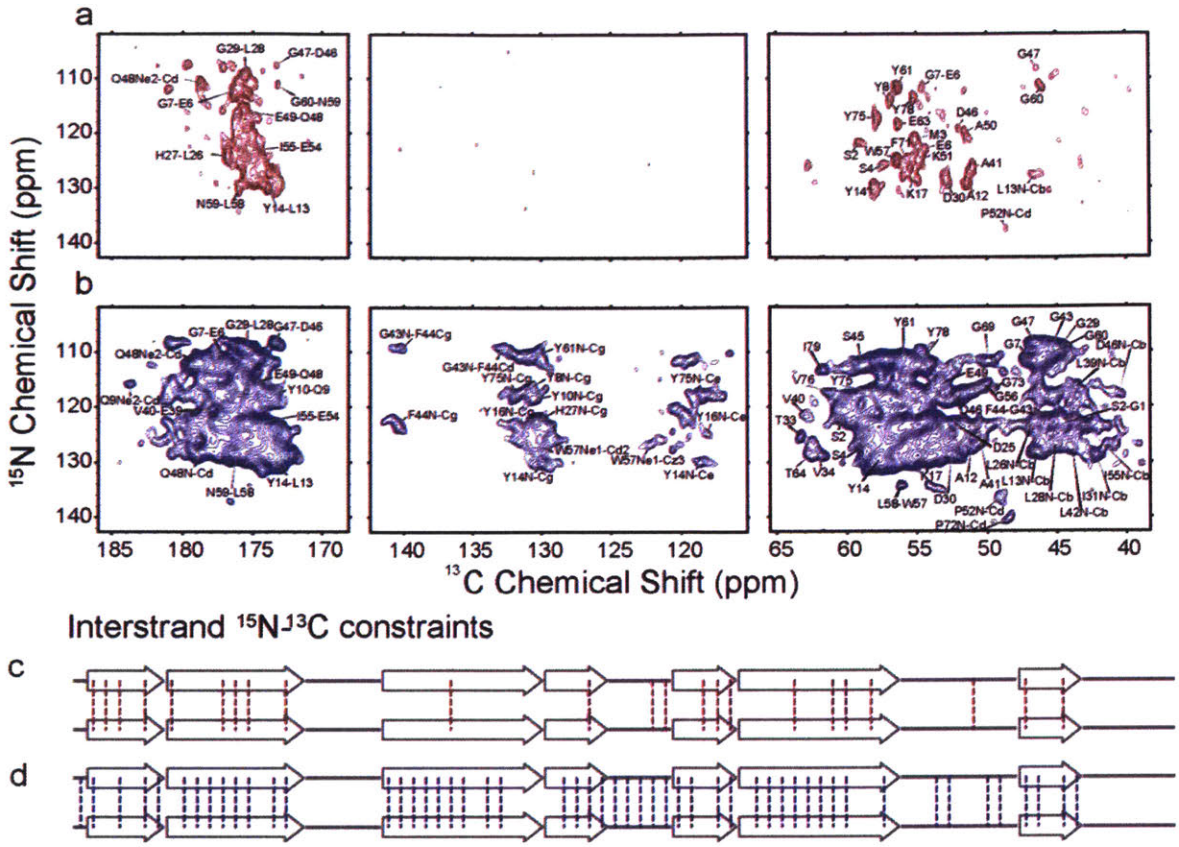

Figure 2.8: Comparison between room temperature and DNP enhanced, low temperature correlation spectra of PI3-SH3. The spectra were obtained with ZF-TEDOR recoupling (τ_{mix} = 16 ms) from sample prepared from partially labeled fibrils [^{15}N, ^{12}C] PI3-SH3 /[^{14}N,^{13}C] PI3-SH3 (50:50 molar ratio). (a) ^{15}N-^{13}C intermolecular correlations in PI3-SH3 fibrils at 300 K obtained at 750 MHz in 16 days of acquisition time. (b). Same sample and identical spectral regions were recorded at 100 K and 400 MHz with DNP enhancement in 32 h. (c). Illustration of the 23 interstrand contacts established from ^{13}C -^{15}N peaks in the 750 MHz spectra acquired at 300 K in a. (d) the 52 interstrand contacts established from the 400 MHz DNP enhanced spectra recorded

conducted by using a Gaussian pulse to select the signals arising from the ^{15}N of Lys216 in both bR_{568} and bR_{555} followed by a ^{15}N-^{13}C and then ^{13}C-^{13}C diffusion via RFDR mixing. Again the spectrum of bR would not be accessible *sans* DNP.

2.4.2 Amyloid Fibrils

MAS NMR is also essential for studies of the structure of amyloid fibrils. Intermolecular ^{13}C-^{13}C or ^{15}N-^{13}C distances derived from MAS DNP experiments provide otherwise unavailable structural constraints. The most straightforward approach is to measure long-range ^{13}C-^{15}N distances with a ZF-TEDOR experiment [42]. However, for distances ≥5 Å, the efficiency is low (< 5%), which vastly extends the acquisition time and severely limits the

number of constraints that can be observed. The application of DNP to overcome this situation has been demonstrated on mixed samples of [^{15}N, ^{12}C] PI3-SH3 /[^{14}N,^{13}C] PI3-SH3 (50:50 molar ratio). Figure 2.8 compares the ^{15}N-^{13}C intermolecular correlation spectra obtained with ZF-TEDOR recoupling (τ_{mix} = 16 ms) at 750 MHz without DNP and at 400 MHz with DNP, collected in 16 days and 32 hours respectively. The number of intermolecular ^{15}N-^{13}C constraints detected was more than doubled due to the DNP with e ~ 30 on ^{13}C. The additional constraints obtained from DNP permitted us to establish that the PI3-SH3 protein strands are aligned in a parallel and in-register β-sheet arrangement [35].

In addition, it is clear that the approaches described here are widely applicable to other areas of science, in particular materials problems – polymers, zeolites, surfaces, semiconductors, etc. These experiments will likely include spectroscopy of quadrupolar species such as ^{17}O[43] and ^{27}Al[44] as well as I=1/2 species. We refer the interested reader to other articles in this issue for a complete discussion of these very interesting applications.

Finally we note that, while most of the results described here were obtained at 250 GHz/380 MHz or 263 GHz/400 MHz, DNP experiments have recently been performed at 460 GHz/700 MHz[30] and at 395 GHz/600 MHz and 527 GHz/800 MHz [http://www.bruker.com/products/mr/nmr/dnp-nmr/overview.html]. Thus, DNP is rapidly moving to higher frequency where the chemical shift resolution will improve and additional systems will become accessible.

2.5 Conclusions

There are currently two important mechanisms that mediate high field DNP processes, namely the SE and the CE. In addition, there are a number of important experimental factors that influence the magnitudes of the enhancements, including microwave power, temperature, and the nature of the polarizing agent. With currently available technology — gyrotron microwave sources, MAS at 80 K, biradical polarizing agents, and partially deuterated proteins — it is possible to obtain enhancements of ≥100 on many samples. This enhancement, together with the improved Boltzmann factor of 300 K/80 K=3.75 due to the lower temperature, yields sensitivity gains of ≥375 and time savings of >10^5. Historically, increases in sensitivity of NMR experiments by factors of 10^2-10^3 have dramatically changed the landscape of what is possible with NMR, and we are beginning to witness the next step in this movement due to high frequency DNP. We have illustrated this point with applications of MAS DNP experiments to membrane proteins and fibrils which are typical of

the biological materials that will be studied in the future. These results clearly illustrate that many experiments that are not possible *sans* DNP, become feasible *avec* DNP. Thus, it is clear that the increased availability of commercial instruments to perform DNP experiments will open many new avenues of scientific and technical endeavor.

2.6. Acknowledgement

We thank Drs. Alexander Barnes, Bjorn Corzilius, Yongchao Su, Marvin J. Bayro and David J. Ruben for their insightful discussions and Jeffrey Bryrant, Ajay Thakkar, for their extensive technical assistance. This work was supported by National Institute of Health Grants EB002804, EB001960, EB003151, EB001035, GM095843 and EB002026.

2.7. References

1. Griffin, R. G. Dipolar Recoupling in Mas Spectra of Biological Solids. *Nat. Struct. Biol.* **1998,** *5,* 508-512.
2. Rienstra, C. M.; Hohwy, M.; Mueller, L. J.; Jaroniec, C. P.; Reif, B.; Griffin, R. G. Determination of Multiple Torsion-Angle Constraints in U-13c,15n-Labeled Peptides: 3d 1h-15n-13c-1h Dipolar Chemical Shift Spectroscopy in Rotating Solids. *J. Am. Chem. Soc.* **2002,** *124,* 11908-11922.
3. Thompson, L. K.; McDermott, A. E.; Raap, J.; van der Wielen, C. M.; Lugtenburg, J.; Herzfeld, J.; Griffin, R. G. Rotational Resonance Nmr Study of the Active Site Structure in Bacteriorhodopsin: Conformation of the Schiff Base Linkage. *Biochemistry* **1992,** *31,* 7931.
4. Griffiths, J. M.; Lakshmi, K. V.; Bennett, A. E.; Raap, J.; Vanderwielen, C. M.; Lugtenburg, J.; Herzfeld, J.; Griffin, R. G. Dipolar Correlation Nmr-Spectroscopy of a Membrane-Protein. *J. Am. Chem. Soc.* **1994,** *116,* 10178-10181.
5. Cady, S. D.; Schmidt-Rohr, K.; Wang, J.; Soto, C.; DeGrado, W.; Hong, M. Structure of the Amantadine Binding Site of Influenza M2 Proton Channels in Lipid Bilayers. *Nature* **2010,** *463,* 689-692.
6. Castellani, F.; van Rossum, B.; Diehl, A.; Schubert, M.; Rehbein, K.; Oschkinat, H. Structure of a Protein Determined by Solid-State Magic-Angle-Spinning Nmr Spectroscopy. *Nature* **2002,** *420,* 98-102.
7. Jaroniec, C. P.; MacPhee, C. E.; Bajaj, V. S.; McMahon, M. T.; Dobson, C. M.; Griffin, R. G. High Resolution Molecular Structure of a Peptide in an Amyloid Fibril Determined by Mas Nmr Spectroscopy. *Proc. Nat'l. Acad. Sci.* **2004,** *101,* 711-716.
8. Tycko, R. Molecular Structure of Amyloid Fibrils: Insights from Solid-State Nmr. *Q Rev Biophys* **2006,** *39,* 1-55.
9. Wasmer, C.; Lange, A.; Van Melckebeke, H.; Siemer, A. B.; Riek, R.; Meier, B. H. Amyloid Fibrils of the Het-S(218-289) Prion Form a Beta Solenoid with a Triangular Hydrophobic Core. *Science* **2008,** *319,* 1523-1526.
10. Bayro, M. J.; Maly, T.; Birkett, N.; MacPhee, C.; Dobson, C. M.; Griffin, R. G. High-Resolution Mas Nmr Analysis of Pi3-Sh3 Amyloid Fibrils: Backbone Conformation and Implications for Protofilament Assembly and Structure. *Biochemistry* **2010,** *49,* 7474-7488.
11. Maly, T.; Debelouchina, G. T.; Bajaj, V. S.; Hu, K.-N.; Joo, C.-G.; Mak-Jurkauskas, M. L.; Sirigiri, J. R.; Wel, P. C. A. v. d.; Herzfeld, J.; Temkin, R. J., et al. Dynamic Nuclear Polarization at High Magnetic Fields. *J. Chem Physics* **2008,** *128,* 052211.

12. Haze, O.; Corzilius, B.; Smith, A. A.; Griffin, R. G.; Swager, T. M. Water-Soluble Narrow-Line Radicals for Dynamic Nuclear Polarization. *J. Am. Chem. Soc.* **2012,** *134,* 14287–14290.
13. Song, C.; Hu, K.-N.; Joo, C.-G.; Swager, T. M.; Griffin, R. G. Totapol – a Biradical Polarizing Agent for Dynamic Nuclear Polarization Experiments in Aqueous Media. *J. Am Chem. Soc* **2006,** *128,* 11385-11390.
14. Matsuki, Y.; Maly, T.; Ouari, O.; Lyubenova, S.; Herzfeld, J.; Prisner, T.; Tordo, P.; Griffin, R. G. Dynamic Nuclear Polarization Using a Rigid Biradical. *Angewandte Chemie* **2009,** *48,* 4996-5000.
15. Can, T. V.; Caporini, M. A.; Mentink-Vigier, F.; Corzilius, B.; Walish, J. J.; Rosay, M.; Maas, W. E.; Baldus, M.; Vega, S.; Swager, T. M., et al. Overhauser Effects in Insulating Solids. *Journal of Chemical Physics* **2014,** *141.*
16. Goldman, M., *Spin Temperature and Nuclear Magnetic Resonance in Solids.* Oxford University Press: London, 1970.
17. Becerra, L. R.; Gerfen, G. J.; Temkin, R. J.; Singel, D. J.; Griffin, R. G. Dynamic Nuclear Polarization with a Cyclotron Resonance Maser at 5 T. *Physical Review Letters* **1993,** *71,* 3561-3564.
18. Hu, K.-N.; Bajaj, V. S.; Rosay, M. M.; Griffin, R. G. High Frequency Dynamic Nuclear Polarization Using Mixtures of Tempo and Trityl Radicals. *J. Chem. Phys.* **2007,** *126,* 044512.
19. Corzilius, B.; Smith, A. A.; Barnes, A. B.; Luchinat, C.; Bertini, I.; Griffin, R. G. High Field Dynamic Nuclear Polarization with High-Spin Transition Metal Ions. *Jour. Amer. Chem. Soc* **2011,** *133,* 5648–5651.
20. Hu, K. N.; Yu, H. H.; Swager, T. M.; Griffin, R. G. Dynamic Nuclear Polarization with Biradicals. *J. Am. Chem. Soc.* **2004,** *126,* 10844-10845.
21. Hu, K.-N.; Song, C.; Yu, H.-h.; Swager, T. M.; Griffin, R. G. High-Frequency Dynamic Nuclear Polarization Using Biradicals: A Multifrequency Epr Lineshape Analysis. *J. Chem. Phys.* **2008,** *128,* 052321.
22. Hu, K.-N.; Debelouchina, G. T.; Smith, A. A.; Griffin, R. G. Quantum Mechanical Theory of Dynamic Nuclear Polarization in Solid Dielectrics. *J. Chem. Physics* **2011,** *134,* 125105.
23. Schweiger, A.; Jeschke, G., *Principles of Pulsed Electron Paramagnetic Resonance.* Oxford University Press: 2001.
24. Bajaj, V. S.; Farrar, C. T.; Hornstein, M. K.; Mastovsky, I.; Vieregg, J.; Bryant, J.; Elena, B.; Kreischer, K. E.; Temkin, R. J.; Griffin, R. G. Dynamic Nuclear Polarization at 9t Using a Novel 250 Ghz Gyrotron Microwave Source. *J. Mag. Res.* **2003,** *160,* 85-90.
25. Rosay, M.; Lansing, J. C.; Haddad, K. C.; Bachovchin, W. W.; Herzfeld, J.; Temkin, R. J.; Griffin, R. G. High Frequency Dynamic Nuclear Polarization in Mas Spectra of Membrane and Soluble Proteins. *J. Am. Chem. Soc.* **2003,** *125,* 13626-13627.
26. Barnes, A. B.; Corzilius, B.; Mak-Jurkauskas, M. L.; Andreas, L. B.; Bajaj, V. S.; Matsuki, Y.; Belenky, M. L.; Lugtenburg, J.; Sirigiri, J. R.; Temkin, R. J., et al. Resolution and Polarization Distribution in Cryogenic Dnp/Mas Experiments. *Phys. Chem. Chem. Phys.* **2010,** *12.*
27. Becerra, L. R.; Gerfen, G. J.; Bellew, B. F.; Bryant, J. A.; Hall, D. A.; Inati, S. J.; Weber, R. T.; Un, S.; Prisner, T. F.; McDermott, A. E., et al. A Spectrometer for Dynamic Nuclear-Polarization and Electron- Paramagnetic-Resonance at High-Frequencies. *J. Magn. Reson. Ser. A* **1995,** *117,* 28-40.
28. Bajaj, V. S.; Hornstein, M. K.; Kreischer, K. E.; Sirigiri, J. R.; Woskov, P. P.; Mak-Jurkauskas, M. L.; Herzfeld, J.; Temkin, R. J.; Griffin, R. G. 250 Ghz Cw Gyrotron Oscillator for Dynamic Nuclear Polarization in Biological Solid State Nmr. *J Magn Reson* **2007,** *189,* 251-279.

29. Barnes, A. B.; Nanni, E. A.; Griffin, R. G.; Temkin, R. J. A 250 Ghz Gyrotron with a 3 Ghz Tuning Bandwidth for Dynamic Nuclear Polarization. *J. Magn. Reson.* **2012,** *221,* 147–153.
30. Barnes, A. B.; Markhasin, E.; Daviso, E.; Michaelis, V. K.; Nanni, E. A.; Jawla, S.; Mena, E.; DeRocher, R.; Thakkar, A.; Woskow, P., et al. Dynamic Nuclear Polarization at 700 Mhz/460 Ghz. *J. Magn. Reson.* **2012,** *221,* 1-7.
31. Barnes, A. B.; Mak-Jurkauskas, M. L.; Matsuki, Y.; Bajaj, V. S.; Wel, P. C. A. v. d.; DeRocher, R.; Bryant, J.; Sirigiri, J. R.; Temkin, R. J.; Lugtenburg, J., et al. Cryogenic Sample Exchange Nmr Probe for Magic Angle Spinning Dynamic Nuclear Polarization. *Jour. Magnetic Resonance* **2009,** *198,* 261–270.
32. Thurber, K. R.; Yau, W.-M.; Tycko, R. Low-Temperature Dynamic Nuclear Polarization at 9.4 T with a 30 Mw Microwave Source. *Jour Magn Resonance* **2010,** *204,* 303-313.
33. Gerfen, G. J.; Becerra, L. R.; Hall, D. A.; Griffin, R. G.; Temkin, R. J.; Singel, D. J. High-Frequency (140 Ghz) Dynamic Nuclear-Polarization - Polarization Transfer to a Solute in Frozen Aqueous-Solution. *Journal of Chemical Physics* **1995,** *102,* 9494-9497.
34. Bajaj, V. S.; Mak-Jurkauskas, M. L.; Belenky, M.; Herzfeld, J.; Griffin, R. G. Functional and Shunt States of Bacteriorhodopsin Resolved by 250-Ghz Dynamic Nuclear Polarization-Enhanced Solid-State Nmr *Proc. Nat'l. Acad. Sci.* **2009,** *106,* 9244-9249.
35. Bayro, M. J.; Debelouchina, G. T.; Eddy, M. T.; Birkett, N. R.; MacPhee, C. E.; Rosay, M.; Maas, W. E.; Dobson, C. M.; Griffin, R. G. Intermolecular Structure Determination of Amyloid Fibrils with Magic-Angle Spinning, Dynamic Nuclear Polarization Nmr. *J. Am. Chem. Soc.* **2011,** *133,* 13967–13974.
36. Kiesewetter, M.; Corzilius, B.; Smith, A. A.; Griffin, R. G.; Swager, T. M. Dynamic Nuclear Polarization with a Water-Soluble Rigid Biradical. *J. Am. Chem. Soc.* **2012,** *134,* 4537–4540.
37. Rosay, M.; Weis, V.; Kreischer, K. E.; Temkin, R. J.; Griffin, R. G. Two-Dimensional ^{13}c-^{13}c Correlation Spectroscopy with Magic Angle Spinning and Dynamic Nuclear Polarization. *Journal of the American Chemical Society* **2002,** *124,* 3214-3215.
38. Akbey, Ü.; Franks, W. T.; Linden, A.; Lange, S.; Griffin, R. G.; Rossum, B.-J. v.; Oschkinat, H. Dynamic Nuclear Polarization of Deuterated Proteins. *Angewandte Chemie International Edition* **2010,** *49,* 7803–7806.
39. Mak-Jurkauskas, M. L.; Bajaj, V. S.; Hornstein, M. K.; Belenky, M.; Griffin, R. G.; Herzfeld, J. Gradual Winding of the Bacteriorhodopsin Chromophore in the First Half of Its Ion-Motive Photocycle: A Dynamic Nuclear Polarization Enhanced Solid State Nmr Study. *Proc. Nat'l. Acad. Sci.* **2008,** *105,* 883-888.
40. Harbison, G. S.; Herzfeld, J.; Griffin, R. G. Solid-State ^{15}n Nuclear Magnetic-Resonance Study of the Schiff-Base in Bacteriorhodopsin. *Biochemistry* **1983,** *22,* 1-5.
41. Harbison, G. S.; Smith, S. O.; Pardoen, J. A.; Courtin, J. M. L.; Lugtenburg, J.; Herzfeld, J.; Mathies, R. A.; Griffin, R. G. Solid-State C-13 Nmr Detection of a Perturbed 6-S-Trans Chromophore in Bacteriorhodopsin. *Biochemistry* **1985,** *24,* 6955-6962.
42. Jaroniec, C. P.; Filip, C.; Griffin, R. G. 3d Tedor Nmr Experiments for the Simultaneous Measurement of Multiple Carbon-Nitrogen Distances in Uniformly C-13, N-15-Labeled Solids. *Journal of the American Chemical Society* **2002,** *124,* 10728-10742.
43. Michaelis, V. K.; Markhasin, E.; Daviso, E.; Herzfeld, J.; Griffin, R. G. Dynamic Nuclear Polarization of Oxygen-17. *J. Phys. Chem. Lett.* **2012,** *3,* 2030–2034.
44. Vitzthum, V.; Mieville, P.; Carnevale, D.; Caporini, M. A.; Gajan, D.; Cope, C.; Lelli, M.; Zagdoun, A.; Rossini, A. J.; Lesage, A., et al. Dynamic Nuclear Polarization of Quadrupolar Nuclei Using Cross Polarization from Protons: Surface-Enhanced Aluminium-27 Nmr. *Chem. Commun.* **2012,** *48,* 1988-1990.

Chapter 3: Peptide and Protein Dynamics and Low-Temperature/DNP Magic Angle Spinning NMR

Adapted from Q.Z. Ni, E. Markhasin, T.V. Can, B. Corzilius, K.O. Tan, A.B. Barnes, E. Daviso, Y.C. Su, J. Herzfeld, and R.G. Griffin, Journal of Physical Chemistry 141 (2014) 064202

In DNP MAS NMR experiments at ~80-110 K, the structurally important $-^{13}CH_3$ and $-^{15}NH_3^+$ signals in MAS spectra of biological samples disappear due to the interference of the molecular motions with the ^1H decoupling. Here we investigate the effect of these dynamic processes on the NMR lineshapes and signal intensities in several typical systems: (1) microcrystalline APG, (2) membrane protein bR, (3) amyloid fibrils PI3-SH3, (4) monomeric alanine–CD_3 and (5) the protonated and deuterated dipeptide N-Ac-VL over 78-300 K. In APG, the 3-site hopping of the Ala-C_β peak disappears completely at 112 K, concomitant with the attenuation of CP signals from other ^{13}C's and ^{15}N's. Similarly, the ^{15}N signal from Ala-NH_3^+ disappears ~173 K, concurrent with the attenuation in CP experiments of other ^{15}N's as well as ^{13}C's. In bR and PI3-SH3, the methyl groups are attenuated at ~95 K while all other ^{13}C's remain unaffected. However, both systems exhibit substantial losses of intensity at ~243 K. Finally, with spectra of Ala and N-Ac-VL we show that it is possible to extract site-specific dynamic data from the temperature dependence of the intensity losses. Furthermore, ^2H labeling can assist with recovering the spectral intensity. Thus, our study provides insight into the dynamic behavior of biological systems over a wide range of temperatures, and serves as a guide to optimizing the sensitivity and resolution of structural data in low temperature DNP MAS NMR spectra.

3.1 Introduction

Magic angle spinning (MAS) NMR spectroscopy is now established as a versatile and essential tool in structural biology.[1-9] In particular, advances in sample preparation, methodology,[10-19] and labeling strategies have dramatically improved the resolution of MAS spectra, thus making possible structural studies of large biomolecules not accessible with other techniques.[20-24] Nevertheless, the primary limiting factor of MAS NMR is its inherently low sensitivity. An approach to circumvent this limitation is operation at cryogenic temperatures, since the Boltzmann population scales as 1/T.[25, 26] An even greater gain in sensitivity can be achieved by integrating dynamic nuclear polarization (DNP) into the MAS NMR experiments, where orders of magnitude enhancements of NMR signal intensities have been reported for peptide and protein samples.[27-30] This permits experiments that are otherwise difficult or impossible to perform.[31-35]

To take advantage of this increased sensitivity, DNP/NMR experiments at 80-120 K are becoming widely accessible and heavily utilized. However, to date, the tremendous sensitivity gain overshadows the effects of molecular motions present in the ambient and low temperature spectra. For example, in many cases, side chain and backbone resonances of structural importance are absent for reasons that are glibly referred to as "dynamics" but are not clearly delineated or understood. Early ^{2}H NMR studies on model compounds revealed threefold hopping (at 10^{3}-10^{6} s^{-1}) by $-CD_3$ and $-ND_3^{+}$ groups at 130-200 K and 200–310 K temperatures, respectively[36-39] and there have been a few investigations of these threefold processes and twofold flips of aromatic rings in peptides and proteins at low temperatures.[40-47] However, to the best of our knowledge, none of them provide a detailed description of the effects of these processes on the accompanying loss in signal intensity in MAS spectra, especially in the 80-120 K regime. Furthermore, recent observation of heteronuclear polarization transfer under DNP has been attributed to methyl dynamics in proteins [48]. Thus, the purpose of the experiments reported here is to provide an overview of the global and site-specific spectral intensity losses as a function of temperature. Thus, we combine data from ^{1}H-^{13}C/^{15}N cross polarization (CP), ^{13}C Bloch decay MAS experiments recorded from a series of temperature-dependent MAS NMR spectra on five systems including: (1) the microcrystalline tripeptide alanyl-prolyl-glycine (APG), (2) the membrane protein bacteriorhodopsin (bR), (3) amyloid fibrils of phosphatydinal-inositol-3-kinase SH3 domain (PI3-SH3), (4) monomeric $-CH_3$ and $-CD_3$ alanine and (5) the protonated and deuterated dipeptide N-acetyl-valyl-leucine (N-Ac-VL) over the temperature range 78-300 K.

In APG we find that the motion of the $-NH_3^+$ and $-CH_3$ interferes with ^1H decoupling and also compromises CP efficiencies, leading to specific and complete attenuation of spectral lines from these two groups at ~173 K and ~112 K, respectively. In addition, these intensity losses propagate throughout the sample, causing a global loss of spectral intensity. At temperatures around 80 K, the interfering motions approach the rigid lattice limit and the signal intensity fully recovers. In this regime, the gain in signal intensity is purely due to the Boltzmann factor.

Two classes of larger protein systems commonly studied at low temperature and with DNP include membrane and amyloid proteins.[49-52] Examples of these systems include bR in its native purple membrane and PI3-SH3. In both of these cases, the signal minimum due to the dynamics of $-CH_3$ groups occurs at a lower temperature (95 K) and appears to be localized as opposed to the case of APG. In addition, other spectral regions such as the carbonyl and aromatic resonances are not affected and exhibit improved signals. Finally, we show that intensity losses due to dynamic process can be partially and in some cases completely recovered by the introduction of ^2H labeling. In particular, the introduction of $-CD_3$ groups in Ala, N-Ac-VL and the use of perdeuterated bR permit observation of these groups in cases where spectral lines from the $-CH_3$ moiety are completely absent.

3.2 Experimental

3.2.1 Sample preparation

Both uniformly ^{13}C,^{15}N-labeled and ^{15}N-labeled APG samples were diluted to 10% with the corresponding natural abundance APG to suppress any intermolecular couplings. This was accomplished by dissolving the mixture of labeled APG/ natural abundance APG in a minimal amount of water (~ 45 mg/ml) followed by slow crystallization in a desiccator, and crystals forming in about a week. 40 mg of each APG samples was packed into a 4 mm Revolution NMR zirconia rotor.

Bacteriorhodopsin (bR), in its native purple membrane, was purified from *Halobacterium salinarum* grown in uniformly ^{13}C, ^{15}N-labeled peptone medium[53]. Peptone was obtained from the anaerobic acid hydrolysis of *Methylophilus methylotrophus* cells grown on ^{13}C-labeled methanol and ^{15}N-labeled ammonium sulfate.[54] The purple membranes were isolated using the method of Oesterhelt and Stoechenius[55]. The sample was washed 3 times with 300 mM guanidine hydrochloride at pH 10.0. The sample was pelleted after every wash by centrifugation for 2 hours at ~43,000 g. The washed pellet was mixed with 5mM AMUPol[56] or 15mM TOTAPOL[57] in

"DNP juice" consisting of d_8-glycerol/D_2O/H_2O (60/30/10 volume ratio) and centrifuged once more.

The phosphatidyl-inositol-3-kinase SH3 domain PI3-SH3 fibril sample was uniformly ^{13}C,^{15}N-labeled at the F, V, Y and L residues. The fibrils were grown from a solution of monomeric protein by incubation at pH 2.0 and 25°C for 14 days.[58] "DNP juice" was adjusted to pH 2.0 and supplemented with 15 mM TOTAPOL was added to the gel-like fibrils for cryoprotection and DNP experiments. Both bR and PI3-SH3 samples were packed into a 4 mm sapphire rotor for DNP/NMR experiments.

[U-^{13}C,^{15}N] and [-CD_3-U-^{13}C,^{15}N] alanine were purchased from Cambridge Isotope Laboratories (CIL) and dissolved in water then crystallized in a desiccator. [U-^{13}C,^{15}N] *N*-acetyl-L-Val-L-Leu (N-Ac-VL) and [1,2-^{13}C] acetic anhydride were purchased from CIL. N-Ac-VL was synthesized by New England Peptide (Gardner, MA), using standard solid-phase methods and purified by HPLC. N-Ac-VL was crystallized from a 1:1 (v/v) H_2O:acetone solution.

3.2.2 NMR Spectroscopy

MAS spectra were recorded using a custom-designed triple resonance (^1H, ^{13}C, ^{15}N) cryogenic MAS probe equipped with a sample exchange system[59] on home-built NMR spectrometer operating at 380 MHz ^1H frequency (courtesy of Dr. D. J. Ruben). Two types of 1D NMR experiments were conducted for APG: ^1H-^{13}C/^{15}N cross polarization (CP) and ^{13}C Bloch decay. For CP experiments, a spin-lock field of 50 kHz was employed on the proton channel. Experimental parameters including: recycle delay, CP Hartmann Hahn matching conditions, CP duration and TPPM decoupling have all been optimized for all temperature dependent experiments. ^1H TPPM decoupling fields $\omega_{1H}/2\pi$ = 83 kHz or 100 kHz and $\omega_r/2\pi$ = 4.83 kHz were used unless stated otherwise.

Liquid nitrogen boil-off gas was used for both the bearing and drive gas streams, and the spinning frequency was controlled by a Bruker MAS controller[59]. Both bearing and drive streams were cooled using a custom-designed heat exchanger, and the temperature was subsequently controlled using heating elements inside vacuum jacketed transfer lines with two PID controllers (Lakeshore, Westerville, OH). The sample temperature was monitored using a fiber optic temperature sensor (Neoptix, Quebec, Canada) that extends to the inside of the MAS stator. The fiber optic thermometers were calibrated by immersion in liquid nitrogen at 77 K. Note, during MAS experiments, we have consistently recorded temperatures in the range 72 K-

77 K presumably due to Joule-Thompson cooling on the expansion of the N_2 gas from the jets of drive cup and bearings of the stator.

3.2.3 DNP Experiments

In order to investigate methyl group dynamics at DNP temperatures, ^{1}H, ^{13}C, ^{15}N CP and homonuclear experiments were performed using a home-built DNP gyrotron instrument operating at 250 GHz / 380 MHz with ~14 W of microwave power.[60, 61] Enhancement factors (ε) were calculated by comparing the signals obtained with and without μw irradiation.

3.2.4 Simulations

The simulations of the Ala–CH_3 group dynamics in APG were performed using GAMMA[62] with 100 powder orientations chosen using ZCW scheme.[63] Details of the parameters used can be found in SI. In order to simulate the three-site hopping mechanism, the simulations were carried out in a composite Liouvillian space that facilitates mutual-exchange mechanism. The dimensions of the exchange matrices for the four-spin CH_3 and CD_3 spin systems are 256 x 256 and 2916 x 2916 respectively. The amount of time required to simulate the FID of one crystallite orientation using one CPU core is ~1 minute and ~1.5 days for CH_3 and CD_3 respectively. All simulations took ~2 weeks to compute using ETH Brutus cluster with 384 CPU cores. The parameters chosen for the simulations are $\omega_r/2\pi$=4.651 kHz, TPPM decoupling $\omega_{1H}/2\pi$ = 83 kHz with 6.9 μs pulses and phases ±15 degree. The size of the quadrupole coupling used for ^{2}H nuclei is 167 kHz.

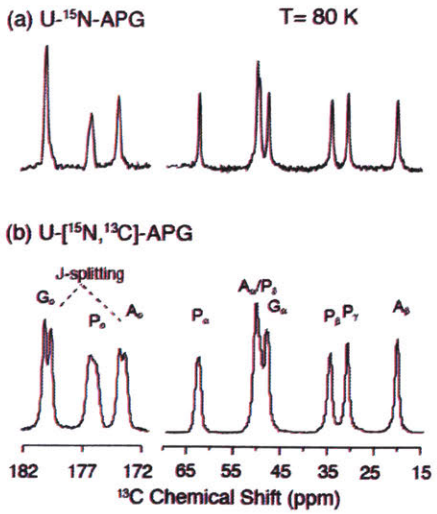

Figure 3.1 ^{13}C CP-MAS spectrum of [U-^{15}N] APG (a) and [U-^{13}C, ^{15}N] APG (b) at 80 K. Both samples were diluted to 10% in unlabeled APG to minimize the intermolecular couplings. The linewidth of the Gly-C_o is 27 Hz (0.28 ppm). In (b) the linewidth is broadened by ^{13}C-^{13}C *J*-coupling evident in the doublet splitting in the carbonyl region with the Gly-C_o and Ala-C_o showing one bond C_α-C_o *J*-couplings of ~50 Hz. The fact

that these resonances are not resolved in the aliphatic region is likely due to the presence of multiple *J*-couplings.

3.3 Results

The 1D ^{13}C spectra in **Figure 3.1** illustrate the spectral resolution of two microcrystalline APG samples with differing isotopic labeling schemes at 80 K. In both cases, the spectra exhibit resolution comparable to that obtained at room temperature. Specifically, **Figure 3.1a** shows a ^{13}C CP MAS NMR spectrum of [U-^{12}C,^{15}N]-APG and in the absence of ^{13}C-^{13}C *J*-couplings, the linewidth of the Gly-C_o is as narrow as 27 Hz (0.28 ppm). In comparison, the linewidths in the spectrum of [U-^{13}C,^{15}N]-APG (**Figure 3.1b**) increase by a factor of two or more primarily due to one bond *J*-couplings and higher order cross terms that arises from the denser ^{13}C network. Nevertheless, resolved *J*-splittings (~50 Hz) can still be distinguished in two out of three

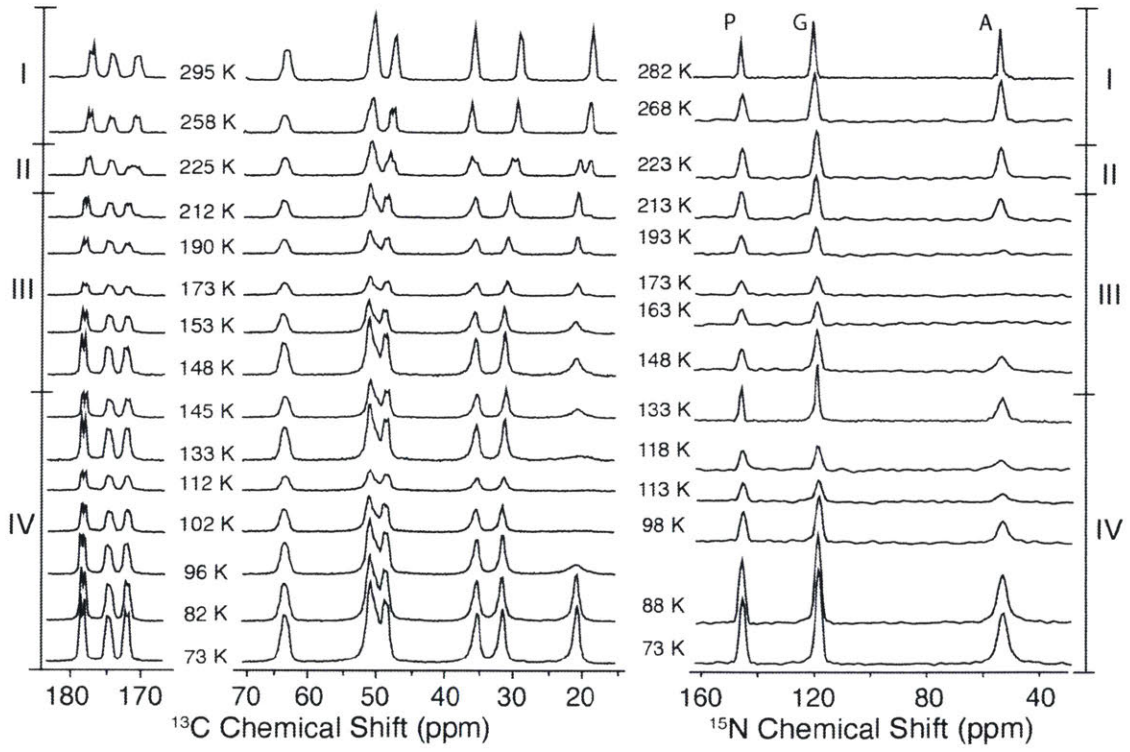

Figure 3.2 Temperature-dependent ^{1}H-^{13}C CP (left column) and ^{1}H-^{15}N CP (right column) spectra of [U-^{13}C,^{15}N] APG. Several important spectral changes are observed. In region (III), between 213 K and 148 K, the intensity of the Ala-NH_3^+ peak is buried under the noise level at ~ 173 K, which couples with the partial attenuation of the ^{13}C spectrum. Region (IV), below 148 K, exhibits the disappearance of the Ala-CH_3 signal at ~113 K, coincident with the signal dip in the ^{15}N spectrum. The spectral changes are further analyzed in **Figure 3**. The spectra were acquired with $\omega_r/2\pi$ = 4.83 kHz, $\omega_{1H}/2\pi$ = 83 kHz for TPPM decoupling

carbonyls, each of which has only one *J*-coupled neighboring ^{13}C. On the other hand, each ^{13}C in the aliphatic region is *J*-coupled to multiple neighbors, which obscures the splitting. The aliphatic carbons also have stronger CH dipolar coupling than that of carbonyl carbons, and would require stronger decoupling and higher spinning frequencies to be averaged out effectively. The data confirm that the optimal resolution in MAS spectra can be obtained with sparsely labeled ^{13}C samples.[64] In addition, they demonstrate that high resolution in well-ordered materials can be obtained at cryogenic temperatures (~ 80 K).

Figure 3.2 illustrates the temperature dependence of the ^{1}H-^{13}C/^{15}N CP-MAS spectra acquired in the range from 73 K to 295 K, where we observe several interesting spectral changes. First, in the transition between regions I and II at 225 K, there is a doubling in all of the side chain signals that is especially obvious on the Ala-C_β line ($\delta \approx 18$ ppm at 295 K), as well as Pro-C_β and Pro-C_γ (30 ppm and 35 ppm at 295 K, respectively). A recent calorimetric study of APG crystals revealed that the spectral changes at 225 K, although in the vicinity of the famous protein glass transition,[65] are likely the result of a polymorphic phase transition[66]. Similar spectral changes at ~200 K were observed for the peptide N-*f*-MLF-OH.[32] Second, in region III, the intensity of Ala-C_β exhibits a local minimum that coincides with the disappearance of the ^{15}N signal from the $-NH_3^+$ group at ~173 K. Third, at lower temperatures, in region IV between 148 K and 96 K, a more significant loss of Ala-$^{13}C_\beta$ signal intensity occurs. The intensity decreases dramatically and the Ala-$^{13}C_\beta$ line disappears into the baseline at ~112 K, and there is a concurrent loss of spectral intensity in the ^{15}N spectra at this temperature. We attribute the two signal minima in regions III and IV at ~173 K and ~112 K to the threefold hopping rates of the $-NH_3^+$ and $-CH_3$ groups, respectively, matching the ^{1}H decoupling frequency. Finally, at lower temperatures the hopping rate enters the slow exchange limit and the $-CH_3$ and $-NH_3^+$ lines reappear, narrow and the intensity recovers fully at 73 K.

The temperature dependence of the signal intensity is a product of the Boltzmann factor, which has a T^{-1} dependence, and the intensity loss due to molecular motions, which varies with temperature. In order to isolate the effect of molecular dynamics, the contribution from the Boltzmann factor is removed by multiplying the integrated signal intensity by the corresponding temperature. **Figure 3.3a** shows the normalized signal intensity of Ala-C_β ($-CH_3$ group) with (red solid circles) and without (blue open circles) the correction for the Boltzmann factor. To correct for the Boltzmann factor, the normalized intensity was calculated as $(I \cdot T)/(I_0 \cdot T_0)$ where I_0 is the intensity at the highest temperature T_0, where experiments were performed and I is the intensity at temperature T. To facilitate data presentation, without the correction for the

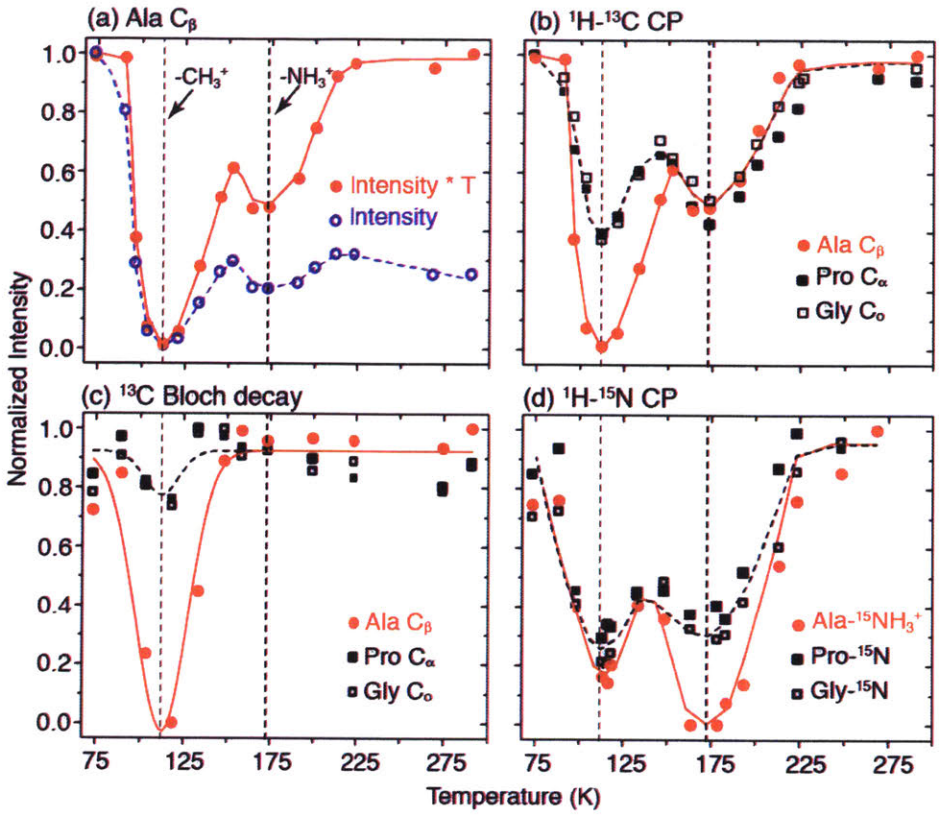

Figure 3.3 Temperature dependence of the integrated peak intensities of [U-^{13}C,^{15}N]-APG. The vertical dashed lines indicate the minima in the signal intensities at ~112 K and ~173 K due to the hopping of -CH_3 and -NH_3^+, respectively. (a) Ala-C_β from ^{1}H -^{13}C CP with (red solid circles) and without (blue open circles) Boltzmann correction at each temperature. (b) Adjusted spectrum intensities of several peaks of APG plotted as a function of temperature from ^{1}H -^{13}C CP. Again, notice the two minima, ~112 K where the Ala-C_β peak broadens beyond detection, and ~173 K. (c) ^{13}C Bloch decay experiments show the first minimum, indicating interference between methyl hopping and ^{1}H decoupling. (d) Spectral intensities of ^{1}H -^{15}N CP alanine NH_3^+as a function of temperature. The second minimum in (b) is due to the hopping of Ala-NH_3^+ group.

Boltzmann factor, the normalized intensity was calculated differently as (I / I_0) to where I_0 the intensity at lowest temperature at which we perform experiments. Note that the integrated signal intensities were adjusted when necessary by their relative ^{1}H or ^{13}C T_1's measured at each temperature and incorporated into the intensity calculations. T_{1H} and T_{13C} values are plotted as a function of temperature in **Figure 3.8** in the supporting information.

The minima at ~112 K and ~173 K in **Figure 3.3** are visible even without this correction and are greatly amplified with the correction. Below 90 K and above 225 K, the adjusted signals in red are essentially the same, indicating that the signal intensities are unaffected by the effect of molecular dynamics in these regions. In particular, the signal intensity in these regions follows

closely the T^{-1} dependence, resulting in a factor of 4 times higher intensity at 73 K compared to 295 K. **Figure 3.3b** illustrates that other sites such as Pro-C_{α} and Gly-C_o also exhibit two signal minima in ^{1}H-^{13}C CP experiments and the entire spectrum is uniformly attenuated at 112 K and 173 K. **Figure 3.3c** presents the data from the single-pulse ^{13}C Bloch decay signals detected with ^{1}H decoupling that show a minimum at 112 K, and a set of ^{13}C Bloch decay spectra is included in **Figure 3.9**. Furthermore, at this temperature the Ala-CH_3 is also completely attenuated **(Figure 3.3a)**, whereas other sites are nearly unaffected. In combination, the data in **Figure 3.3b** and 3.**3c** suggest that the signal minimum at ~112 K is associated with the threefold hopping rate of the Ala–CH_3, which approximates to the Rabi frequency of the ^{1}H RF fields during decoupling and/or CP. The minimum at ~173 K is attributed to the hopping of the Ala-NH_3^+ which manifests itself in the disappearance of its ^{1}H-^{15}N CP signal as shown in **Figure 3.3d**. In comparison to the ^{1}H-^{13}C CP data (**Figure 3.3b**), the ^{1}H-^{15}N CP data also exhibit two minima but in reverse intensity order: nearly uniform signal attenuation at ~112 K and complete signal attenuation of Ala-NH_3^+ at ~173 K.

Motivated by the dramatic changes in signal intensities in the APG spectra, we extended our studies to the membrane protein bR, and to amyloid fibrils formed by PI3-SH3, to determine if a similar behavior is observed in these systems. **Figure 3.4a** illustrates that attenuation of methyl ^{13}C resonances occurs in [U-^{13}C,^{15}N]-bR. However, because of spectral overlap in this 248 amino acid, uniformly ^{13}C/^{15}N labeled protein, the extraction of accurate intensity data for these resonances is imprecise. Multidimensional experiments at higher fields are required to obtain better resolution. In contrast, the spectra in **Figure 3.4c** of [^{13}C,^{15}N-FVYL]-PI3-SH3 are greatly simplified, which permits the extraction of the intensity of different functional groups, especially the Val-CH_3 and Leu-CH_3. In general, the spectra show that the overall intensity of carbonyl and aromatic ^{13}C's in both samples increases as temperature decreases except around 243 K (**Figure 3.4b** and **3.4d**). In addition, the methyl groups exhibit another minimum at

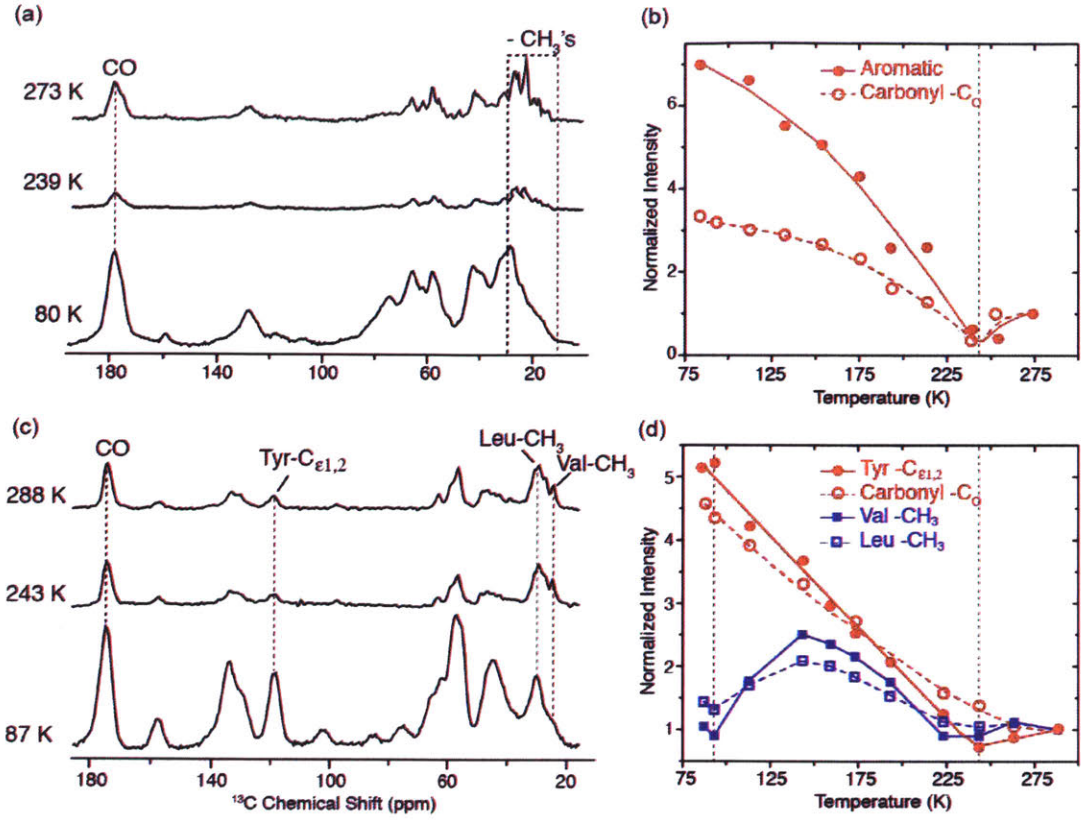

Figure 3.4 Temperature-dependent ^{1}H-^{13}C CP spectra of (a) [U-^{13}C,^{15}N] bacteriorhodopsin and (c) [^{13}C,^{15}N- FVYL]-PI3-SH3 amyloid fibrils without Boltzmann correction. In (b) and (d) we show plots of normalized intensities for carbonyl, aromatic and aliphatic regions in bR and PI3-SH3 fibrils as a function of temperature. Both carbonyl and aromatic experience a minimum in intensity around 243 K followed by a steady increase as the temperature is decreased for both systems. The intensity of $-CH_3$'s in the valines and leucines in PI3-SH3 also reveals a minimum at ~243 K, followed by a second minimum at ~95 K, where the intensity losses are again due to $-CH_3$ hopping interfering with ^{1}H decoupling and spin-lock fields. Both samples were cryoprotected in d_8-glycerol/D_2O/H_2O (60/30/10 volume ratio). Full sets of spectra at different temperatures are provided in **Figure 3.10** and **3.11**. The spectra were acquired with $\omega_r/2\pi$ = 4.83 kHz for bR and 7 kHz for PI3-SH3. In both cases, $\omega_{1H}/2\pi$ = 83 kHz for TPPM decoupling.

~95 K in the case of [^{13}C,^{15}N-FVYL]-PI3-SH3, but the intensities of the two $-CH_3$ containing residues are partially recovered at 87 K and are expected to fully recover at lower temperatures. Incorporation of DNP into the experiments in this temperature regime will, in addition to the Boltzmann factor, boost the sensitivity. In **Figure 3.12,** we show 1D ^{1}H-^{13}C CP spectra of [^{13}C,^{15}N-FVYL]-PI3-SH3 obtained with a signal enhancement of 35. A 2D RFDR spectrum of [^{13}C,^{15}N-FVYL]-PI3-SH3 fibril with τ_{mix}=1.6 ms was acquired in approximately 4 hours. Without DNP, the same spectrum would require one month to achieve the same S/N.

In **Figure 3.4b** and **3.4d**, the intensities are normalized to those obtained at 275 K for bR and 283 K for PI3-SH3. We note that the normalized intensities of the aromatic ^{13}C's at ~ 80-90 K

can be larger than the contribution from the Boltzmann factor. This is due to the fact that at 300 K there is already a significant loss in signal intensity in aromatic ring spectra due to the twofold ring flips,[67-70] which affects the polarization transfer during CP and interferes with decoupling. This phenomenon was observed in N-*f*-MLF-OH where the δ, δ' and ε, ε' signals from the Phe ring are absent in the 300 K 1D spectra. They start to reappear at 250K-225K and are fully developed at lower temperatures.[32] In addition, in ZF-TEDOR spectra of PI3-SH3, the aromatic region is essentially empty at 300 K but is intense and well resolved at 90 K.[71] Thus, the broad signal minimum around 243 K probably extends to the higher temperatures, ~ 280 K. Note also that protein samples used for DNP are cryoprotected by the glass-forming mixture of glycerol/water (60/40 volume ratio), as it is the case for the bR and PI3-SH3 samples used in our study. Therefore, the signal minimum at 243 K coincides with the freezing of the glycerol/water mixture and a slowing of the twofold flips of the 24 aromatic rings in bR. We also note that this temperature is close to that of the protein glass transition, although it is generally centered at the somewhat lower temperature (~200 K).

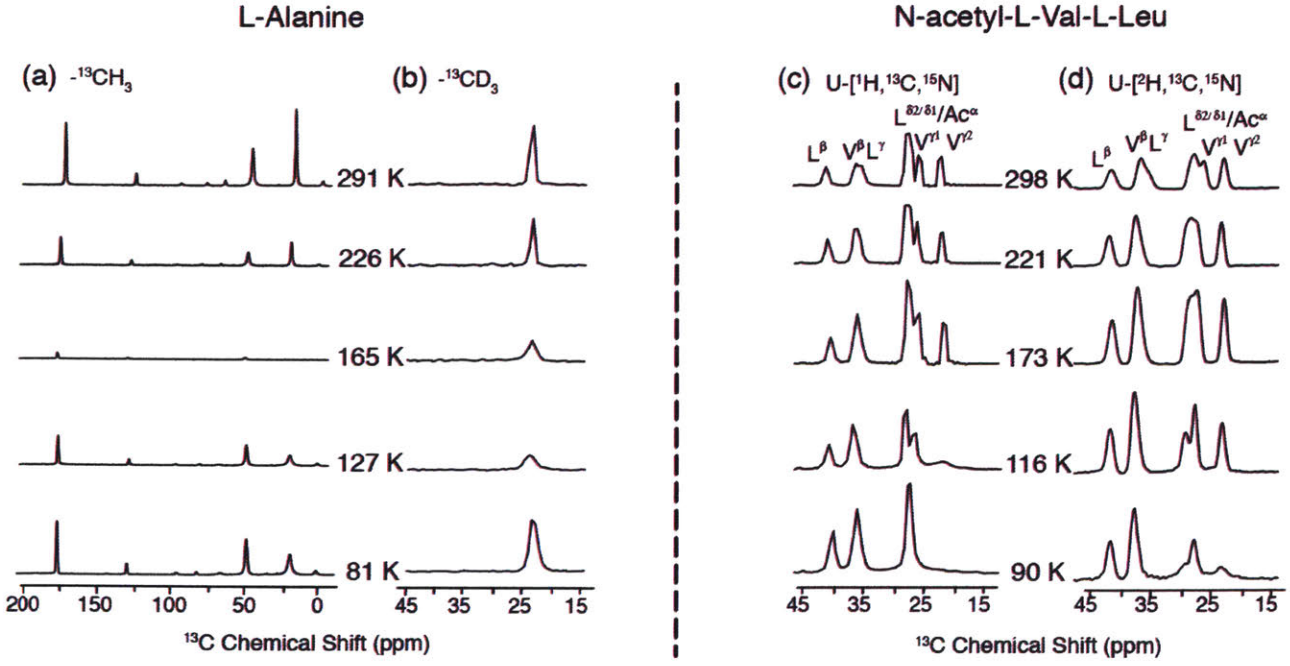

Figure 3.5 Temperature dependent ^{13}C MAS spectra of (a) [U-^{13}C, ^{15}N]-Ala with a $^{13}CH_3$; (b)Ala-$^{13}CD_3$; (c) [U-^{1}H, ^{13}C, ^{15}N] N-acetyl-L-Val-L-Leu (d) [U-^{2}H, ^{13}C, ^{15}N] N-acetyl-L-Val-L-Leu. The spectra were acquired with $\omega_r/2\pi$ = 6.2 kHz, $\omega_{1H}/2\pi$ = 100 kHz for TPPM decoupling.

It would clearly be desirable to recover the signal loss due to the interference between molecular dynamics and decoupling, and accordingly, we have examined the possibility of labeling methyl groups as $-CD_3$'s.[36, 37] The rationale behind this approach is that the 1st order ^2H quadrupole coupling is inhomogeneous, the 2nd order ^2H coupling is small at high fields, and ^2H-^2H dipole couplings, proportional to γ_I^2, are a factor of 42 smaller than ^1H-^1H dipole couplings. Thus, MAS itself should average the ^2H-^2H and ^2H-^{13}C dipolar couplings and attenuate the intensity losses. Figure 5 shows temperature-dependent spectra obtained from the monomeric amino acid alanine containing either a $-CH_3$ or $-CD_3$ group. As expected the ^{13}C MAS spectra obtained from Ala-$^{13}CH_3$ exhibit dramatic intensity losses around 165 K. Note that the intensity also decreases uniformly across the spectrum and both the C_α and C_o resonances are effectively suppressed as was the case in APG (Figure 3.2). However, with the $-^{13}CD_3$ present, the Ala methyl line is not suppressed at 165 K and the intensity recovers at 81 K. Nevertheless, there is still considerable intensity loss at 165 K, and, as discussed below, this is probably due to the $-CD_3$ methyl hopping rate (~10^4-10^5 s^{-1}) being similar to magic angle spinning frequency. By interpolating the data from the Arrhenius plot reported by Beshah et al. for Ala–CD_3, we obtain hopping rates of 1.4 x 10^5 at 165 K and 1.6 x 10^3 at 127 K,[38] which confirms our hypothesis.

To explore the intensity losses in two other amino acids, namely Leu and Val, we recorded spectra of protonated and $-CD_3$ labeled N-Ac-VL. As shown in Figure 5c, the Val γ_1 and γ_2 lines in protonated N-Ac-VL exhibit significant intensity losses and are absent in the spectrum for T<116 K. Note also that the line from $V^{\gamma 2}$ disappears in the interval 116-173 K whereas the $V^{\gamma 1}$ line persists to ~116 K. This behavior is consistent with the fact that the threefold hopping rates, measured with ^2H spectra, for the two $-CH_3$ groups in Val differ by about an order of magnitude[38]. Specifically, in N-Ac-DL-Val they are 4.8 x 10^5 and 2.8 x 10^6 at 118 K, and therefore, the signal intensities of the methyl groups at 116 K (Figure 3.5d) are not severely attenuated and still detectable as the hopping rates are ~1-2 order of magnitude away from the interference regime (~10^4-10^5 s^{-1}). In contrast, the Leu–CH_3 line does not lose intensity even at 90 K and it can potentially be used for distance measurements at low temperatures. In deuterated N-Ac-VL, both groups are present at 90 K but with reduced intensity.

In DNP enhanced spectra of uniformly labeled bR, the intensity of methyl containing residues is also reduced. Figure 6a shows a 2D RFDR spectrum of ^1H uniformly labeled bR at 190 K with cross peaks corresponding to the 29 Ala and 18 Thr $-CH_3$'s in bR that are not resolved at 380 MHz. In contrast, at 90 K (Figure 3.6b) the Ala $C_{\beta\alpha}$ cross-peaks is no longer

observed in the ^{1}H bR sample while it is detected in the ^{2}H uniformly labeled bR. Similarly, $Thr_{\gamma 2\beta}$ cross-peaks are partially attenuated in the ^{1}H spectrum compared to that at 190 K, but it is fully recovered in the spectrum of ^{2}H bR. This further verifies that an effective solution of methyl group attenuation could involve deuteration.

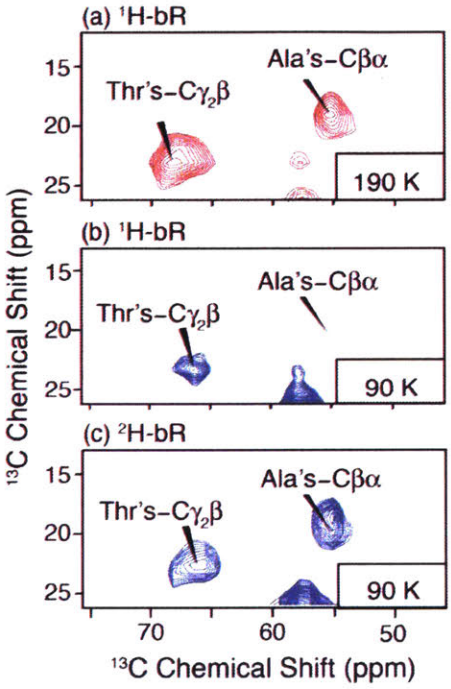

Figure 3.6 2D DNP enhanced ^{13}C-^{13}C RFDR spectra of (A) U-^{1}H,^{13}C,^{15}N bR doped with 5 mM AMUPol at 190 K, (B) 92 K and (C) 2D RFDR of U-^{2}H, ^{13}C,^{15}N bR containing 15mM TOTAPOL at 92 K. (B) and (C) were acquired with DNP microwave irradiation. Enhancements of 75 and 71 were obtained, respectively. All spectra were acquired with 2ms mixing, 30 kHz ^{13}C pulses and 100 kHz ^{1}H decoupling and spinning frequency $\omega_r/2p$= 7 kHz at $w_{0H}/2p$= 380 MHz. Both experiments took 7 hours with 6 s recycle delay, 128 t_1 increments, and 32 scans per increment.

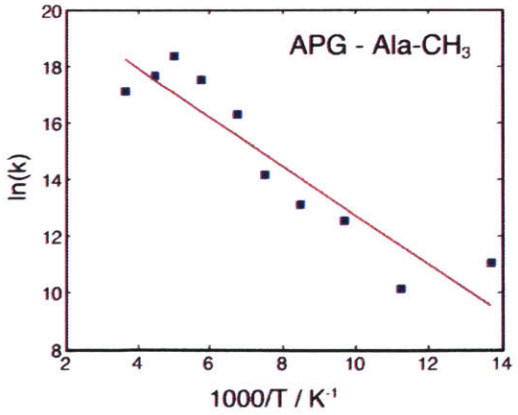

Figure 3.7 Arrhenius plot of three-site hopping rate of the Ala $-CH_3$ group in APG. The least-square fit (red line) yields an activation energy E_a of 7.2 ± 1 kJ/mol and pre-exponential constant A of ~ 2 x 10^{9} s^{-1}.

Although the loss of signal intensity of the methyl groups at low temperature impedes many NMR experiments, including distance measurements, it encodes useful information the site-specific about the dynamics of group, for instance the activation energy, E_a. The activation energy contains rich details about the local chemical and structural environment, and they can be extracted by first comparing experimental data at different temperatures with numerical simulations. **Figure 3.7** shows the Arrhenius plot of the $-CH_3$ group hoping rates of alanine extracted from simulations of the signal intensities in APG measured by observing ^{13}C signals directly using a Bloch decay in the presence of ^{1}H decoupling. (data from **Figure 3.3c)**. The least-square fit yields an activation energy E_a of 7.2 ± 1 kJ/mol. This value is lower than the literature value of 20.0 kJ/mol[39] obtained for the monomeric amino acid alanine. The activation energy of the $-CH_3$ group in alanine is higher than that in the APG probably due to tighter crystal packing and thus more restricted rotation. Hence, the higher barrier for threefold hopping. However, this analysis is complicated by the fact that the methyl group is not strictly an isolated system, i.e. it is coupled to the nearby proton bath, especially the $-NH_3^+$ group via spin diffusion. A more detailed study of this effect on the activation energy can be performed by deuteration of the NH_3^+ group.

3.4 DISCUSSION

It is well known that the hopping rates of $-CH_3$ and $-NH_3^+$ groups can be measured precisely by analyzing the ^{2}H lineshape of the deuterated analogs of these groups.[36-39] Alternatively, Long *et al.* showed a strong correlation between the intensity of Bloch decay signals of ^{15}N and the hopping rate in $-NH_3^+$.[37] Using the same approach, we acquired ^{13}C Bloch decay signals (**Figure 3.3c**) and assigned the signal minimum at ~112 K to the interference between the methyl group hopping and the ^{1}H decoupling. Furthermore, the small signal attenuation (10%) of Pro-C_α and Gly-C_o from Bloch decay experiments (**Figure 3.3c**) cannot account for the large signal loss (60%) of the same resonances from CP experiments (**Figure 3.3b**), suggesting that the methyl group hopping also causes inefficient CP at this temperature. This suggests that the hopping rate of the methyl group in APG at ~112 K is ~10^4-10^5 s^{-1}, i.e. same order of magnitude as the MAS frequency and/or ^{1}H decoupling regime. The hopping rate can be extracted from the fitted Arrhenius plot (**Figure 3.7**) and we obtained a hopping rate of ~7 x 10^5 s^{-1}, thus confirming our hypothesis.

In practice, the decoupling field and the spin-locking field are very close in strength. Thus, it is expected that interferences between these Rabi fields and the 3-site hopping occur at the

same temperature. Interference between the spin-locking field and the molecular dynamics is clearly the dominant mechanism responsible for the signal minimum at ~173 K in the ^{1}H-^{13}C CP data, (**Figure 3.3b**) which does not appear in the ^{13}C Bloch decay data (**Figure 3.3c**). At this matching condition, the spin-lock is inefficient for methyl ^{1}H's, causing a short ^{1}H $T_{1\rho}$. Furthermore, due to rapid ^{1}H-^{1}H spin diffusion and the combination of intra- and inter-molecular contacts, the effect of a short $T_{1\rho}$ of the methyl ^{1}H's readily distributes itself throughout the molecule, resulting in a uniform signal loss at ~173 K in the ^{1}H-^{13}C CP data (**Figure 3.3b**). In contrast, the destructive interference effect on the decoupling appears to be more localized to the $-CH_3$ and $-NH_3^+$. This is apparent in the signal minimum at ~112 K in **Figure 3.3b** and **3.3c** as well as in the signal loss at ~173 K in the ^{1}H-^{15}N CP data, (**Figure 3.3d**) which is due to interference of $-NH_3^+$ hopping with both the decoupling and spin-lock fields.

The diffusive hopping of $-CH_3$ causes the first minimum at ~112 K, and the second at ~173 K is also caused by the similar phenomenon involving the $-NH_3^+$ group. The temperature or hopping rate at which the signal intensity is minimum is governed by both the E_a and the pre-exponential factor of the Arrhenius equation, A. However, if the values of A are comparable, then by comparing the previously published E_a values, one can predict the temperature range at which the intensity is minimum. The higher activation energy of the $-NH_3^+$ group is due to its ability to form hydrogen bonds.[37] For example, the E_a in Ala for $-ND_3^+$ is 40.5 kJ/mol,[37] whereas that for the $-CD_3$ group is 20.0 kJ/mol.[39] Long has shown the E_a of CD_3 and CH_3 groups are comparable. Similar to the case of $-CH_3$, Long *et al.* shows that the hopping rate of $-NH_3^+$ in Ala reaches 5×10^4 s^{-1} at 243 K, which is significantly higher than 173 K implied by our data, pointing to lower activation energy in APG, given that the values of A are comparable in both cases.

Our hypothesis on the correlation between molecular packing/ flexibility and the E_a is further supported by the data on larger systems including the membrane protein bR (**Figure 3.4a** and **3.4b**) and amyloid fibrils of PI3-SH3 (**Figure 3.4c** and **3.4d**). In contrast to the tripeptide APG, in bR and PI3-SH3 the hopping effect appears to be localized to the methyl groups. In [FVYL-^{13}C,^{15}N] PI3-SH3, a sample in which only methyl groups of Val and Leu are labeled, we are able to observe the minimum in the intensity of the $-CH_3$ groups at ~95 K, compared to ~112 K in APG, suggesting a lower E_a.

Our observations have a direct implication for the application of DNP to problems in structural biology. Carbonyl ^{13}C's, together with the aromatic side chains, are the least affected by the molecular dynamics and exhibit excellent sensitivity at low temperatures. This validates

the approach using low temperature DNP to obtain long-range intermolecular distances involving aromatic side chains[71]. Similarly, methyl groups are of proven importance in measuring long-range contacts in proteins due to their position at the termini of many amino acid side chains. Interestingly, as demonstrated by the data here, one cannot use DNP experiments in the 80-120 K temperature range to measure distances associated with certain protonated ($-CH_3$) methyl groups. As hinted by the partial recovery of the methyl carbons at 87 K in **Figure 3.3 and 3.4,** the brute force solution to this problem is to perform experiments at even lower temperatures, which would then require cooling using liquid helium. A promising alternative approach is to fully or partially deuterate the methyl groups and it was demonstrated some time ago that full deuteration largely prevents the intensity losses observed here.[36] Thus, the benefit of this approach is twofold. First, it circumvents the detrimental intensity losses while maintaining sufficient CP from adjacent protons. Second, deuteration of proteins has been demonstrated to increase DNP enhancements by a factor of 3-4.[31]

We have initiated the investigation of such an approach. In particular, in **Figure 3.5** we compared spectra of alanine with $-CD_3$ and $-CH_3$ methyl groups as well as between protonated and fully deuterated N-acetyl-L-Val-L-Leu. The methyl group $-CH_3$ of alanine disappears completely at 165 K while alanine $-CD_3$ signal experiences some level of attenuation but nevertheless survives. In N-Ac-VL, the Val $C_{\gamma 1}$ and $C_{\gamma 2}$ possess different activation energies, resulting in their disappearance at different temperatures, 90 K and 116 K respectively. This behavior is delayed in the perdeuterated N-Ac-VL spectra, and more importantly, valine $C_{\gamma 1}$ and $C_{\gamma 2}$ signals can still be observed at 90 K. These two carbons in N-Ac-Val were reported to have distinct E_a's of 15.3 and 22.2 kJ/mol.[38] Our results suggest that it is possible to maintain the signals from methyl groups at low temperature by deuteration. Further investigations including the incorporation of deuterium decoupling are underway and will be the topic of the subsequent studies.

It is worth noting that the signal loss at ~243 K can be as large as ~70% in the case of bR and occurs in the neighborhood of, but above, the temperature normally associated with the protein glass transition. It appears that two mechanisms could be responsible for this effect. First, this intensity loss could be due to the freezing of glycerol/water mixture. Thus, the signal attenuation is related to the hydration of the sample and protein-water interactions and is, therefore, ubiquitous in biological samples. Second, the loss could also be due to the 2-site flipping of phenyl rings. bR contains 13 Phe's and 11 Tyr's in the amino acid sequence and preliminary ^2H NMR data show intermediate exchange flipping rates at this temperature. We

believe this is important since protein samples are frequently studied at temperatures slightly lower than room temperature to slow some dynamic processes. Our results suggest that this approach may be suboptimal in term of the overall sensitivity. It is therefore desirable to perform such experiments at even lower temperatures, but to date, these temperatures are not always achievable due to instrumental limitations.

Finally, the main focus of this article is to address the effect of temperature on the line intensity of the $-CH_3$ group, along with solutions to alleviate the line-broadening effect at certain temperatures due to interference between hopping mechanism with MAS frequency and/or ^1H decoupling and/or CP. While such interference is problematic for some experiments, this temperature-dependent phenomena can be exploited and used to extract useful dynamic information about the system. Thus, we present here a new method to extract the activation energy of the$-CH_3$ group (**Figure 3.7**) by monitoring the change of ^{13}C signal intensities as a function of temperature. We are currently applying this novel approach to investigate the site-specific motions of other biological macromolecules like proteins, which could reveal important relations between the dynamics and functions of proteins.

3.5 CONCLUSION

In summary, we report effects of molecular motions on NMR signals of peptide and protein samples at cryogenic temperatures. In the microcrystalline tripeptide APG, a first-order polymorphic phase transition occurs at 225 K, which manifests itself in the line doubling in ^{13}C NMR spectra. At lower temperatures, we observe a destructive interference effect from the threefold jump diffusion of the Ala-CH_3 (at ~112 K) and of the Ala-NH_3^+ (at ~173 K) on the proton decoupling and/or the CP spin-lock fields. The effect on the decoupling appears to be localized, whereas the effect on the CP is readily transmitted throughout the molecule due to fast ^1H-^1H spin diffusion in a strongly coupled ^1H bath.

We extend these experiments to larger biological systems consisting of the membrane protein bacteriorhodopsin and amyloid fibrils formed from PI3-SH3. At ~243 K, both samples exhibit significant signal loss, in the neighborhood of the protein glass transition. Similar to the case of APG, the methyl groups are attenuated at low temperatures. However, the effect does not propagate in an obvious way to other parts of the spectrum, which supports the approach of using low temperature DNP to obtain long-range distances involving aromatic side chains. Furthermore, the intensity minima occur at lower temperatures in these biological systems than in APG (95 K vs. 112 K). Simulations of the intensity losses for the $-CH_3$ group in APG suggest that it should be possible to use similar data to extract site-specific information on molecular

dynamics. Finally, our study suggests deuteration of the methyl groups as $-CD_3$ as another probe of long-range distance constraints using DNP at liquid nitrogen temperatures.

3.6 SUPPORTING INFORMATION

Spin-lattice relaxation, T_1 for ^{13}C and ^{1}H measured with saturation recovery. Temperature dependence of ^{13}C Bloch decay spectra of APG. Full set of temperature-dependent ^{1}H-^{13}C CP spectra of [^{13}C,^{15}N-FVYL]-PI3-SH3. Full set of temperature-dependent ^{1}H-^{13}C CP spectra of bR. 1D ^{1}H-^{13}C CP spectra and 2D RFDR DNP spectrum of [^{13}C,^{15}N-FVYL]-PI3-SH3 fibril.

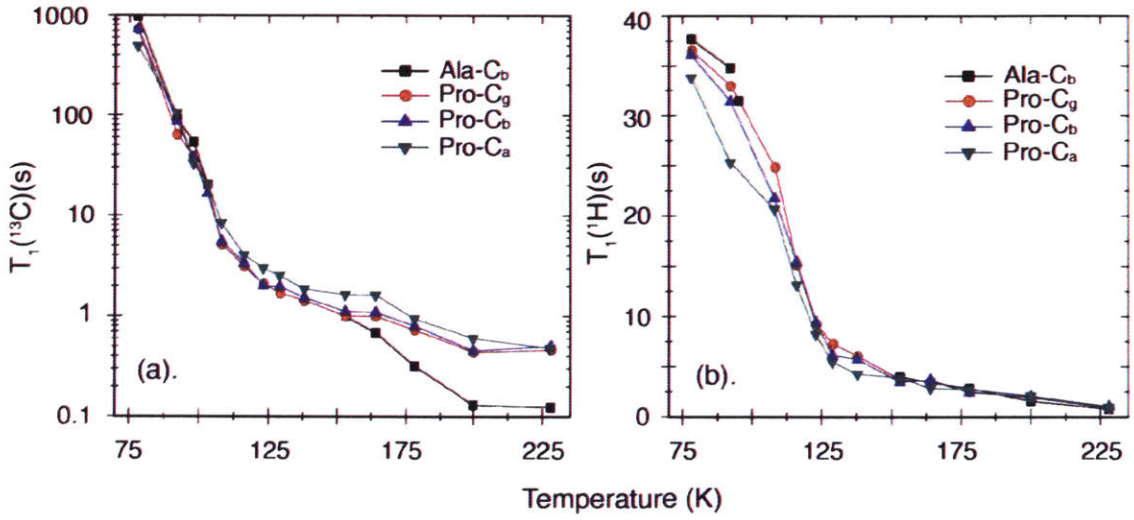

Figure 3.8 ^{13}C CP MAS Spin lattice relaxation, T_1 values at different temperatures for ^{13}C (right) and ^{1}H (left) measured with saturation recovery experiments. The T_1 values were acquired with $\omega_r/2\pi$ = 4.83 kHz, $\omega_{1H}/2\pi$ = 83 kHz for TPPM decoupling and $\omega_{0H}/2\pi$ =380 MHz.

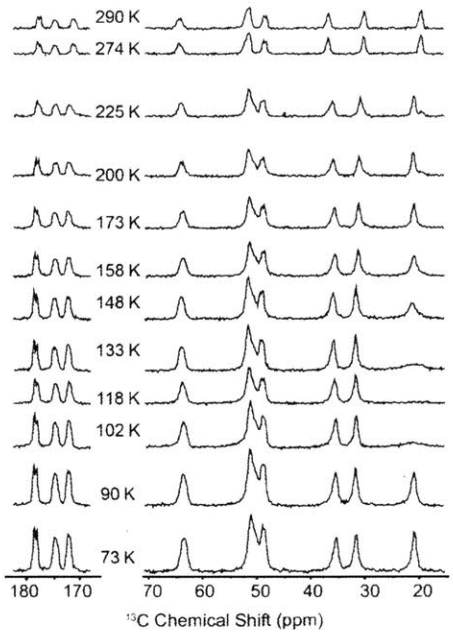

Figure 3.9 Temperature-dependent direct ^{13}C spectra of [U-^{13}C,^{15}N] APG. The spectral changes are plotted in **Figure 3c**. The spectra were acquired with $\omega_r/2\pi$ = 4.83 kHz, $\omega_{1H}/2\pi$ = 83 kHz for TPPM decoupling and $\omega_{0H}/2\pi$ =380 MHz.

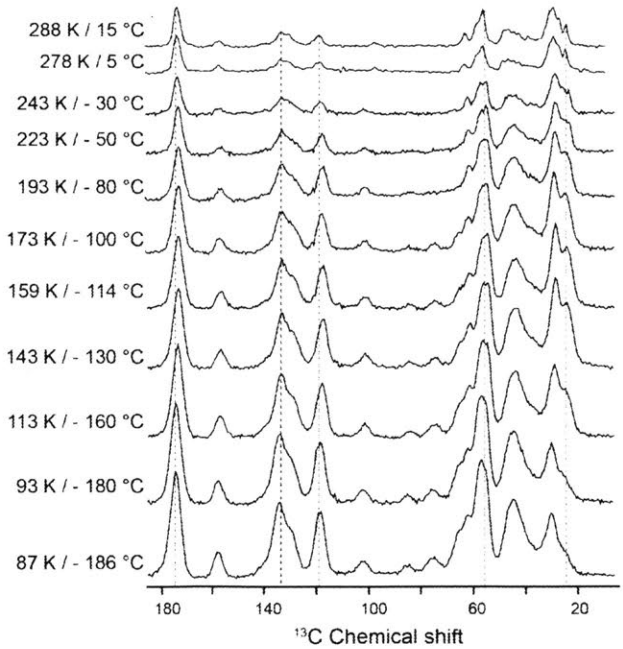

Figure 3.10 Temperature-dependent ^1H-^{13}C CP spectra of [^{13}C,^{15}N- FVYL]-PI3-SH3 amyloid fibrils. Sample was cryoprotected in d_8-glycerol/D_2O/H_2O (60/30/10 volume ratio). $\omega_r/2\pi$ = 7 kHz, $\omega_{1H}/2\pi$ = 100 kHz for TPPM decoupling and $\omega_{0H}/2\pi$ =380 MHz.

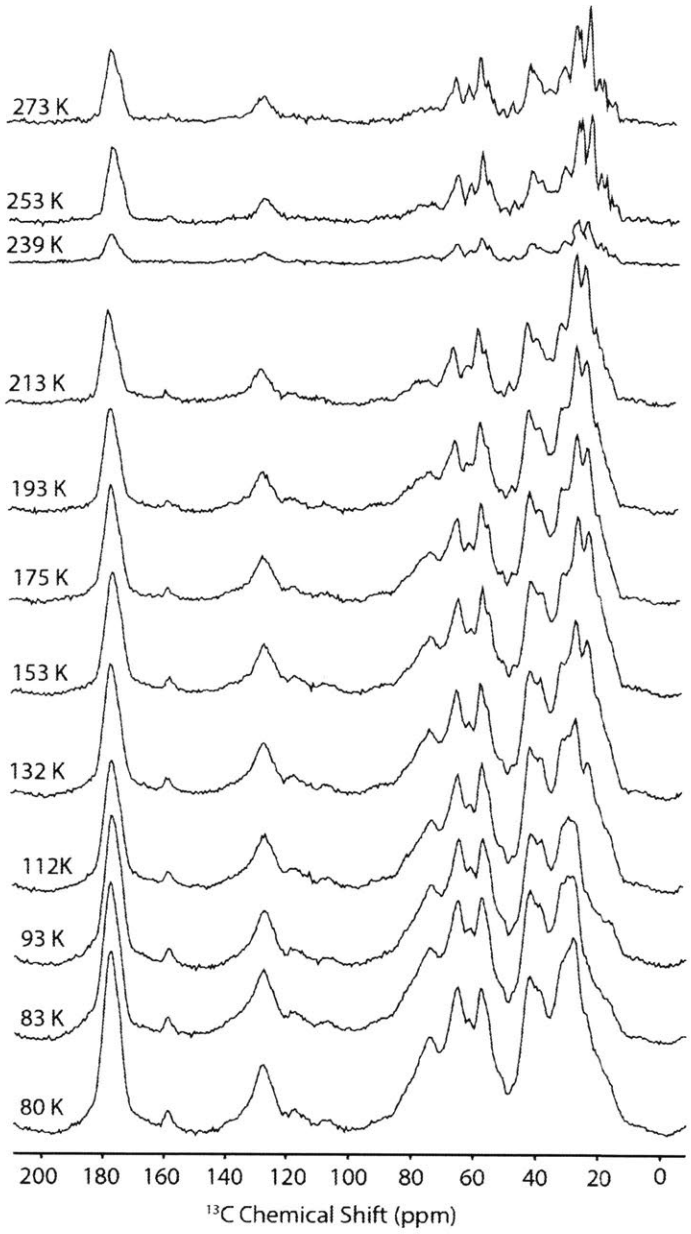

Figure 3.11 Temperature-dependent ^{1}H-^{13}C CP spectra of [^{13}C,^{15}N]- bacteriorhodopsin. Sample was cryoprotected in d_8-glycerol/D_2O/H_2O (60/30/10 volume ratio). $\omega_r/2\pi$ = 4.83 kHz, $\omega_{1H}/2\pi$ = 100 kHz for TPPM decoupling and $\omega_{0H}/2\pi$ =380 MHz.

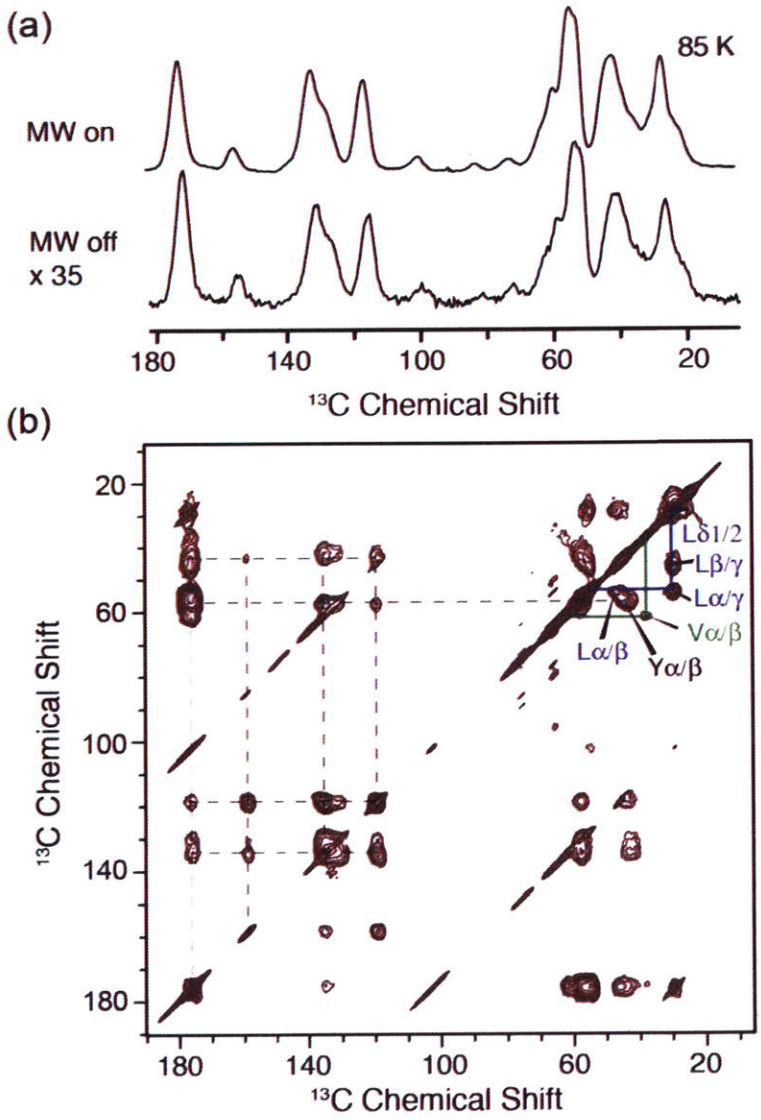

Figure 3.12 DNP-enhanced 1D and 2D spectra of [^{13}C,^{15}N-FVYL]-PI3-SH3 fibrils. (a)^{1}H-^{13}C CP MAS NMR spectra at 88 K measured with (top) and without (bottom) DNP, an enhancement of 35 was obtained. The fibril was hydrated in 60/30/10 volume ratio of d_8-glycerol/D_2O/H_2O supplemented with 15 mM TOTAPOL. (b) DNP-enhanced 2D ^{13}C-^{13}C RFDR acquired with 1.6 ms of mixing time and a total experiment time of 4 hours. The dashed lines indicate the spin systems of tyrosine residues. The spectra were acquired with $\omega_r/2\pi$ = 7 kHz, $\omega_{1H}/2\pi$ = 83 kHz for TPPM decoupling, and $\omega_{0H}/2\ \pi$ =380 MHz.

The enhanced intensity greatly accelerates the acquisition of multidimensional spectra and allows the investigation of low-temperature structural and dynamic behaviors such as conformational disorder, polymorphism, and backbone and side chain motions. In the 2D RFDR spectrum of [^{13}C,^{15}N-FVYL]-PI3-SH3, methyl containing valine and leucine residues are recovered at 85 K.

Notes S1. GAMMA simulation parameters.

Details of the parameters used can be found in SI. In order to simulate the three-site hopping mechanism, the simulations were carried out in a composite Liouvillian space that facilitates mutual-exchange mechanism. The dimensions of the exchange matrices for the four-spin $\mathbf{CH_3}$ and $\mathbf{CD_3}$ spin systems are 256 x 256 and 2916 x 2916 respectively. The amount of time required to simulate the FID of one crystallite orientation using one CPU core is ~1 minute and ~1.5 days for $\mathbf{CH_3}$ and $\mathbf{CD_3}$ respectively. All simulations took ~2 weeks to compute using ETH Brutus cluster with 384 CPU cores. The parameters chosen for the simulations are $\omega_r/2\pi$=4.651 kHz, TPPM decoupling $\omega_{1H}/2\pi$= 83 kHz with 6.9 μs pulses and phases ±15 degree. The size of the quadrupole coupling used for ^{2}H nuclei is 167 kHz.

ABBREVIATIONS

MAS: magic angle spinning; NMR: nuclear magnetic resonance; ssNMR: solid state NMR; CP: cross polarization; DNP: dynamic nuclear polarization; RF: radio frequency; RFDR: radio frequency-driven recoupling; S/N: signal to noise ratio; APG: alanyl-prolyl-glycine; bR: bacteriorhodopsin; PI3-SH3: phosphatydinal-inositol-3-kinase SH3 domain.

3.7 ACKNOWLEDGMENT

Funding Sources

This work was supported by grants (EB-001960, EB-002804, EB-002026 and EB-001035) from the National Institute of Biomedical Imaging and Bioengineering. B. Corzilius was partially funded by a DFG Research Fellowship CO802/1-1. K.O. Tan is supported by Early Postdoc Mobility grant -165285 provided by the Swiss National Science Foundation (SNSF).

We would like to thank Jeffrey Bryant, Ajay Thakkar and Michael Mullins for their technical assistance and Drs. Sudheer Jawla and Richard Temkin for helping with DNP instrumentation. We would like to thank Prof. Matthias Ernst for useful discussions regarding the simulations. We are grateful to Dr. Marina Belenky and Angela Jacavone for the preparation of bR, PI3-SH3 samples, respectively.

3.8 References

1. Renault, M.; Cukkemane, A.; Baldus, M. Solid-State Nmr Spectroscopy on Complex Biomolecules. *Angew. Chem.-Int. Edit.* **2010,** *49,* 8346-8357.
2. Lesage, A. Recent Advances in Solid-State Nmr Spectroscopy of Spin I=1/2 Nuclei. *Phys. Chem. Chem. Phys.* **2009,** *11,* 6876-6891.
3. Lange, A.; Becker, S.; Seidel, K.; Giller, K.; Pongs, O.; Baldus, M. A Concept for Rapid Protein-Structure Determination by Solid-State Nmr Spectroscopy. *Angew. Chem.-Int. Edit.* **2005,** *44,* 2089-2092.
4. Cady, S. D.; Schmidt-Rohr, K.; Wang, J.; Soto, C. S.; DeGrado, W. F.; Hong, M. Structure of the Amantadine Binding Site of Influenza M2 Proton Channels in Lipid Bilayers. *Nature* **2010,** *463,* 689-U127.
5. Castellani, F.; van Rossum, B. J.; Diehl, A.; Rehbein, K.; Oschkinat, H. Determination of Solid-State Nmr Structures of Proteins by Means of Three-Dimensional 15n-13c-13c Dipolar Correlation Spectroscopy and Chemical Shift Analysis. *Biochemistry* **2003,** *42,* 11476-11483.
6. Brown, S. P.; Spiess, H. W. Advanced Solid-State Nmr Methods for the Elucidation of Structure and Dynamics of Molecular, Macromolecular, and Supramolecular Systems. *Chem. Rev.* **2001,** *101,* 4125-4155.
7. Wel, P.; Lewandowski, J.; Griffin, R. Solid-State Nmr Study of Amyloid Nanocrystals and Fibrils Formed by the Peptide Gnnqqny from Yeast Prion Protein Sup35p. *J. Am. Chem. Soc.* **2007,** *129,* 5117-5130.
8. Andreas, L. B.; Reese, M.; Eddy, M. T.; Gelev, V.; Ni, Q. Z.; Miller, E. A.; Emsley, L.; Pintacuda, G.; Chou, J. J.; Griffin, R. G. Structure and Mechanism of the Influenza a M2(18-60) Dimer of Dimers. *J. Am. Chem. Soc.* **2015,** *137,* 14877-14886.
9. Can, T. V.; Sharma, M.; Hung, I.; Gor'kov, P. L.; Brey, W. W.; Cross, T. A. Magic Angle Spinning and Oriented Sample Solid-State Nmr Structural Restraints Combine for Influenza a M2 Protein Functional Insights. *Journal of the American Chemical Society* **2012,** *134,* 9022-9025.
10. De Paepe, G. Dipolar Recoupling in Magic Angle Spinning Solid-State Nuclear Magnetic Resonance. *Annu. Rev. Phys. Chem.* **2012,** *63,* 661-684.
11. Rienstra, C. M. Magic-Angle Spinning Recoupling Techniques for Distance Determinations among Spin-1/2 Nuclei in Solid Peptides and Proteins. *NMR Spectrosc. Biol. Solids* **2006,** 1-38.
12. Ernst, M.; Meier, B. H., Adiabatic Polarization-Transfer Methods in Mas Spectroscopy. In *Encyclopedia of Magnetic Resonance*, John Wiley & Sons, Ltd: 2007.
13. Bjerring, M.; Rasmussen, J. T.; Krogshave, R. S.; Nielsen, N. C. Heteronuclear Coherence Transfer in Solid-State Nuclear Magnetic Resonance Using a Gamma-Encoded Transferred Echo Experiment. *J. Chem. Phys.* **2003,** *119,* 8916.
14. Ernst, M. Heteronuclear Spin Decoupling in Solid-State Nmr under Magic-Angle Sample Spinning. *J. Magn. Reson.* **2003,** *162,* 1-34.
15. Mithu, V. S.; Pratihar, S.; Paul, S.; Madhu, P. K. Efficiency of Heteronuclear Dipolar Decoupling Schemes in Solid-State Nmr: Investigation of Effective Transverse Relaxation Times. *J. Magn. Reson.* **2012,** *220,* 8-17.
16. Mithu, V. S.; Paul, S.; Kurur, N. D.; Madhu, P. K. Heteronuclear Dipolar Decoupling in Solid-State Nuclear Magnetic Resonance under Ultra-High Magic-Angle Spinning. *J. Magn. Reson.* **2011,** *209,* 359-363.
17. Van Beek, J. D.; Carravetta, M.; Antonioli, G. C.; Levitt, M. H. Spherical Tensor Analysis of Nuclear Magnetic Resonance Signals. *J. Chem. Phys.* **2005,** *122,* 244510/244511.
18. Zhao, X.; Hoffbauer, W.; Schmedt auf der Gunne, J.; Levitt, M. H. Heteronuclear Polarization Transfer by Symmetry-Based Recoupling Sequences in Solid-State Nmr. *Solid State Nucl. Magn. Reson.* **2004,** *26,* 57.

19. Drobny, G. P.; Long, J. R.; Karlsson, T.; Shaw, W.; Popham, J.; Oyler, N.; Bower, P.; Stringer, J.; Gregory, D.; Mehta, M., et al. Structural Studies of Biomaterials Using Double-Quantum Solid-State Nmr Spectroscopy. *Annu. Rev. Phys. Chem.* **2003,** *54,* 531-571.
20. LeMaster, D. M.; Kushlan, D. M. Dynamical Mapping of E. Coli Thioredoxin Via 13c Nmr Relaxation Analysis. *J. Am. Chem. Soc.* **1996,** *118,* 9255-9264.
21. Hong, M. Determination of Multiple Φ-Torsion Angles in Proteins by Selective and Extensive 13c Labeling and Two-Dimensional Solid-State Nmr. *J. Magn. Reson.* **1999,** *139,* 389-401.
22. Castellani, F.; van Rossum, B.; Diehl, A.; Schubert, M.; Rehbein, K.; Oschkinat, H. Structure of a Protein Determined by Solid-State Magic-Angle-Spinning Nmr Spectroscopy. *Nature* **2002,** *420,* 98-102.
23. Jones, D. H.; Cellitti, S. E.; Hao, X.; Zhang, Q.; Jahnz, M.; Summerer, D.; Schultz, P. G.; Uno, T.; Geierstanger, B. H. Site-Specific Labeling of Proteins with Nmr-Active Unnatural Amino Acids. *J. Biomol. NMR* **2010,** *46,* 89-100.
24. Davis, L.; Chin, J. W. Designer Proteins: Applications of Genetic Code Expansion in Cell Biology. *Nat. Rev. Mol. Cell Biol.* **2012,** *13,* 168-182.
25. Concistre, M.; Johannessen, O. G.; Carignani, E.; Geppi, M.; Levitt, M. H. Magic-Angle Spinning Nmr of Cold Samples. *Acc. Chem. Res.* **2013,** *46,* 1914-1922.
26. Abragam, A., *The Principles of Nuclear Magnetism.* Clarendon Press: Oxford, 1961; Vol. International series of monographs on physics, p 599 p.
27. Can, T. V.; Ni, Q. Z.; Griffin, R. G. Mechanisms of Dynamic Nuclear Polarization in Insulating Solids. *J. Magn. Reson.* **2015,** *253,* 23-35.
28. Gelis, I.; Vitzthum, V.; Dhimole, N.; Caporini, M. A.; Schedlbauer, A.; Carnevale, D.; Connell, S. R.; Fucini, P.; Bodenhausen, G. Solid-State Nmr Enhanced by Dynamic Nuclear Polarization as a Novel Tool for Ribosome Structural Biology. *J. Biomol. NMR* **2013,** *56,* 85-93.
29. Barnes, A. B.; De Paëpe, G.; van der Wel, P. C. A.; Hu, K. N.; Joo, C. G.; Bajaj, V. S.; Mak-Jurkauskas, M. L.; Sirigiri, J. R.; Herzfeld, J.; Temkin, R. J., et al. High-Field Dynamic Nuclear Polarization for Solid and Solution Biological Nmr. *Applied Magnetic Resonance* **2008,** *34,* 237-263.
30. Maly, T.; Debelouchina, G. T.; Bajaj, V. S.; Hu, K.-N.; Joo, C.-G.; Mak-Jurkauskas, M. L.; Sirigiri, J. R.; van der Wel, P. C. A.; Herzfeld, J.; Temkin, R. J., et al. Dynamic Nuclear Polarization at High Magnetic Fields. *The Journal of Chemical Physics* **2008,** *128,* 052211-052219.
31. Akbey, Ü.; Franks, W. T.; Linden, A.; Lange, S.; Griffin, R. G.; Rossum, B.-J. v.; Oschkinat, H. Dynamic Nuclear Polarization of Deuterated Proteins. *Angew. Chem.-Int. Edit.* **2010,** *49,* 7803-7806.
32. Bajaj, V. S.; Mak-Jurkauskas, M. L.; Belenky, M.; Herzfeld, J.; Griffin, R. G. Functional and Shunt States of Bacteriorhodopsin Resolved by 250 Ghz Dynamic Nuclear Polarization-Enhanced Solid-State Nmr. *Proc. Natl. Acad. Sci. U.S.A.* **2009,** *106,* 9244-9249.
33. Mak-Jurkauskas, M. L.; Bajaj, V. S.; Hornstein, M. K.; Belenky, M.; Griffin, R. G.; Herzfeld, J. Energy Transformations Early in the Bacteriorhodopsin Photocycle Revealed by Dnp-Enhanced Solid-State Nmr. *Proc. Natl. Acad. Sci. U.S.A.* **2008,** *105,* 883-888.
34. Becker-Baldus, J.; Bamann, C.; Saxena, K.; Gustmann, H.; Brown, L. J.; Brown, R. C. D.; Reiter, C.; Bamberg, E.; Wachtveitl, J.; Schwalbe, H., et al. Enlightening the Photoactive Site of Channelrhodopsin-2 by Dnp-Enhanced Solid-State Nmr Spectroscopy. *Proc. Natl. Acad. Sci. U. S. A.* **2015,** *112,* 9896-9901.
35. Fricke, P.; Demers, J. P.; Becker, S.; Lange, A. Studies on the Mxih Protein in T3ss Needles Using Dnp-Enhanced Ssnmr Spectroscopy. *Chemphyschem* **2014,** *15,* 57-60.
36. Maus, D. C.; Copie, V.; Sun, B.; Griffiths, J. M.; Griffin, R. G.; Luo, S.; Schrock, R. R.; Liu, A. H.; Seidel, S. W.; Davis, W. M., et al. A Solid-State Nmr Study of Tungsten Methyl Group Dynamics in $[W(H^5\text{-}C_5me_5)Me_4][Pf_6]$. *J. Am. Chem. Soc.* **1996,** *118,* 5665-5671.

37. Long, J. R.; Sun, B. Q.; Bowen, A.; Griffin, R. G. Molecular Dynamics and Magic Angle Spinning Nmr. *J. Am. Chem. Soc.* **1994,** *116,* 11950-11956.
38. Beshah, K.; Griffin, R. G. Deuterium Quadrupole Echo Nmr Study of Methyl Group Dynamics in N-Acetyl-Dl-(Γ-D6)-Valine. *J. Magn. Reson.* **1989,** *84,* 268-274.
39. Beshah, K.; Olejniczak, E. T.; Griffin, R. G. Deuterium Nmr Study of Methyl Group Dynamics in L-Alanine. *J. Chem. Phys.* **1987,** *86,* 4730-4736.
40. Linser, R.; Sarkar, R.; Krushelnitzky, A.; Mainz, A.; Reif, B. Dynamics in the Solid-State: Perspectives for the Investigation of Amyloid Aggregates, Membrane Proteins and Soluble Protein Complexes. *J. Biomol. NMR* **2014,** *59,* 1-14.
41. Vugmeyster, L.; Ostrovsky, D.; Ford, J. J.; Burton, S. D.; Lipton, A. S.; Hoatson, G. L.; Vold, R. L. Probing the Dynamics of a Protein Hydrophobic Core by Deuteron Solid-State Nuclear Magnetic Resonance Spectroscopy. *Journal of the American Chemical Society* **2009,** *131,* 13651-13658.
42. Vugmeyster, L.; Ostrovsky, D.; Khadjinova, A.; Ellden, J.; Hoatson, G. L.; Vold, R. L. Slow Motions in the Hydrophobic Core of Chicken Villin Headpiece Subdomain and Their Contributions to Configurational Entropy and Heat Capacity from Solid-State Deuteron Nmr Measurements. *Biochemistry* **2011,** *50,* 10637-10646.
43. Vugmeyster, L.; Ostrovsky, D.; Penland, K.; Hoatson, G. L.; Vold, R. L. Glassy Dynamics of Protein Methyl Groups Revealed by Deuteron Nmr. *J. Phys. Chem. B* **2013,** *117,* 1051-1061.
44. Xue, Y.; Pavlova, M. S.; Ryabov, Y. E.; Reif, B.; Skrynnikov, N. R. Methyl Rotation Barriers in Proteins from 2h Relaxation Data. Implications for Protein Structure. *J. Am. Chem. Soc.* **2007,** *129,* 6827-6838.
45. Latanowicz, L. Nmr Relaxation Study of Methyl Groups in Solids from Low to High Temperatures. *Concepts Magn. Reson., Part A* **2005,** *27A,* 38-53.
46. Andrew, E. R.; Hinshaw, W. S.; Hutchins, M. G. Proton Magnetic-Relaxation in Crystalline Amino Acids *J. Magn. Reson.* **1974,** *15,* 196-200.
47. Andrew, E. R.; Hinshaw, W. S.; Hutchins, M. G.; Sjoblom, R. O. I.; Canepa, P. C. Proton Magnetic-Relaxation and Molecular-Motion in Polycrystalline Amino Acids 2. Alanine, Isoleucine, Leucine, Methionine, Norleucine, Threonine and Valine *Mol. Phys.* **1976,** *32,* 795-806.
48. Daube, D.; Aladin, V.; Heiliger, J.; Wittmann, J. J.; Barthelmes, D.; Bengs, C.; Schwalbe, H.; Corzilius, B. Heteronuclear Cross-Relaxation under Solid-State Dynamic Nuclear Polarization. *J. Am. Chem. Soc.* **2016,** *138,* 16572–16575.
49. Colvin, M. T.; Silvers, R.; Ni, Q. Z.; Can, T. V.; Sergeyev, I.; Rosay, M.; Donovan, K. J.; Michael, B.; Wall, J.; Linse, S., et al. Atomic Resolution Structure of Monomorphic Aβ42 Amyloid Fibrils. *J. Am. Chem. Soc.* **2016,** *138,* 9663-9674.
50. Lehnert, E.; Mao, J. F.; Mehdipour, A. R.; Hummers, G.; Abele, R.; Glaubitz, C.; Tampe, R. Antigenic Peptide Recognition on the Human Abc Transporter Tap Resolved by Dnp-Enhanced Solid-State Nmr Spectroscopy. *J. Am. Chem. Soc.* **2016,** *138,* 13967-13974.
51. Kaushik, M.; Bahrenberg, T.; Can, T. V.; Caporini, M. A.; Silvers, R.; Heiliger, J.; Smith, A. A.; Schwalbe, H.; Griffin, R. G.; Corzilius, B. Gd(Iii) and Mn(Ii) Complexes for Dynamic Nuclear Polarization: Small Molecular Chelate Polarizing Agents and Applications with Site-Directed Spin Labeling of Proteins. *Phys. Chem. Chem. Phys.* **2016,** *18,* 27205-27218.
52. Fricke, P.; Mance, D.; Chevelkov, V.; Giller, K.; Becker, S.; Baldus, M.; Lange, A. High Resolution Observed in 800 Mhz Dnp Spectra of Extremely Rigid Type Iii Secretion Needles. *Journal of Biomolecular Nmr* **2016,** *65,* 121-126.
53. Gochnaue, M. B.; Kushner, D. J. Growth and Nutrition of Extremely Halophilic Bacteria. *Can. J. Microbiol.* **1969,** *15,* 1157-1160.
54. Batey, R. T.; Inada, M.; Kujawinski, E.; Puglisi, J. D.; Williamson, J. R. Preparation of Isotopically Labeled Ribonucleotides for Multidimensional Nmr-Spectroscopy of Rna. *Nucleic Acids Research* **1992,** *20,* 4515-4523.

55. Oesterhelt, D.; Stoeckenius, W. Isolation of the Cell Membrane of Halobacterium Halobium and Its Fractionation into Red and Purple Membrane. *Methods in enzymology* **1974,** *31,* 667-678.
56. Sauvee, C.; Rosay, M.; Casano, G.; Aussenac, F.; Weber, R. T.; Ouari, O.; Tordo, P. Highly Efficient, Water-Soluble Polarizing Agents for Dynamic Nuclear Polarization at High Frequency. *Angew. Chem. Int. Ed.* **2013,** *52,* 10858-10861.
57. Song, C.; Hu, K.-N.; Joo, C.-G.; Swager, T. M.; Griffin, R. G. Totapol: A Biradical Polarizing Agent for Dynamic Nuclear Polarization Experiments in Aqueous Media. *Journal of the American Chemical Society* **2006,** *128,* 11385-11390.
58. Guijarro, J. I.; Sunde, M.; Jones, J. A.; Campbell, I. D.; Dobson, C. M. Amyloid Fibril Formation by an Sh3 Domain. *Proc. Natl. Acad. Sci. U.S.A.* **1998,** *95,* 4224-4228.
59. Barnes, A. B.; Mak-Jurkauskas, M. L.; Matsuki, Y.; Bajaj, V. S.; Wel, P. C. A. v. d.; DeRocher, R.; Bryant, J.; Sirigiri, J. R.; Temkin, R. J.; Lugtenburg, J., et al. Cryogenic Sample Exchange Nmr Probe for Magic Angle Spinning Dynamic Nuclear Polarization. *J. Magn. Reson.* **2009,** *198,* 261–270.
60. Jawla, S.; Ni, Q. Z.; Barnes, A.; Guss, W.; Daviso, E.; Herzfeld, J.; Griffin, R.; Temkin, R. Continuously Tunable 250 Ghz Gyrotron with a Double Disk Window for Dnp-Nmr Spectroscopy. *J. Infrared Millim. Terahertz Waves* **2013,** *34,* 42-52.
61. Barnes, A. B.; Nanni, E. A.; Herzfeld, J.; Griffin, R. G.; Temkin, R. J. A 250 Ghz Gyrotron with a 3 Ghz Tuning Bandwidth for Dynamic Nuclear Polarization. *Journal of Magnetic Resonance* **2012,** *221,* 147-153.
62. Smith, S. A.; Levante, T. O.; Meier, B. H.; Ernst, R. R. Computer-Simulations in Magnetic-Resonance - an Object-Oriented Programming Approach. *J. Magn. Reson. Ser. A* **1994,** *106,* 75-105.
63. Cheng, V. B.; Suzukawa, H. H.; Wolfsberg, M. Investigations of a Nonrandom Numerical Method for Multimensional Integration *J. Chem. Phys.* **1973,** *59,* 3992-3999.
64. Eddy, M. T.; Belenky, M.; Sivertsen, A. C.; Griffin, R. G.; Herzfeld, J. Selectively Dispersed Isotope Labeling for Protein Structure Determination by Magic Angle Spinning Nmr. *Journal Of Biomolecular NMR* **2013,** *57,* 129-139.
65. Lee, A. L.; Wand, A. J. Microscopic Origins of Entropy, Heat Capacity and the Glass Transition in Proteins. *Nature* **2001,** *411,* 501-504.
66. Markin, A. V.; Markhasin, E.; Sologubov, S. S.; Ni, Q. Z.; Smirnova, N. N.; Griffin, R. G. Low-Temperature Polymorphic Phase Transition in a Crystalline Tripeptide L-Ala-L-Pro-Gly·H2o Revealed by Adiabatic Calorimetry. *J. Phys. Chem. B* **2015,** *119,* 1787-1792.
67. Bajaj, V. S.; van der Wel, P. C. A.; Griffin, R. G. Observation of a Low-Temperature, Dynamically Driven Structural Transition in a Polypeptide by Solid-State Nmr Spectroscopy. *Journal of the American Chemical Society* **2009,** *131,* 118-128.
68. Rice, D. M.; Wittebort, R. J.; Griffin, R. G.; Meirovitch, E.; Stimson, E. R.; Meinwald, Y. C.; Freed, J. H.; Scheraga, H. A. Rotational Jumps of the Tyrosine Sidechain in Crystalline Enkephalin H2 Nmr Lineshapes for Aromatic Rong Motion in Solids *Journal of the American Chemical Society* **1981,** *103,* 7707-7710.
69. Rice, D. M.; Meinwald, Y. C.; Scheraga, H. A.; Griffin, R. G. Tyrosyl Motion in Peptides H2 Nmr Lineshapes and Spin Lattice Relaxation *Journal of the American Chemical Society* **1987,** *109,* 1636-1640.
70. Kamihira, M.; Naito, A.; Tuzi, S.; Saito, H. Phenyl Ring Dynamics of Enkephalin Molecules and Behavior of Bound Solvents in the Crystalline States by H-2 Nmr Spectroscopy. *J. Phys. Chem. A* **1999,** *103,* 3356-3363.
71. Bayro, M. J.; Debelouchina, G. T.; Eddy, M. T.; Birkett, N. R.; MacPhee, C. E.; Rosay, M.; Maas, W. E.; Dobson, C. M.; Griffin, R. G. Intermolecular Structure Determination of Amyloid Fibrils with Magic-Angle Spinning and Dynamic Nuclear Polarization Nmr. *Journal of the American Chemical Society* **2011,** *133,* 13967-13974.

Chapter 4: Primary Proton Pathway of Bacteriorhodopsin Revealed by DNP Enhanced MAS NMR

Adapted from a manuscript in preparation by Q.Z. Ni, T.V. Can, E. Daviso, J. Herzfeld, and R.G. Griffin.

Bacteriorhodopsin (bR) is a transmembrane protein that functions as a light-drive ion pump. With its ready availability, bR has been thoroughly studied by many techniques. Nevertheless, one major question remains unanswered is bR's primary proton transfer pathway. Here we use dynamic nuclear polarization (DNP) MAS NMR to study bR's active site in the various intermediates of the photocycle. The active site is comprised of a retinylidene chromophore that interacts via its Schiff base (SB) with nearby water molecules and amino acid residues. An essential feature of the experiments is signal enhancement by a factor of 75 through the use of DNP. Bond length measurements of the SB proton reveal an elongated N-H bond in L, the transfer of ^{1}H in deprotonated M_0, and a tight N-H bond in N intermediate. The ^{1}H chemical shift of ~3.6 ppm in M_o indicates an alcohol hydrogen donor partner. This strongly supports the H^+ being relay from the SB to Asp85 via Thr89 as the pathway for bR's primary proton transfer.

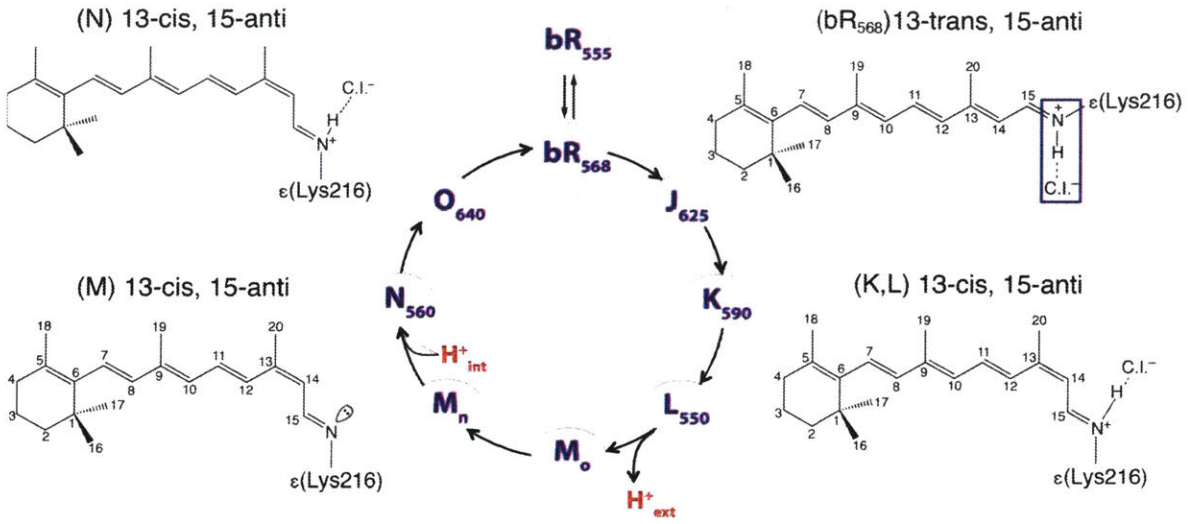

Figure 4.1 Photocycle of bR. The subscript next to each intermediate is the corresponding maximum absorption wavelength (nm). The orientations and configurations of the chromophore for each intermediate are displayed adjacent to the photocycle. The dark adapted (DA) state comprises a mixture of bR_{555} (13-trans, 15-syn) and bR_{568} (13-trans, 15-anti). Illumination converts bR_{555} to bR_{568}, resulting in the light adapted (LA) state. The boxed region of the bR_{568} structure highlights the hydrogen bond of the protonated SB for which water molecule wat402 is the acceptor. Wat402, Asp85, Asp212, Arg82 and other water molecules make up the complex counterion (CI), which has a (-1) charge density that stabilizes the positive charge on the nitrogen atom of the SB. The photocycle of bR_{568} pumps one ion per photon, with resolved intermediates K, L M_o, M_n, N, and O. The Schiff base deprotonates in $L \rightarrow M_0$, with concomitant protonation of D85 on the extracellular side of the chromophore, and reprotonates in $M_n \rightarrow N$, with concomitant deprotonation of D96 on the cytoplasmic side of the chromophore.

4.1 Introduction

Bacteriorhodopsin (bR), a 26kDa membrane protein found on the surfaces of archaeal cells, functions as a light-driven ion pump, generating electrochemical gradients that drive ATP synthesis. The seven transmembrane helices of bR enclose a retinylidene chromophore formed by a Schiff base (SB) between a retinal molecule and Lys216. Due to bR's relative availability, it serves as a model for other members of the rhodopsin family(1, 2) and for GPCRs more generally. Since its discovery in the 1970's, bR has been intensely studied by various methods including: X-ray crystallography,(4, 5) EM,(6, 7) IR,(8-11) molecular simulations(12, 13) and NMR.(14-21) Although advancements in these techniques have led to many insights over the years, the details of bR's pumping mechanism remain unclear.

The transduction of light energy involves a series of conformational and protonation changes with the resolved intermediates in a photocycle shown in **Figure 5.1** In the resting state, protonation of the SB is stabilized by a delocalized complex counterion (CI) comprising a hydrogen bonded complex of water molecules with Asp85, Asp212 and Arg82.(15, 22) In the absence of light, bR exists in dark adapted (DA) state, a mixture of bR_{555} (with a 13-*cis*, 15-*syn* chromophore) and bR_{568} (with an all-*trans*, 15-*trans* chromophore).(23) When irradiated with green light at 278 K, bR_{555} converts to the more stable bR_{568}, also known as the light adapted (LA) state.

bR_{568} is the active form of bR. Upon the absorption of light, the chromophore rapidly isomerizes from *all-trans*, 15-*trans* to 13-*cis*, 15-*trans*, with thermal reisomerization occurring only at the end of the photocycle.(24) The absorbed energy is stored in electrostatic form in the K intermediate and converted to torsion in the functional L intermediate.(25) The torsion leaves the SB connected to the extracellular side of the active site such that Asp85 becomes protonated when the SB becomes deprotonated in the transition from L to M_0. Due to this "switch", reprotonation of the SB is associated with deprotonation of Asp96 in the transition M_n to N. Lastly the SB thermal reisomerizes to bR_{568} in the O to bR_{568} transition. It is vital that both photoisomization and thermal reisomerization occur when the SB is protonated while the vectoriality of the pump requires connectivity change (the switch) occur between deprotonation and reprotonation of the SB. The cycle repeats itself with a 1:1 ratio between the photon absorbed and ion pumped.

bR_{568} is the active form of bR. Upon the absorption of light, the chromophore rapidly isomerizes from *all-trans*, 15-*trans* to 13-*cis*, 15-*trans*, with thermal reisomerization occurring only at the end of the photocycle. The absorbed energy is stored in electrostatic form in the K intermediate and converted to torsion in the functional L intermediate.(25) The torsion leaves the SB connected to the extracellular side of the active site such that Asp85 becomes protonated when the SB becomes deprotonated in the transition from L to M_0. Due to this "switch", reprotonation of the SB is associated with deprotonation of Asp96 in the transition M_n to N. Lastly the SB thermal reisomerizes to bR_{568} in the O to bR_{568} transition. It is vital that both photoisomization and thermal reisomerization occur when the SB is protonated while the vectoriality of the pump requires connectivity change (the switch) occur between deprotonation and reprotonation of the SB. The cycle repeats itself with a 1:1 ratio between the photon absorbed and ion pumped.

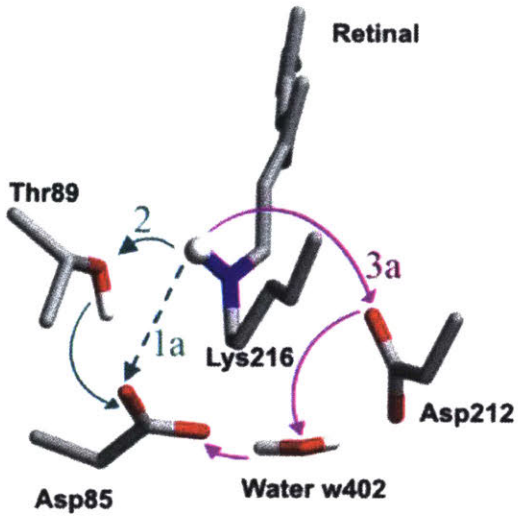

Figure 4.2 Three proposed pathways by Bondar *et al.* for primary proton transfer from SB nitrogen to Asp85, determined by computing minimum-energy reaction paths in Bacterirhodopsin using quantum/classical mechanics (QM/MM).(13) (1a). the proton is transferred directly from SB to Asp85 (2) the proton is relayed to Asp85 via Thr89. (3). The proton is transferred first to Asp212 and then to Asp85 along a proton wire via a water molecule.

Despite numerous breakthroughs over the years, a detailed mechanism of the primary proton transfer that takes place in the L→M_0 transition still remains elusive. The different orientations of the SB and members of the CI in multiple crystal structures were used by Bondar *et al.* for QM/MM calculations to determine the mechanism of primary proton transfer.(13) Calculations led to three possible pathways with the lowest energy barrier shown in **Figure 4.2**. These pathways involve highly divergent mechanisms, i.e. they require the SB to twist to varying degrees and different displacements of surrounding residues, and therefore, it is unlikely for all three pathways to coexist. Narrowing down the correct pathway involves seeking answers to additional questions: how does the proton of the SB behave throughout the photocycle? And although the deprotonation is seen to occur in M_0, does it occur instantaneously? Or does the SB prepare for deprotonation in intermediates prior to M_0? The SB NH covalent bond and the local environment of the SB ^{1}H in bR have never been closely investigated experimentally. Elucidating a membrane protein's function requires dynamic snapshots of structural changes at the atomic level. Here, we use MAS NMR in conjunction with dynamic nuclear polarization (DNP) to disclose bR's primary proton pathway. We present thorough look at the proton of the SB through the

bond length between the ^{1}H and ^{15}N of the SB and its ^{1}H chemical shift in various photocycle intermediates.

NMR is an exceptional tool in that it provides both chemical information (in common with other spectroscopies) and distance information (in common with diffraction and microscopy). In the case of MAS NMR, there is no requirement for either solubilization or crystallization, making it a powerful tool in structural biology.(26-30) The major shortcoming of NMR is in its low sensitivity, which becomes especially problematic when experiments are focused around a single nitrogen site of a large molecule, in this the SB of bR. The low sensitivity can be overcome with the addition of DNP, where the ~660-fold greater polarization of unpaired electrons is transferred to the protons and thence to the nuclei of interest.(31-33) A graphical display to illustrate the major components of our DNP/MAS NMR instrument is illustrated in **Figure 4.6**. DNP experiments are carried out at cryogenic temperatures, which coincidently also traps the various bR photocycle intermediates.(34-36) An enhancement of 75 was obtained on bR, corresponding to a savings of ~5,600-fold in acquisition time. This massive gain in sensitivity allows for multidimensional experiments to be done on the low gamma ^{15}N atom of the SB and its N-H···O complex.

Several groups have used MAS NMR to study biologically important N-H···N systems, including RNase, hCMV protease and M2.(37, 38) However, N-H···O investigations with MAS NMR have been limited to organic models at ambient temperatures.(39-42) Understanding N-H···O is particularly crucial in systems such as bR as it plays a central role in the active site. To obtain information on N-H···O via other techniques including X-ray crystallography or computational studies is either not possible or highly challenging, thus, the H bond length is fixed at 1.00 Å.(43) bR's hydrogen bond complex, $(SB)N^{+}$-H···$O(H_2)$, where N is the donor and O is the acceptor, is intimately associated with both the SB and nearby counterion residues. The role of proton donor and acceptor becomes reversed in M_0, where the ^{15}N shift of the deprotonated SB is 20 ppm upfield relative to that in retinylidene butylamine, suggesting that there is significant interaction with a hydrogen bond donor.(44)

It has been shown with MAS NMR that the Schiff base linkage in DA closely resembles those of more weakly hydrogen bonded protonated model compounds.(44) However, there hasn't been any other information on the SB proton in other intermediates. Our results show the SB NH covalent bond is unusually long in the L intermediate. Interestingly, there is a dipolar coupling between the two atoms in the deprotonated M_0 intermediate. The newly established NH bond is shorter than a typical amide NH bond in the N intermediate. In addition, the ^{1}H chemical shift values of the SB in various intermediates reveal that a weak

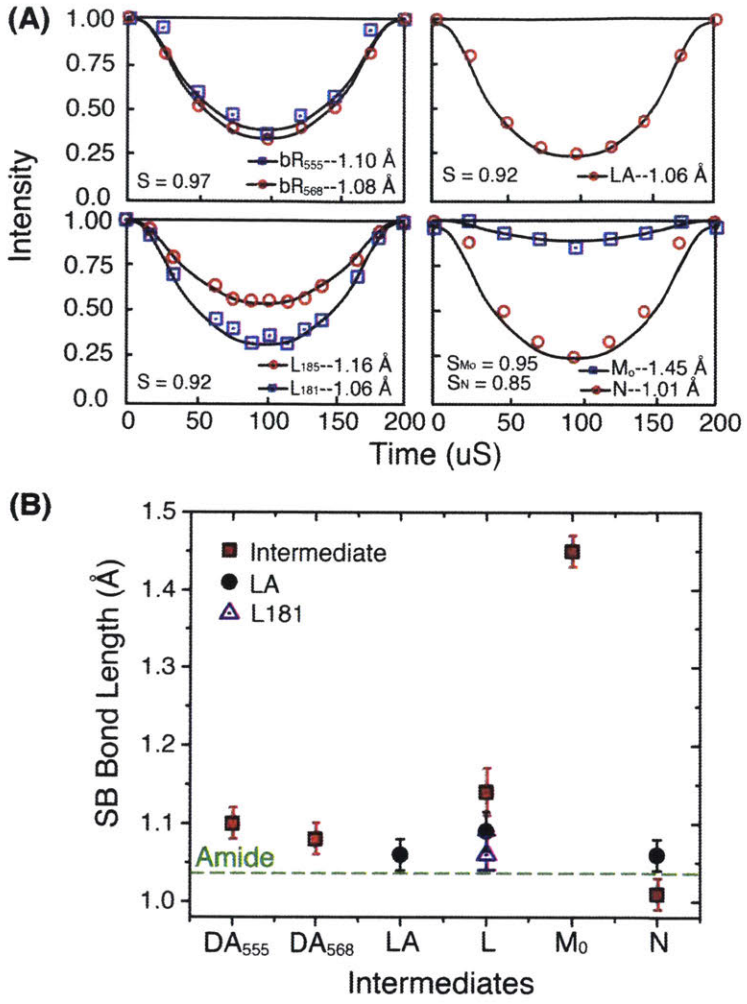

Figure 4.3 (A).^{15}N-^{1}H double-DIPSHIFT results at 90 K in the DA, LA, L, M_0 and N states. Each data point was collected with 16K scans and 7 seconds recycle delay. The scaling factor (S) is the ratio of the dipolar coupling constant of the amide backbone peak to the standard value of 10.8 kHz. Integrated SB peak intensities were deconvoluted using Origin and then fitted using SpinEvolution.(3) (B). Summary of the SB(N-H) bond length in various intermediates.

H-bond in the first half of the photocycle from LA to L. The upfield shift in ^{1}H chemical shift in M_0 highly supports an alcohol hydrogen bond donor group to the SB nitrogen which leads to the conclusion that the primary pathway of deprotonation from SB to Asp85 involves a proton atom being relayed through Thr89.

4.2 Schiff Base N-H Bond length

Figure 4.3 shows the results of the double dipolar chemical shift (DIPSHIFT) experiment employed to measure the dipolar coupling between the N and H nuclei of the SB. Since the influence of dynamics is assumed to be negligible at cryogenic temperatures, the

bond length is inferred directly from the measured dipolar coupling. In **Figure 4.3A**, the integrated SB peak intensities are plotted as a function of evolution time up to one rotor period. The scaling factor (S) is the ratio of the measured dipolar coupling constant of the amide backbone peak to the standard value of 10.8 kHz. S is then used to adjust the coupling constant obtained from the SB N-H bond in DA, LA, L, M_0 and N. Note that all the subscripts adjacent to the intermediates are the maximum visible absorption frequencies in *nm* of that particular intermediate except for the case of the L intermediate, where the subscripts are the ^{15}N chemical shifts values of the SB in ppm.

In the DA state, the bond length for bR_{568} is slightly shorter than for bR_{555} indicating somewhat weaker H-bond donation. The bond length obtained from **Figure 4.3A** are plotted together in chronological order of bR's photocycle, shown in **Figure 4.3B**. Each error bar in this figure was estimated from a pair of simulated DIPSHIFT curves corresponding to the upper and lower bounds of the measured distance. It can be seen that the bond length of bR_{568}/LA remains the same throughout all intermediates. The length of a standard amide bond of 1.04 Å is plotted across with a dotted line. The bond length in all intermediates except N, are longer than that of the amide bond. In L_{181}, the strength of the coupling constant is similar to that of LA. The N-H bond is elongated in L_{185} and unusually short in N, corresponding to strong H-bond donation in L_{185} and a weaker than in bR_{568} H-bond donation in N. The former suggests that the SB in L_{185} is ready to deprotonate and that, while the SB is reprotonated in N, it has not yet found a H-bond partner.

4.3 Local Environment of the Schiff Base ^1H

The SB H-bond is at the heart of the action in bR. From the NH correlation experiments in **Figure 4.4,** we obtain the ^1H chemical shifts summarized in **Table 4.5** for the DA, LA, K, L, M_0 and N intermediates. The experimental uncertainties listed for the ^{15}N, ^1H chemical shifts are determined by the peak's linewidth at half height. Laser irradiation at different temperatures yields different populations of the photocycle intermediates due to different barriers for forward and backward conversion. For example, when trapping the K intermediate, a portion of bR is always found in the bR_{568} state because there is a photo-equilibrium between the two at 90K. The ^1H chemical shift of the residual LA can be seen to have the same value in all intermediates, another indication that the spectra can be compared reliably with respect to each other.

Since the different forms are readily distinguished and assigned from ^{15}N spectra, the 2D spectra provide clear assignments of corresponding ^1H frequencies. Between the two

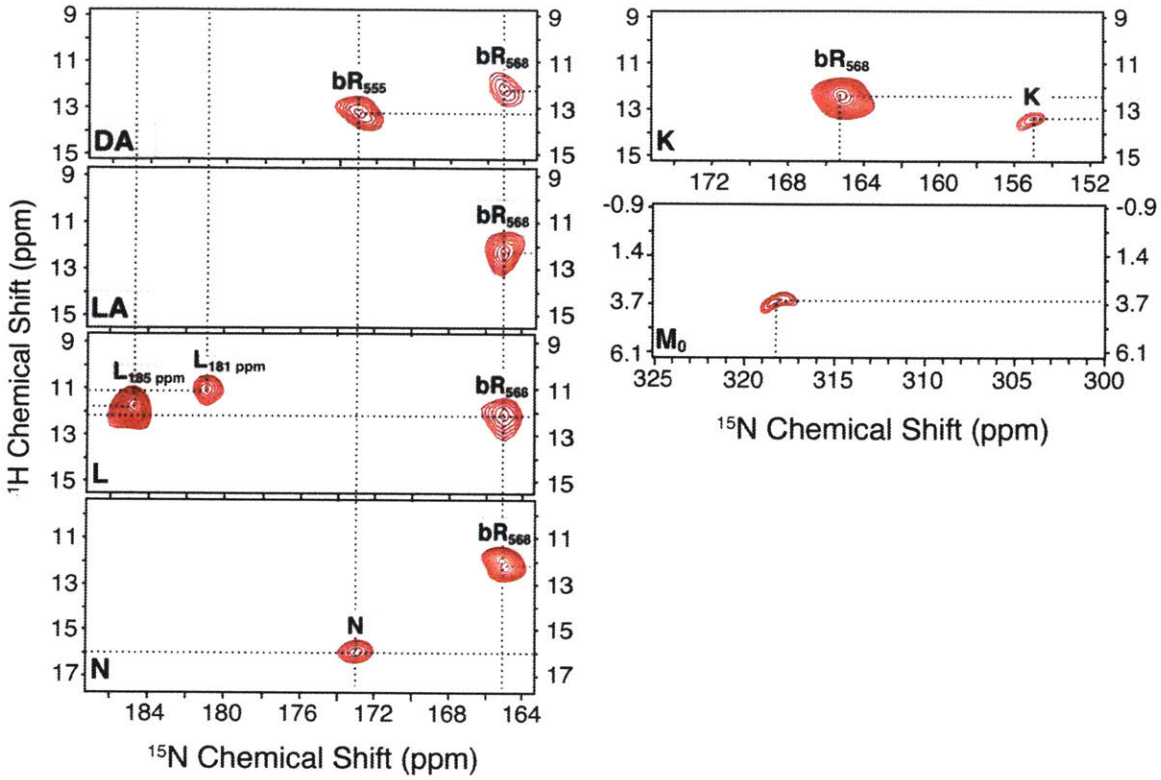

Figure 4.4. Two dimensional ^{15}N-^{1}H HETCOR spectra of DA, LA K, L, M_0, and N intermediates of [U-^{13}C, ^{15}N]bR. The ^{1}H and ^{15}N chemical shifts of the SB proton are listed in Table 1. The experimental scaling factor ranged from 0.453 to 0.547. Assignments of the different intermediates within a particular trapping procedure are labeled.

species present in the dark, bR_{568} has a lower ^{15}N and higher ^{1}H chemical shift than bR_{555}. The difference corresponds to a slightly stronger H-bond in bR_{555}, which is attributed to its 13-cis,15-syn configuration, vs. the 13-trans,15 anti configuration in bR_{568}. The weak hydrogen bond in bR_{568} is considered to be an important basis for the functionality of its photocycle.(21) As the SB loses its hydrogen bond partner in K, the ^{1}H chemical shift shifts slightly downfield to ~13.3 ppm.

In the L intermediate, where the SB reestablishes interactions with a CI, has been reported to have a total of four conformations, of which only L_{185} is functional. I.e., only L_{185} progresses to the M state rather than regresses to bR_{568}.(35) Under our trapping conditions, **Figure 4.4** only shows NH crosspeaks for L_{185}, L_{181} and LA. In both of the L states, the ^{1}H chemical shifts are slightly lower than that of LA state, due to the stronger counterion interactions in L. This suggests that the water hydrogen bonded to the SB becomes more polarized. N-H bond becomes more polar in nature as the hydrogen bond strengthens. The

highly polarized hydrogen bond suggests an inward-drive hydroxyl pump instead of an outward proton pump.(15, 45)

Table 4.5 ^{15}N, ^{1}H Chemical Shifts and bond length of the Schiff Base in bR

Intermediate	^{15}N (ppm)	^{1}H (ppm)	Bond Length (Å)
bR_{555}	173.5 ± 0.65	13.2 ± 0.4	1.10 ± 0.02
bR_{568} in DA	165.4 ± 0.60	12.2 ± 0.4	1.08 ± 0.03
bR_{568} in LA	165.4 ± 0.60	12.2 ± 0.5	1.06 ± 0.02
K	156.5 ± 0.72	13.3 ± 0.3	—
L165 (an unstable L)	165.4 ± 0.60	—	—
L174 (an unstable L)	174.3 ± 1.02	—	—
L181 (an unstable L)	181.2 ± 1.2	11.1 ± 0.3	1.06 ± 0.03
L185 (functional L)	184.9 ± 1.0	11.8 ± 0.4	1.16 ± 0.03
M_0 (early M)	318.4 ± 0.63	3.6 ± 0.3	1.45 ± 0.02
Mn (late M)	312.0 ± 0.65	—	—
N	173.3 ± 0.65	16.0 ± 0.3	1.01 ± 0.02

The ^{1}H chemical shift remains ~12 ppm in the first half of the photocycle, until M_0, where it shifts upfield to ~3.6ppm. Lastly, after reprotonation, the ^{1}H chemical shift of the SB in N intermediate is ~16ppm.

4.4 Primary proton pathway revealed

Differences in the ^{1}H chemical shifts result from different distributions of the electron density upon the (SB)N-H···O formation. In general, ^{1}H frequency moves downfield with formation with an acceptor, such as oxygen or nitrogen. Downfield shifts of the amide proton correlates to shorter H-bond length. As the H-bond strength increases, the proton atom experiences an increase (less deshielded, decrease in chemical shift) while the nitrogen atom experiences a decrease in charge density (more deshielded, increase in chemical shift). Summary of all the chemical shift values are listed in **Table 4.5**.

Earlier studies comparing the nitrogen chemical shifts of bR_{568} SB with halide salts of retinylidenebutyl [^{15}N] imine showed the isotropic shift of bR_{568} is 11 ppm further upfield than

any of the model compounds, suggesting an unusually weak hydrogen bond.(21) Our experimental results for bR_{568} agree with this finding. ^{1}H chemical shift is ~12 ppm, indicating that it is part of a weak H-bond. The ^{1}H chemical shift measured in **Figure 4.4** identifies the strength of the H-bond in that particular intermediate. The strength of the SB NH covalent bond in the first half of the photocycle is weaker than that of an amide backbone bond. Instead of a gradual weakening in bond strength, the NH bond remains weak from the very beginning of the photocycle. While the Cl is responsible for the overall electrostatic steering and for keeping the SB connected to the extracellular side of bR, they don't vary amongst the intermediates. The closest molecule of the Cl to the SB is a water molecule, Wat402.(13) Molecular simulation has shown that the water molecule that situates in between the SB and the aspartic residues has the role of maintaining a stable configuration of the protonated SB.(43) Regardless of the identity of the Cl, the polarization of the SB nitrogen relies more so on the overall strength/charge of the complex counterion. This explains why the ^{1}H chemical shift doesn't experience great variation from each other in the first half of the photocycle.

The lower ^{15}N frequency for K represents the less shielded nitrogen atom, corresponding to the slightly higher ^{1}H chemical shift value. In K, the SB loses contact with its Cl,(46) and the NH of the SB bond is claimed to rotate from diffraction and FTIR measurements.(47) The ^{1}H and ^{15}N chemical shift of both L_{185} and L_{181} are slightly lower and higher than that of LA, respectively.(21) The long NH bond in L intermediate could be the major cause to the 'opsin shift' observed, where bR's absorption maximum of its retinal protonated SB chromophore is shifted to the red.(48) The elongated NH bond length measured in L shows that L sets the stage for the primary deprotonation from the SB to Asp85 in the L to M_o transition.

The hydrogen bond interactions in L are lost in the M_o intermediate and ^{15}N chemical shift of the SB shifts downfield to 318 ppm, which is 12 ppm less than the standard retinylidene butylimine. This offset argues for the presence of a hydrogen bond donor water at the SB and that the roles of hydrogen bond donor and acceptor become reserved in M_o.(21) The SB proton was originally hydrogen bonded to wat402 loses its contact and rotates towards cytoplasmic side during the switch. The dipolar coupling measured for M_o in **Figure 4.3** confirms the presence of a hydrogen bond donor. Nango et al. reported that the hydrogen bond interaction from the protonated SB to wat452 or Thr89 creates a pathway in the initial proton transfer to Asp85.(49) The ^{1}H chemical shift of the SB in M_o strongly

indicates the donor is that of an alcohol. Our findings supports the idea that there has been a ^{1}H relay from the SB to Asp85 via Thr89 in the L to M_o transition.

After the switch from M_o to M_n, the ^{15}N chemical shift of the SB in N shows that it has an extraordinary weak counterion as a result of different charges and rearrangements of the elements of the CI. FTIR studies also indicated that the conformational change of the protein backbone is the largest in N.(50) The different environment attributes to the much higher ^{1}H chemical shift (~16 ppm) of the newly established SB NH bond. The distance measurement in N is consistent with λmax absorption values indicating a relaxed chromophore. (51)

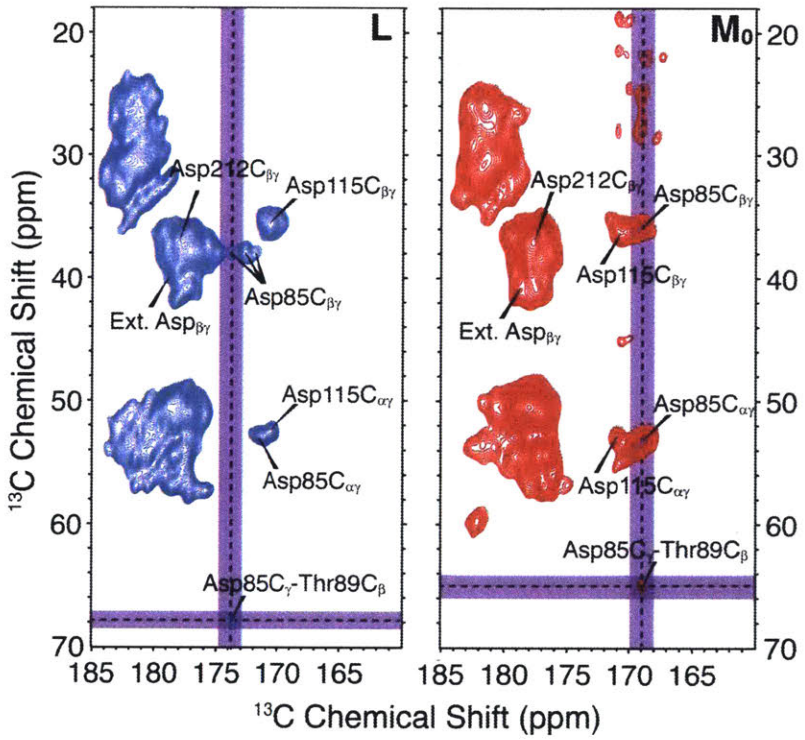

Figure 4.6 Long range ^{13}C-^{13}C chemical shift correlation RFDR spectra of [U-^{13}C, ^{15}N]bR doped with 5mM AMUPol displaying contact between Asp85-C_γ and Thr89-C_β in L (left) and in M_o intermediate (right). Three conformations of Asp85-$C_{\beta\gamma}$ are observed in L (174.4, 173.2, and 172.3)ppm, they correspond to the functional and nonfunctional forms of the L and LA intermediate. Only the Asp85-C_γ conformation at 174.4 ppm correlates to Thr89-C_β, representing the difficulty of obtaining functional L_{185}. In L to M_o, Asp85 reorganizes to develop a strong hydrogen bond with Thr89, which results the chemical shift of Thr89-C_β to shift upfield from 68.2 ppm to 64.75 ppm.

4.5 Thr89 – Asp 85 proximity

Fig. 4.6 shows ^{13}C-^{13}C correlations between the C_γ of aspartate residues with various upfield carbons. In these spectra, we see the characteristic upfield shift of the C_γ of Asp85 (from 169 ppm to 174 ppm) upon protonation in the L→M_o transition. In M_o, the C_γ of Asp85 is clearly correlated with the C_β of Thr89. As usual, the results are more complicated for L because multiple forms of the intermediate are typically trapped along with some LA. Interestingly, these variations are reflected in the $C_{\beta\gamma}$ cross-peak of Asp85 which shows that at least three species are present (as in the L panel of **Fig. 4**). However, only one of these species shows a correlation between the C_β of Thr89 and the C_γ of Asp85 analogous to that in M_o. Thus, it seems likely that this is the functional L, i.e., the precursor for M_o. Significantly, the change in the protonation states of the SB and Asp85 in going from L to M_o also affects the chemical shift of the C_β of Thr89. This is consistent with Thr89 being caught in a hydrogen bonded chain between the SB and Asp85.

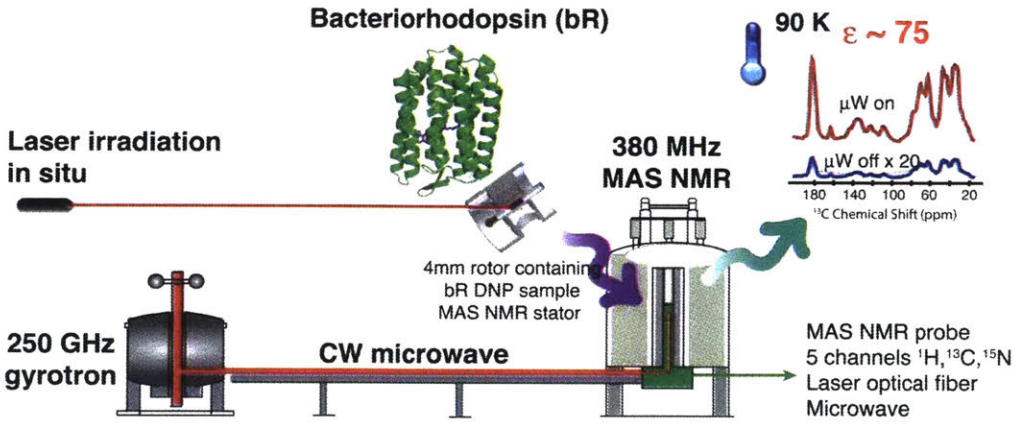

Figure 4.7. The components of the 250GHz/380MHz DNP MAS NMR instrumentation used for the experiments presented. In chronological order, bR DNP sample is packed in a 4mm sapphire rotor and placed in the stator housing of the triple resonance probe head. Visible light is delivered to the sample through in situ laser irradiation to initiate bR's photocycle. The sample is then cooled to cryogenic temperatures where the isolated intermediate is trapped. The low sensitivity of the NMR signal is enhanced by the addition of dynamic nuclear polarization (DNP) through constant wave microwave irradiation traveling from the gyrotron through the connecting wavelength to the MAS NMR probe.

4.6 Experimental

4.6.1 Sample preparation

Bacteriorhodopsin (bR), in its native purple membrane, was purified from *Halobacterium salinarum* grown in uniformly ^{13}C,^{15}N-labeled peptone medium.(52) The peptone was obtained from the anaerobic acid hydrolysis of *Methylophilus methylotrophus* cells grown on ^{13}C-labeled methanol and ^{15}N-labeled ammonium sulfate.(53) The purple membranes were isolated using the method of Oesterhelt and Stoechenius.(54) The sample was washed 3 times with 300 mM guanidine hydrochloride at pH 10.0. The sample was pelleted after each wash by centrifugation for 2 hours at ~43,000 g. The washed pellet was mixed with 5mM AMUPol polarizing agent(55) in d_8-glycerol/D_2O/H_2O (60/30/10 volume ratio) and centrifuged once more.

4.6.2 Trapping photocycle intermediates

Two types of light sources were used to generate bR photocycle intermediates: a diode-pumped solid state laser from Coherent operating at 532 nm (green) and 1W krypton laser from Cambridge Laser Laboratory emitting 647 nm (red). The photocycle intermediates were generated according to previous protocols:(56)

-LA was generated by irradiation of the dark-adapted bR sample with green light for 3 hours at 278 K.

-K was generated by irradiation of bR in LA state at 100 K with green light for 2 hours.

-L was generated by irradiation of bR in LA state at 150 K with red laser light for 3 hours.

-M_o was generated by irradiation of bR in LA state with green laser light at 210 K for 45 minutes.

-N was generated by irradiation of bR in LA state at 240 K with red laser light for 3 hours.

Each photocycle intermediate was kinetically trapped at 100 K, where spectra were acquired in the dark. During all stages, the bR sample was kept spinning by nitrogen gas through the bearing and drive lines of the magic angle spinning (MAS) probe.

4.5.3 DNP NMR Spectroscopy

All experiments were conducted with a DNP instrumentation consisting a gyrotron producing microwaves at 250 GHz(57, 58) and a 380 MHz/ 9T solid state NMR spectrometer equipped with a 4mm MAS triple channel (^1H, ^{13}C, ^{15}N) DNP probe at cryogenic temperatures.(59-61)

4.6.3.1 DIPSHIFT

NH bond lengths were measured using the dipolar-doubled 2D ^{15}N-^{1}H dipolar chemical shift (DIPSHIFT) correlation experiment(62) under 5kHz MAS. ^{1}H homonuclear decoupling of 100kHz was conducted with MREV8 sequence, which has a theoretical scaling factor of 0.477.(63) The experimental scaling factor at 90 K was measured using the amide backbone peak of bacteriorhodopsin and was found to be between 0.9-1 of the coupling constant for a typical NH bond of 1.04 Å.

4.6.3.2 HETCOR

Two-dimensional ^{15}N-^{1}H HETCOR spectra were measured under 5 kHz MAS. In the HETCOR pulse sequence, the homonuclear dipolar coupling to is averaged to zero under MREV8 homonuclear decoupling and the heteronuclear dipolar couplings are averaged by magic angle spinning during t1 evolution. Then cross polarization transfers the frequency encoded ^{1}H polarization to nitrogen for acquisition. For cross polarization, the contact time was 0.15 ms except for M_0 (0.9 ms), with a 50 kHz spin lock field on ^{1}H. ^{1}H homonuclear decoupling during the t1 evolution of 100 us and 32 increments was carried out using MREV8 sequence with 100 kHz decoupling.

^{1}H chemical shifts were obtained by multiplying the acquired values by the MREV8 experimental scaling factors, which were determined using the amide and arginine crosspeaks (not shown) as internal references set to 9.1 and 8.28 ppm, respectively. The experimental scaling factor ranged from 0.453 to 0.547. 100kHz of ^{1}H decoupling was used during acquisition to eliminate spin diffusion effects. In addition, to compensate the minor offsets between the theoretical and the experimental scaling factor.

4.7 ABBREVIATIONS

bR, bacteriorhodopsin; SB, Schiff base; DA, dark adapted; LA, light adapted; DNP, dynamic nuclear polarization; MAS NMR, magic angle spinning nuclear magnetic resonance; rf, radio frequency; CP, cross polarization; TPPM, two-pulse phase-modulated; RFDR, radio frequency driven recoupling; REDOR, fs; frequency

4.8 ACKNOWLEDGMENT

This work was supported by NIH grant #EB-002804, #EB-002026.

We thank Dr. Marina Belenky for preparing bR samples. We would like to thank Drs. Mei Hong, Ann Nicoletta Bondar, Robert Silvers for their valuable discussions. We thank Drs. Sudheer Jawla and Richard J. Temkin for their long lasting support on maintaining the

gyrotron instrumentation and Ajay Thakkar, Jeffrey Byrant, Mike Mullins for their lasting support.

4.9 References

1. Becker-Baldus J, *et al.* (2015) Enlightening the photoactive site of channelrhodopsin-2 by DNP-enhanced solid-state NMR spectroscopy. *Proceedings of the National Academy of Sciences* 112(32):9896-9901.
2. Maciejko J, *et al.* (2015) Visualizing Specific Cross-Protomer Interactions in the Homo-Oligomeric Membrane Protein Proteorhodopsin by Dynamic-Nuclear-Polarization-Enhanced Solid-State NMR. *J. Am. Chem. Soc.* 137(28):9032-9043.
3. Veshtort M & Griffin RG (2006) SPINEVOLUTION: A powerful tool for the simulation of solid and liquid state NMR experiments. *J. Magn. Reson.* 178(2):248-282.
4. Lanyi JK & Schobert B (2007) Structural Changes in the L Photointermediate of Bacteriorhodopsin. *J. Mol. Biol.* 365(5):1379-1392.
5. Grigorieff N, Ceska TA, Downing KH, Baldwin JM, & Henderson R (1996) Electron-crystallographic Refinement of the Structure of Bacteriorhodopsin. *J. Mol. Biol.* 259(3):393-421.
6. Bullough PA & Henderson R (1999) The projection structure of the low temperature K intermediate of the bacteriorhodopsin photocycle determined by electron diffraction1. *J. Mol. Biol.* 286(5):1663-1671.
7. Subramaniam S, *et al.* (1999) Protein conformational changes in the bacteriorhodopsin photocycle1. *J. Mol. Biol.* 287(1):145-161.
8. Rothschild KJ (2016) The early development and application of FTIR difference spectroscopy to membrane proteins: A personal perspective. *Biomedical Spectroscopy and Imaging* 5(3):231-267.
9. Sonar S, *et al.* (1995) Site-Directed Isotope Labeling and FTIR Spectroscopy - The Tyr-185/Pro-186 Peptide-Bond of Bacteriorhodopsin is Perturbed During the Primary Photoreaction. *J. Am. Chem. Soc.* 117(46):11614-11615.
10. Ludlam CFC, *et al.* (1995) Site-Directed Isotope Labeling and ATR-FTIR Difference Spectroscopy of Bacteriorhodopsin - The Peptide Carbonyl Group of Tyr-185 is Structurally Active During the Br- N-Transition. *Biochemistry* 34(1):2-6.
11. Morgan JE, Vakkasoglu AS, Lugtenburg J, Gennis RB, & Maeda A (2008) Structural Changes Due to the Deprotonation of the Proton Release Group in the M-Photointermediate of Bacteriorhodopsin as Revealed by Time-Resolved FTIR Spectroscopy. *Biochemistry* 47(44):11598-11605.
12. Bondar A-N, Fischer S, & Smith JC (2011) Water pathways in the bacteriorhodopsin proton pump. *The Journal Of Membrane Biology* 239(1-2):73-84.
13. Bondar AN, Elstner M, Suhai S, Smith JC, & Fischer S (2004) Mechanism of primary proton transfer in bacteriorhodopsin. *Structure* 12(7):1281-1288.
14. Jaroniec CP, Tounge BA, Herzfeld J, & Griffin RG (2001) Frequency selective heteronuclear dipolar recoupling in rotating solids: Accurate C-13-N-15 distance measurements in uniformly C-13,N-15-labeled peptides. *J. Am. Chem. Soc.* 123(15):3507-3519.
15. Herzfeld J & Lansing JC (2002) Magnetic resonance studies of the bacteriorhodopsin pump cycle. *Annu. Rev. Biophys. Biomol. Struct.* 31:73-95.
16. Petkova AT, *et al.* (2002) Tryptophan interactions in bacteriorhodopsin: A heteronuclear solid-state NMR study. *Biochemistry* 41(7):2429-2437.

17. Hu JG, *et al.* (1998) Early and late M intermediates in the bacteriorhodopsin photocycle: A solid-state NMR study. *Biochemistry* 37(22):8088-8096.
18. Hu JG, Griffin RG, & Herzfeld J (1994) Synergy in the Spectral Tuning of Retinal Pigments - Complete Accounting of the Opsin Shift in Bacteriorhodopsin. *Proc. Natl. Acad. Sci. U. S. A.* 91(19):8880-8884.
19. McDermott AE, *et al.* (1991) Mechanism of Proton Pumping in Bacteriorhodopsin by Solid-State NMR - The Protonation State of Tyrosine in the Light-Adapted and M-States. *Biochemistry* 30(34):8366-8371.
20. Smith SO, *et al.* (1989) Solid-State C-13 NMR of the Retinal Chromophore in Photointermediates of Bacteriorhodopsin - Characterization of 2 Forms of M. *Biochemistry* 28(1):237-243.
21. Degroot HJM, Harbison GS, Herzfeld J, & Griffin RG (1989) Nuclear Magnetic-Resonance Study of the Schiff-Base in Bacteriorhodopsin - Counterion Effects on the N-15 Shift Anisotropy. *Biochemistry* 28(8):3346-3353.
22. Bondar AN, Baudry J, Suhai S, Fischer S, & Smith JC (2008) Key Role of Active-Site Water Molecules in Bacteriorhodopsin Proton-Transfer Reactions. *Journal of Physical Chemistry B* 112(47):14729-14741.
23. Harbison GS, *et al.* (1984) Dark-Adapted Bacteriorhodopsin Contains 13-Cis,15-Syn and All-Trans,15-Anti Retinal Schiff-Bases. *Proceedings of the National Academy of Sciences of the United States of America-Biological Sciences* 81(6):1706-1709.
24. Fodor SPA, *et al.* (1988) Chromophore structure in bacteriorhodopsin's N intermediate: implications for the proton-pumping mechanism. *Biochemistry* 27(18):7097-7101.
25. Braiman M & Mathies R (1982) RESONANCE RAMAN-SPECTRA OF BACTERIORHODOPSINS PRIMARY PHOTOPRODUCT - EVIDENCE FOR A DISTORTED 13-CIS RETINAL CHROMOPHORE. *Proceedings of the National Academy of Sciences of the United States of America-Biological Sciences* 79(2):403-407.
26. Cady SD, *et al.* (2010) Structure of the Amantadine Binding Site of Influenza M2 Proton Channels in Lipid Bilayers. *Nature* 463(7281):689-U127.
27. Colvin MT, *et al.* (2016) Atomic Resolution Structure of Monomorphic Aβ42 Amyloid Fibrils. *J. Am. Chem. Soc.* 138(30):9663-9674.
28. Yan S, *et al.* (2015) Atomic-resolution structure of the CAP-Gly domain of dynactin on polymeric microtubules determined by magic angle spinning NMR spectroscopy. *Proceedings of the National Academy of Sciences of the United States of America* 112(47):14611-14616.
29. Tuttle MD, *et al.* (2016) Solid-state NMR structure of a pathogenic fibril of full-length human alpha-synuclein. *Nat. Struct. Mol. Biol.* 23(5):409-415.
30. Andreas LB, *et al.* (2015) Structure and Mechanism of the Influenza A M2(18-60) Dimer of Dimers. *J. Am. Chem. Soc.* 137(47):14877-14886.
31. Ni QZ, *et al.* (2013) High Frequency Dynamic Nuclear Polarization. *Acc. Chem. Res* 46(9):1933-1941.
32. Can TV, Ni QZ, & Griffin RG (2015) Mechanisms of dynamic nuclear polarization in insulating solids. *J. Magn. Reson.* 253:23-35.
33. Barnes AB, *et al.* (2008) High-Field Dynamic Nuclear Polarization for Solid and Solution Biological NMR. *Applied Magnetic Resonance* 34(3):237-263.
34. Bajaj VS, Mak-Jurkauskas ML, Belenky M, Herzfeld J, & Griffin RG (2009) Functional and shunt states of bacteriorhodopsin resolved by 250 GHz dynamic nuclear polarization-enhanced solid-state NMR. *Proceedings of the National Academy of Sciences* 106(23):9244-9249.

35. Mak-Jurkauskas ML, *et al.* (2008) Energy transformations early in the bacteriorhodopsin photocycle revealed by DNP-enhanced solid-state NMR. *Proc. Natl. Acad. Sci. U. S. A.* 105(3):883-888.
36. Bajaj VS, Mak-Jurkauskas ML, Belenky M, Herzfeld J, & Griffin RG (2010) DNP enhanced frequency-selective TEDOR experiments in bacteriorhodopsin. *J. Magn. Reson.* 202:9-13.
37. Song XJ & McDermott AE (2001) Proton transfer dynamics and N-H bond lengthening in N-H center dot center dot center dot N model systems: a solid-state NMR study. *Magnetic Resonance in Chemistry* 39:S37-S43.
38. White PB & Hong M (2015) 15N and 1H Solid-State NMR Investigation of a Canonical Low-Barrier Hydrogen-Bond Compound: 1,8-Bis(dimethylamino)naphthalene. *J. Phys. Chem. B* 119(35):11581-11589.
39. Sharif S, Denisov GS, Toney MD, & Limbach HH (2006) NMR studies of solvent-assisted proton transfer in a biologically relevant Schiff base: Toward a distinction of geometric and equilibrium H-bond isotope effects. *J. Am. Chem. Soc.* 128(10):3375-3387.
40. Sharif S, Denisov GS, Toney MD, & Limbach HH (2007) NMR studies of coupled low- and high-barrier hydrogen bonds in pyridoxal-5 '-phosphate model systems in polar solution. *J. Am. Chem. Soc.* 129(19):6313-6327.
41. Sharif S, *et al.* (2007) NMR Localization of Protons in Critical Enzyme Hydrogen Bonds. *J. Am. Chem. Soc.* 129(31):9558-9559.
42. Tolstoy PM, *et al.* (2010) Geometries and Tautomerism of OHN Hydrogen Bonds in Aprotic Solution Probed by H/D Isotope Effects on C-13 NMR Chemical Shifts. *Journal of Physical Chemistry A* 114(40):10775-10782.
43. Murata K, *et al.* (2000) A Study on the Mechanism of the Proton Transport in Bacteriorhodopsin: The Importance of the Water Molecule. *Biophys. J.* 79(2):982-991.
44. Harbison GS, Herzfeld J, & Griffin RG (1983) Solid-State N-15 Nuclear Magnetic-Resonance Study of the Schiff-Base in Bacteriorhodopsin. *Biochemistry* 22(1):1-5.
45. Herzfeld J & Tounge B (2000) NMR probes of vectoriality in the proton-motive photocycle of bacteriorhodopsin: evidence for an 'electrostatic steering' mechanism. *Biochimica Et Biophysica Acta-Bioenergetics* 1460(1):95-105.
46. Kandori H, Belenky M, & Herzfeld J (2002) Vibrational frequency and dipolar orientation of the protonated Schiff base in bacteriorhodopsin before and after photoisomerization. *Biochemistry* 41(19):6026-6031.
47. Schobert B, Cupp-Vickery J, Hornak V, Smith SO, & Lanyi JK (2002) Crystallographic Structure of the K Intermediate of Bacteriorhodopsin: Conservation of Free Energy after Photoisomerization of the Retinal. *J. Mol. Biol.* 321(4):715-726.
48. Lugtenburg J, *et al.* (1986) Mechanism for the Opsin Shift of Retinals Absorption in Bacteriorhodopsin. *J. Am. Chem. Soc.* 108(11):3104-3105.
49. Nango E, *et al.* (2016) A three-dimensional movie of structural changes in bacteriorhodopsin. *Science* 354(6319):1552-1557.
50. Bousché O, Sonar S, Krebs MP, Khorana HG, & Rothschild KJ (1992) Time-resolved fourier transform infrared spectroscopy of the bacteriorhodopsin mutant Tyr-185 →E: Asp-96 reportonates during O formation; Asp-85 and Asp-212 deprotonate during O decay *Photochem. Photobiol.* 56(6):1085-1095.
51. Hatcher ME, *et al.* (2002) Control of the pump cycle in bacteriorhodopsin: Mechanisms elucidated by solid-state NMR of the D85N mutant. *Biophys. J.* 82(2):1017-1029.
52. Gochnauer MB & Kushner DJ (1969) Growth and Nutrition of Extremely Halophilic Bacteria. *Canadian Journal of Microbiology* 15(10):1157-1160.

53. Batey RT, Inada M, Kujawinski E, Puglisi JD, & Williamson JR (1992) Preparation of Isotopically Labeled Ribonucleotides for Multidimensional NMR-Spectroscopy of RNA. *Nucleic Acids Res.* 20(17):4515-4523.
54. Oesterhelt D & Stoeckenius W (1974) Isolation of the Cell Membrane of Halobacterium Halobium and Its Fractionation into Red and Purple Membrane. *Methods Enzymol.* 31:667-678.
55. Sauvee C, *et al.* (2013) Highly Efficient, Water-Soluble Polarizing Agents for Dynamic Nuclear Polarization at High Frequency. *Angew. Chem. Int. Ed.* 52(41):10858-10861.
56. Balashov SP & Ebrey TG (2001) Trapping and Spectroscopic Identification of the Photointermediates of Bacteriorhodopsin at Low Temperatures. *Photochem. Photobiol.* 73(5):453-462.
57. Barnes AB, Nanni EA, Herzfeld J, Griffin RG, & Temkin RJ (2012) A 250 GHz gyrotron with a 3 GHz tuning bandwidth for dynamic nuclear polarization. *J. Magn. Reson.* 221:147-153.
58. Jawla S, *et al.* (2013) Continuously Tunable 250 GHz Gyrotron with a Double Disk Window for DNP-NMR Spectroscopy. *Journal of Infrared Millimeter and Terahertz Waves* 34(1):42-52.
59. Barnes AB, *et al.* (2009) Cryogenic sample exchange NMR probe for magic angle spinning dynamic nuclear polarization. *J. Magn. Reson.* 198:261–270.
60. Barnes AB, *et al.* (2010) Resolution and polarization distribution in cryogenic DNP/MAS experiments. *Physical Chemistry Chemical Physics* 12(22):5861-5867.
61. Ni QZ, *et al.* (2017) Peptide and Protein Dynamics and Low-Temperature/DNP Magic Angle Spinning NMR. *J. Phys. Chem. B* 121(19):4997-5006.
62. Munowitz MG, Griffin RG, Bodenhausen G, & Huang TH (1981) TWO-DIMENSIONAL ROTATIONAL SPIN-ECHO NUCLEAR MAGNETIC-RESONANCE IN SOLIDS - CORRELATION OF CHEMICAL-SHIFT AND DIPOLAR INTERACTIONS. *J. Am. Chem. Soc.* 103(10):2529-2533.
63. Rhim WK, Elleman DD, & Vaughan RW (1973) Analysis of multiple pulse NMR in solids. *Journal of Chemical Physics* 59(7):3740-3749.

Chapter 5: Insights into the Ion-motive Photocycle of Bacteriorhodopsin Using DNP-enhanced Solid-state NMR to Probe the Active Site

Adapted from a manuscript in preparation by Q.Z. Ni, E. Daviso, T.V. Can, J. Herzfeld, and R.G. Griffin.

The 26 kDa light-driven ion pump, bacteriorhodospin (bR) is comprised of 7 trans-membrane helices that enclose a retinylidene chromophore formed by a Schiff base (SB) between the retinal and K216. Despite numerous studies by different techniques, details of the bR pump mechanism remain elusive due to experimental limitations in sensitivity and/or resolution. Here, dynamic nuclear polarization (DNP) is employed to boost the ^{1}H NMR signal by transferring polarization from electrons of polarizing agents. DNP NMR experiments are done at cryogenic temperatures, which also trap the various bR photocycle intermediates (DA, LA, K, L, M_o, and N), allowing them to be studied in situ. With an enhancement of 75, we are able to follow elements of the active site via multidimensional spectra. Distance measurements obtained from 3D fs-REDOR presented here are the first set of long-range DNP MAS NMR distance measurements conducted on a uniformly labeled bR system. We find that the SB-D85 distance shrinks in the first half of the photocycle and is released after the primary proton transfer that neutralizes the opposing charges on the two parties. The decrease in distance between the two indicates helix C and helix G are moving toward each other, which could be the reason why functional L is difficult to achieve. The subsequent release of helix G provides an additional gate to the release of the torsion energy in the chromophore. Meanwhile, the SB-D212 distance hardly changes.

5.1 Introduction

Ion pumps are ubiquitous in nature. To understand how they function requires a thorough investigation of the details of their pumping mechanisms. bR is a 26 kDa light-driven proton exporter (or hydroxide importer) found in the purple patches of the cell membrane of *Halobacterium salinarium*. Similar to other members of the rhodopsin family, bR contains a retinylidene chromophore linked to K216 through a Schiff base (SB). Since its discovery in the 1970's, bR has been heavily studied by various methods including X-ray crystallography,(1, 2) electron microscopy,(3, 4) IR spectroscopy,(5-8) molecular simulations(9, 10) and NMR.(11-18) Although advances in these techniques have led to many highly complementary breakthroughs; details of bR's pumping mechanism remain unclear.

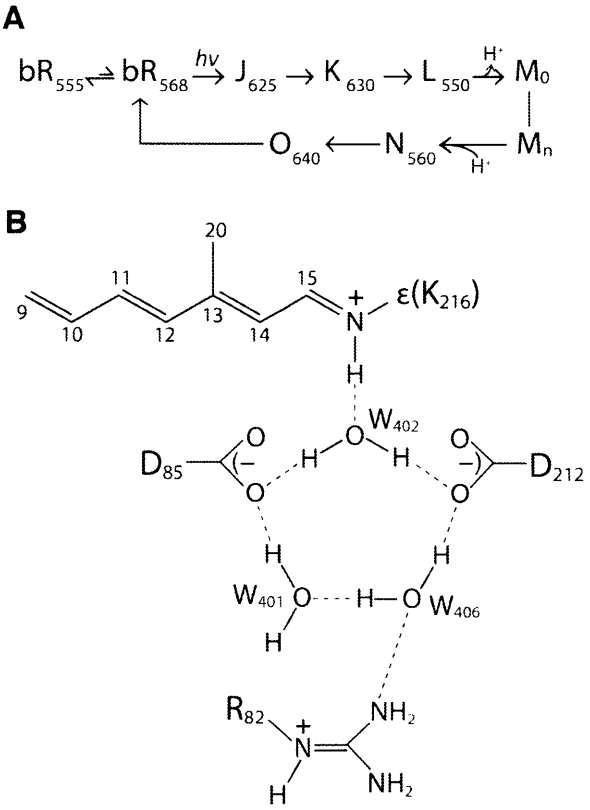

Figure 5.1 (A) Photocycle of bR. Dark adapted (DA) state consists of both bR_{555} (13-*cis*, 15-*syn*) and bR_{568} (13-*trans*, 15-*anti*). Upon the absorption of light, bR_{555} converts to bR_{568}, known as the light adapted (L.A). The retinal then adapts (13-*cis*, 15-*anti)* configuration in the remaining intermediates K, L M_0, M_n, and N, and O before relaxing back to all trans configuration. The number next to the intermediates represents the λ_{max} values of that particular intermediate. The Schiff base deprotonates in L→ M_0, and reprotonates in M_n→N. Each intermediate can be isolated by laser irradiation and trapped at cryogenic temperatures for DNP NMR experiments. (B) Structure of the active site in the LA state showing the SB and its complex counterion charge delocalization. Hydrogen bonded complex counterion contains two acidic residues, D85 and D212, and one basic residue R82.

At rest without illumination, bR exists in the dark-adapted (DA) state, which comprises a mixture of bR_{555} (with a 13-*cis*, 15-*syn* chromophore) and bR_{568} (with a 13-*trans*, 15-*anti* chromophore). When irradiated with green light at 5°C, bR_{555} converts to the more stable bR_{568}, also known as the light adapted (LA) state. From here, the ion-motive photocycle is initiated with optically distinct intermediates (see **Fig. 5.1A**), where the subscripts indicate the corresponding λ_{max} absorption values. Light absorption causes the chromophore of bR_{568} to rapidly isomerize to the 13-*cis*, 15-*anti* configuration. The absorbed energy is stored in electrostatic form in the K intermediate and is converted to torsional energy in the L intermediate.(19)A decrease in the pKa of the SB causes it to deprotonate in the L$\rightarrow$ M_0 transition, while D85 becomes protonated.(20) Once the SB deprotonates, it undergoes "the switch", $M_0 \rightarrow$Mn, where it is freed from the electrostatically enforced torsion and changes its connectivity from the extracellular side of the protein to the intracellular side. In Mn$\rightarrow$N transition, the reprotonation of the SB is associated with the deprotonation of D96.

The strong degree of shielding in ^{15}N chemical shift values of the SB which is correlated to the degree of charge delocalization on the SB counterion,(21) suggest that SB counterion is extraordinarily delocalized. Such delocalization of the SB counterion can be explained by the presence of a hydrogen-bonded complex counterion consisting of polar residues and water.(**Fig. 5.1B)** Diffraction results subsequently showed that the complex counterion (CI) comprises D85, D212, R82 and a water molecules.(22) Hydrogen bonds among these residues delocalize the overall (-1) charge, thereby stabilizing protonation of the SB. Close examination of relationships among these groups during the proton transfer steps of the photocycle will assist in elucidating further details of the vectorial action of the pump.

The aspartic acids in bR have been heavily studied since the 1980's. There are nine aspartic acids in bR, four of which are in the hydrophobic core of the protein, D85, D96, D115 and D212.(23, 24) In particular, D212 and D85 are located near the active site. Studies used site directed mutagenesis(25) and phototrophically negative mutants(26) by Glu and/or Asn to distinguish the aspartic acids from each other for assignments. Infrared experiments first demonstrated that the carboxylate groups in aspartate are protonated and deprotonated during the photocycle. (27, 28) In addition, D96 and D115 are found to be protonated while and D85 and D212 are deprotonated in the ground state.(29, 30) D85 is located near the SB and D96 is located ~12 Å from the SB towards the cytoplasmic side of the protein. Both residues undergo protonation changes during the bR photocycle. Chemical shift values of the D-C_γ and their protonation states in the native state were

previously reported using [4-^{13}C]Asp-labeled bR. (31) Since then, due to experimental limitations, a thorough empirical analysis of the internal aspartic acids through the photocycle has yet to be done. Further revelations require techniques that can provide both sufficient sensitivity and resolution at the atomic scale.

NMR is a particularly versatile tool because it provides both chemical information through chemical shielding values and structural information through dipole interaction measurements. In the past, solid state NMR has proven to be one of the most unambiguous methods for characterizing details of the chromophore in bR.(32-34) The major difficulty with NMR lies in its low sensitivity, making it challenging to acquire multidimensional data for quantitative measurements. Experiments become particularly challenging when the target of interest revolves around a single low gyromagnetic ratio nitrogen atom. The low sensitivity can be addressed via the use of dynamic nuclear polarization (DNP). Typically for biological systems, DNP transfers the polarization from electrons in the polarizing agent to the protons in a system and thence to the nuclei of interest.(35, 36) DNP NMR experiments are done at cryogenic temperatures,(37) which coincidently also traps the various bR photocycle intermediates, allowing the stages of transport to be studied in situ.(19, 38) An enhancement of 75 was obtained for bR, corresponding to a savings of ~5600-fold in acquisition time. With this boost in sensitivity, we are able to conduct three-dimensional NMR spectroscopy to monitor the active site residues and measure their distances to the SB in various photocycle intermediates.

The solid-state NMR techniques employed here are intended to study bR's photocycle in three sections: 1) ^{15}N chemical shifts of the SB. 2) ^{13}C chemical shifts of the internal aspartic acids and their protonation states. In particular, the $C_{\beta\gamma}$ signals of the four internal aspartic acids are identified in each intermediate. 3) distance measurements between the SB nitrogen atom and C_g's of the two aspartic acids at the active site using 3D frequency selective (fs)-REDOR experiment. From the distance measurements, the decreasing distance between D85-SB provides insights into the helical movements throughout the photocycle, which is critical for the vectorality of the ion motive pump.

5.2 Experimental

5.2.1 Sample preparation

Bacteriorhodopsin (bR), in its native purple membrane, was purified from *Halobacterium salinarum* grown in uniformly ^{13}C,^{15}N-labeled peptone medium.(39) The peptone was obtained from the anaerobic acid hydrolysis of *Methylophilus methylotrophus* cells grown on

^{13}C-labeled methanol and ^{15}N-labeled ammonium sulfate.(40) The purple membranes were isolated using the method of Oesterhelt and Stoechenius.(41) The sample was washed 3 times with 300 mM guanidine hydrochloride at pH 10.0. The sample was pelleted after each wash by centrifugation for 2 hours at ~43,000 g. The washed pellet was mixed with 5mM AMUPol polarizing agent(42) in d_8-glycerol/D_2O/H_2O (60/30/10 volume ratio) and centrifuged once more.

5.2.2 Trapping photocycle intermediates

Two types of light sources were used to generate bR photocycle intermediates: a diode-pumped solid state laser from Coherent operating at 532 nm (green) and 1W krypton laser from Cambridge Laser Laboratory emitting 647 nm (red). The photocycle intermediates were generated according to previous protocols:(43)

-LA was generated by irradiation of the dark-adapted, bR sample with green light for 3 hours at 278 K.

-K was generated by irradiation of bR in LA state at 100 K with green light for 2 hours.

-L was generated by irradiation of bR in LA state at 150 K with red laser light for 3 hours.

-M_0 was generated by irradiation of bR in LA state with green laser light at 210 K for 45 minutes.

-N was generated by irradiation of bR in LA state at 240 K with red laser light for 3 hours.

Each photocycle intermediate was kinetically trapped at 100 K, where spectra were acquired in the dark. During all stages, the bR sample was kept spinning by nitrogen gas through the bearing and drive lines of the magic angle spinning (MAS) probe.

5.2.3 DNP NMR Spectroscopy

DNP enhanced MAS NMR spectra were recorded on a custom built 380 MHz/9T solid state NMR spectrometer equipped with a 4mm MAS $e^-/^1H/^{13}C/^{15}N$ probe,(44) and a 250 GHz gyrotron.(45, 46) During DNP experiments, the temperature was kept at around 100 K. Referencing was done to DSS ^{13}C signals of adamantine at room temperature and reconfirmed with the ^{15}N chemical shift of the SB at 100 K. All experiments used 100 kHz of proton TPPM(47) decoupling during acquisition. ^{15}N **cross polarization** (CP) experiments were recorded using ramp CP from ^{1}H to ^{15}N with a contact time of 0.5 ms. Each 1D spectrum was acquired with 7 s recycle delay and 1024 scans.

5.2.3.1 CP-RFDR-REDOR

The RFDR(48) part of the experiment is initiated by cross polarization, followed by a chemical shift evolution period, t_1. A pair of π/2 pulses encompassing the longitudinal mixing period τ_{mix} prepares the spin polarizations for exchange and returns them to the transverse plane.(49) Rotor synchronized π pulses were applied during the mixing period to induce exchange via homonuclear dipole-dipole couplings. The π pulses were alternated according to the XY-16 phase cycling scheme to compensate for resonance offsets and pulse imperfections. The subsequent REDOR part of the experiment uses a ^{13}C-^{15}N filter to eliminate N C_γ and Q C_δ signals in t_2. RFDR and REDOR filter lengths were 1.184 ms and 1.48 ms, respectively. CW/TPPM stands for CW during the pulsing on other channel and TPPM during the gaps. Two-dimensional ^{13}C-^{13}C spectra were acquired with (120, 896) complex points with dwell times (32, 20) μs. Each FID was obtained with 16 scans of 7 seconds recycle delay.

5.2.3.2 CP-RFDR-REDOR-fs-REDOR

Measurements of the distance between the D-C_γ and the Schiff base N were performed using the CP-RFDR- REDOR-frequency selective (fs)-REDOR(50) sequence at $\omega_r/2\pi$ = 6.757 kHz and recycle delay 6.8s. Parameters used for the RFDR and REDOR filter are similar to the CP-RFDR-REDOR section mentioned above and the durations were 1.184 and 1.48 ms, respectively. RF was 50 kHz on the carbon channel during the RFDR, and 30 kHz on the nitrogen channel during the REDOR filter and mixing periods. During fs-REDOR, the (t_2) Gaussian 180° selective pulse lengths were 0.35 ms and 2.5 ms for D-C_γ and K-216 $^{15}N_\zeta$ of SB, respectively. S and So signals were recorded with and without the ^{15}N selective pulse, in alternatingly fashion at every increment of the indirect dimension. Experimental data were obtained with 128 and 384 transients for t_2 < 15ms and t_2 > 15ms, respectively. Signals of the D85 and D212 were then integrated in Sparky using the same processing parameters for both S and So. Values of S/So were then plotted vs. the fs-REDOR mixing time (t_2), from 0 to 25 ms. Experimental S/So fs-REDOR dephasing curves are plotted for LA, L, M_0 and N intermediates. Experimental data were fitted with Bessel function,(51) using scaling factor 0.9 to compensate for experimental imperfections.

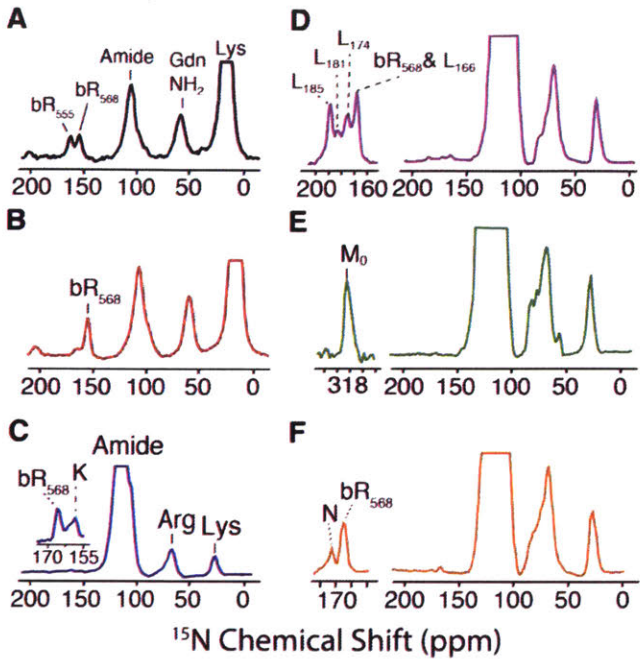

Figure 5.2 ^{15}N spectra of photocycle intermediates of bR: (A) dark adapted, (B) light adapated, (C) K, (D) functional and nonfunction L, (E) M_0, and (F) N. In (A-B), [ζ-^{15}N]lysine-bR was used with 20mM TOTAPOL, resulting in an enhancemnt of 45. In (C-F), U[^{13}C, ^{15}N]-bR was used with 5mM AMUPol, resulting in an enhancement of 75. Expansions of the SB region are shown for intermediates: K, L, M_0 and N.

5.3 Results

5.3.1 Views from the Schiff base

In the dark adapted state (DA), bR_{555} and bR_{568} exist in the expected 60:40 ratio.**(Fig. 5.2A)** Upon laser irradiation at 5°C, most of the bR_{555} is converted to bR_{568} **(Fig. 5.2B)**, the LA resting state for the ion-motive photocycle. After photoisomerization to the K intermediate, the ^{15}N SB peak appears at 155 ppm.**(Fig. 5.2C)** There are four substates of L: L_{165}, L_{174}, L_{181}, and L_{185}.**(Fig. 5.2D)**(19) Deprotonation in M_0 causes the ^{15}N chemical shift of the SB to be drastically shifted downfield to 318ppm (**Fig. 5.2E**). Continuing forward in the photocycle to N, where the reprotonation of the SB causes its ^{15}N chemical shift to shift upfield to 173.3 ppm,(**Fig. 5.2F)** similar to those intermediates prior to M_0.

5.3.2 Role of the Aspartic acids

The aspartic acids play a crucial role in the proton pumping mechanism, and therefore, we examine each aspartic acid in greater detail. **Fig. 5.3** shows the aspartic acid region of a

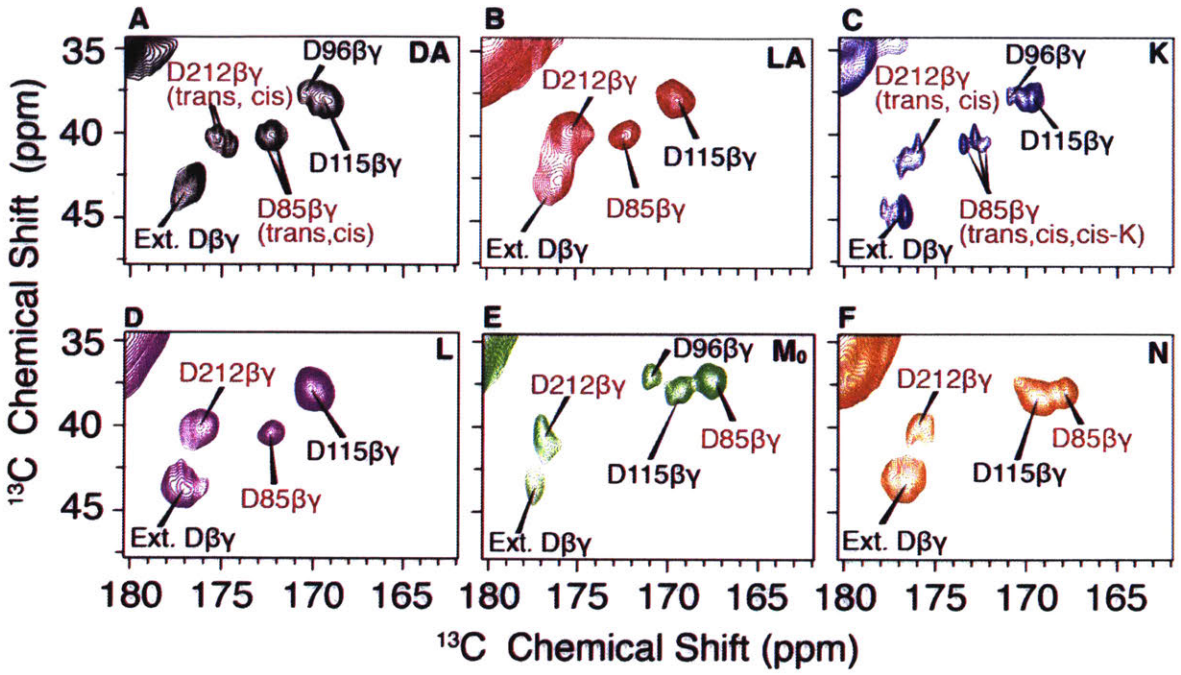

Figure 5.3 Two dimensional ^{13}C-^{13}C chemical shift correlation RFDR spectra of [U-^{13}C, ^{15}N]bR doped with 5mM AMUPol displaying side chain methylene to carboxyl $C_{\beta\gamma}$ cross peaks of D residues. The crosspeaks for the buried aspartate residues (D85 and D212 in the active site (red), and D96 and D115 elsewhere) can be followed through different states: (B) DA, (B) LA, (C) K, (D) L, (E) M_o, and (F) N. To eliminate amide signals, the 2D RFDR sequence was followed by a REDOR one bond ^{13}C-^{15}N dipolar filter (see Methods).

2D homonuclear RFDR ^{13}C-^{13}C chemical shift correlation spectrum of bR displaying the aspartic side chain methylene to carboxyl (C_{bg}) crosspeaks in various intermediates. In **Fig. 5.3A and 5.3B**, the chemical shift values of the aspartic acids of bR in DA and LA are in agreement with previously published values.(23, 31) The D212 chemical shift increases from 175 ppm in LA to 176.9 ppm in M_o. D85 stays at 172.4 ppm from LA to L and then deprotonates to 167.4 ppm in M_o. D115 remains at 169.2 ppm from DA to N, with slight variations in chemical shift values in K and L. D96 was detected in DA, K, M_o and N, the chemical shift value remains at 170.6 ppm.

Distances between D85, D212 and SB were measured by using the pulse sequence is shown in **Fig. 5.4**. This experiment allows for distance measurements in a large spin system where multiple internuclear distances can be determined. The pulse sequence is broken down into three sections, beginning with the coherence transfer to C_γ and C_β in RFDR, a subsequent REDOR filter that eliminates one-bond signals from nuclei directly bonded to a ^{15}N nucleus (such as Asn C_γ and Gln C_δ), and a frequency selective REDOR, where the

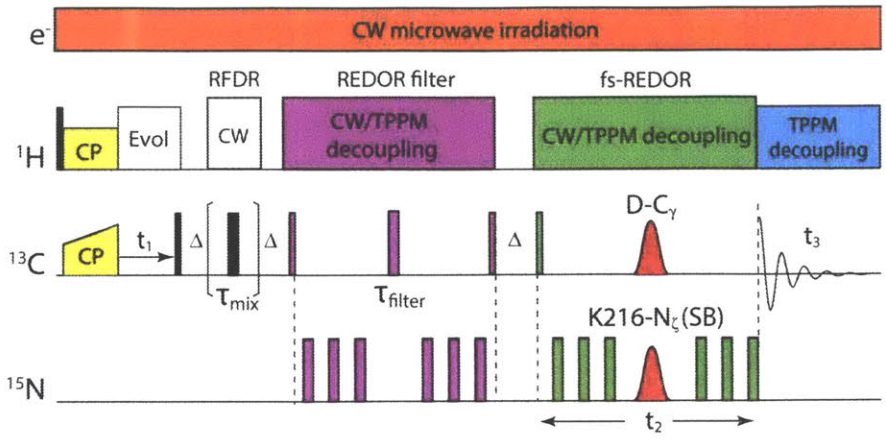

Fig. 5.4. Three dimensional DNP experiment for the measurement of dipolar couplings between the Schiff base nitrogen atom and D85 C_γ in [U-^{13}C,^{15}N]bR. Spectra were recorded at 9 T, 380 MHz, ω_r = 6.757 kHz. Narrow and wide rectangles stand for π /2 and π pulses respectively. Starting with cross polarization from ^{1}H to ^{13}C with contact time of 0.7ms, followed by t_1 evolution on carbon. The remainder of the pulse sequence contains three parts: RFDR, REDOR filter and frequency selective REDOR. Both RFDR and REDOR filter times were 1.184 ms. REDOR and FSR ^{15}N p pulses length were 16.6 ms for 30 kHz rf irradiation. During fs-REDOR, selective Gaussian pulses of 0.35ms and 2.5ms were applied on the D-C_γ and the SB respectively. Gaussian selective pulses were divided into 64 steps. The z-filters were 50ms. Proton decoupling was 100 kHz was used for both mixing and acquisition period.

frequency selective spin echo refocuses the multiple homonuclear and heteronuclear spin-spin interactions.(11) D85-SB distance in LA, L, M_0, and N are measured to be 4.7 Å, 4.3 Å, 4.2 Å and 4.6 Å, respectively while the D212-SB distance remained around 4.5 Å in LA, L and M_o.

5.4 DISCUSSION

The ^{15}N signal of the SB in **Fig. 5.2** is an excellent probe of the active site. It is also a reliable method to verify the presence of a particular isolated intermediate. Upon the absorption of light, the retinal photoisomerizes to the K intermediate, where the chemical shift of the SB is 10 ppm upfield from where it was in LA. This upfield shift has been attributed to a loss of contact of the SB with its CI, which is partially re-established in L by torsion of the chromophore. Of the four substates of L, only L_{185} progresses to M_o while the others convert to LA upon thermal relaxation. **(Fig. 5.2D)**(19) The deprotonation of the SB in M_o causes ^{15}N chemical shift to drastically shift downfield to 318 ppm; however, this is not nearly as far downfield as that of retinylidene butylimine, strongly suggesting the presence of a hydrogen bond donor nearby. Lastly, the SB reclaims its role as a hydrogen bond donor when it reprotonates in the N intermediate.

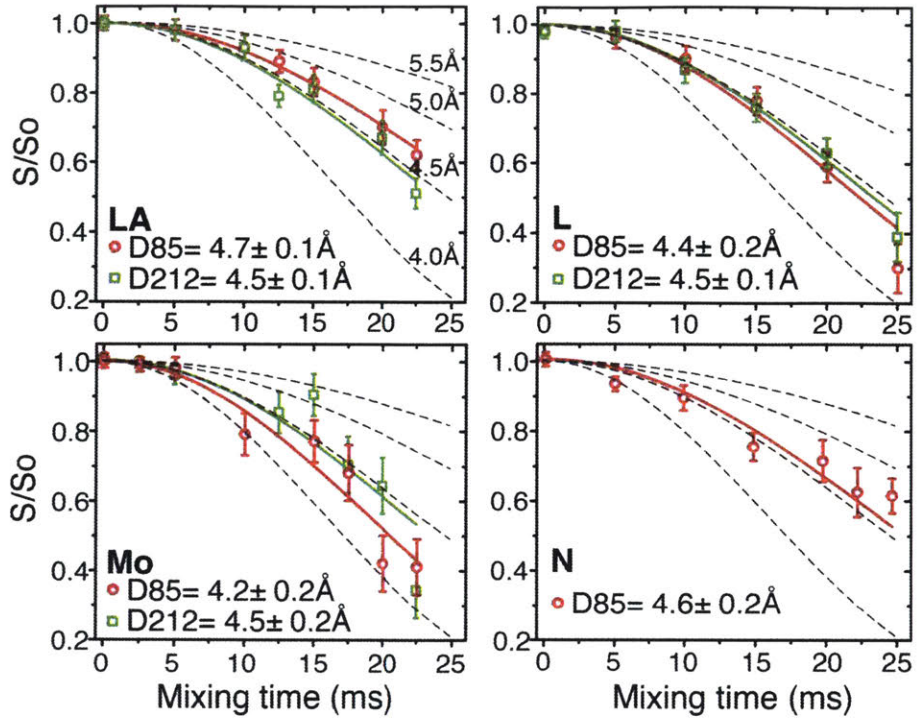

Fig. 5.5. Dephasing curves of the distances measured from C_γ in D85(red) and D212 (green) to the SB nitrogen in LA, L M_o, and N [U-^{13}C,^{15}N]bR. Simulated curves are plotted for distances 4.0 to 5.5 A in increments of 0.5 A. (black dotted line) S and reference So curves were acquired with and without the Gaussian pulse on ^{15}N of the experiment in Fig 5, with varying t2 mixing times from 0 to 25ms. (see Methods).

On the basis of the 2D RFDR spectra, we are able to follow the C_γ and C_β chemical shift values of the internal aspartic acids as well as their protonation states through the photocycle. In DA, D85 and D212 each have two signals due to the presence of 13-cis, 15-syn and all-trans chromophores. We notice several differences between the DA and LA. First, the ratio between bR_{555} and bR_{568} is discerned in DA, whereas LA is populated mostly with bR_{568}. For both residues the C_g of D212 appears a bit further downfield in LA, indicating that the residue experiences a more hydrophilic environment.

In K, **Fig. 5.3C,** an additional peak is detected for D85 in the 13-cis, 15 anti configuration. Since isomerization reduces the interaction of the SB with its complex counterion, perturbation of the residues comprising the complex is expected. Surprisingly, heterogeneity in the cross peaks does not appear to be present in the L intermediate (**Fig. 5.3D**). Apparently the renewed interaction of the SB with its counterion in functional L is not distinguishable because after releasing some of the strain in K, the configuration of the

retinal results in a downfield shift in the SB nitrogen, and therefore, yields similar chemical environment to the SB in LA.

In M_o, **Fig. 5.3E,** D85 becomes protonated and therefore its C_g is shifted substantially upfield, from 172.9 ppm to 168.7 ppm, in agreement with previous findings.(31) The low and broad intensity of the D212 crosspeak suggests that the residue is in a more flexible environment in M_o intermediate.

In agreement with FTIR results, D85 remains protonated in N intermediate, **(Fig. 5.3F)** suggesting that the deprotonation of D85 doesn't occur until after the N intermediate, either during the O intermediate or the decay of O to LA.(52) Time-resolved visible absorption studies and photoelectric measurements have shown that D96 donates a proton to the SB during the M→N transition and it reprotonates during N decay.(53) Our results imply that D96 is in a more flexible environment and isn't detected in N. The minor variations in the chemical shifts confirm that D212 remains deprotonated and D115 protonated throughout the photocycle.

5.4.1 3D Distance Measurements between D85, D212 and SB

Distance measurements provide crucial insights into the active site of bR. In the past, X-ray crystallography and EM have offered numerous bR structures, however these techniques have modest resolution and cannot distinguish among structures in mixtures.(1-3, 54) The resolution of $C_{\beta\gamma}$ signals for D85 and D212 in **Fig. 5.3**, provides the basis for distance measurements. With the signal enhancement provided by DNP, we employ a 3D fs-REDOR experiment **(Fig. 5.4)** to measure the distances between C_γ atoms of aspartic acids and the ^{15}N atom of the SB in different intermediates. The results are presented in **Fig. 5.5**.

In LA, the D85-SB distance is shorter than the D212 distance, supporting the claim that D85 is more strongly hydrogen bonded to the interior water 402 than D212.(22) D85 in LA has the longest distance, consistent with the well-known stabilization of the resting state of the SB by delocalization of the balancing negative charge across a hydrogen-bonded complex of multiple residues and water molecules.

A gradual decrease in the SB-D85 distance is observed from LA to M_o. A local bend of helix C toward the center of the hydrophobic core is unique in L.(55) The helix C movement inward is crucial as it sets the stage for the primary ^1H transfer to occur between the SB and D85. Previous NMR studies also reported observations of D85 approaching the SB in L.(56, 57) The need for inward helical movement could also explain why only the functional L_{181} proceeds forward while the other nonfunctional L's fail. However, since the pump is known

to be highly efficient, there may not be as many failed L's at room temperature than at ~150 K, at which the L intermediate was isolated.

The relatively short distance in M_o agrees with the fact that the active site has not yet had a chance to relax after the deprotonation of the SB and protonation of D85. Oka and coworkers used a mercury mutant at residue 222 of bR to observe the structural changes in helix G between DA and M_n. The mutated residue 222 on helix G is seen to move by 2.1 Å towards the directly opposing helix C in M_n.(58) The longer distance found in N indicates that the once contracted SB-D85 distance is now released. The release of the interhelical attraction breaks/gates the interactions found in previous intermediates. Meanwhile, the SB-D212 distance remains at ~4.5 Å in intermediates LA, L and M_o. The constant distance is not surprising because the SB and D212 are one turn apart on the Helix G.

5.5 CONCLUSION

DNP-enhanced NMR spectroscopy has provided unique insights into bR's proton transport pump. We are able to obtain snapshots of key elements in bR's pumping mechanism, which include the SB and residues D85, D96 and D212. Quantitative distance measurements between the SB and D85 indicates that the two helices C and G, which largely compose the active site are being drawn closer together from LA $\rightarrow$ L $\rightarrow$ M_o. The increase in SB-D85 distance from $M_o \rightarrow$ N supports the release of the interhelical attraction after neutralization of charges on both sides. These factors along with the untwisting of the retinylidene in $M_o \rightarrow M_n$, contributes to the vectoriality of bR's ion motive pump.

5.6 ABBREVIATIONS

bR, bacteriorhodopsin; SB, Schiff base; DA, dark adapted; LA, light adapted; DNP, dynamic nuclear polarization; MAS NMR, magic angle spinning nuclear magnetic resonance; rf, radio frequency; CP, cross polarization; TPPM, two-pulse phase-modulated; RFDR, radio frequency driven recoupling; REDOR, fs; frequency

5.7 ACKNOWLEDGMENT

Funding Sources

This work was supported by NIH grant #EB-002804, #EB-002026.

We would like to thank Drs. Ann Nicoletta Bondar, Jinggui Hu and Robert Silvers for their valuable discussions. We thank Sudheer Jawla and Richard J. Temkin for their long lasting support on gyrotron and Jeffrey Byrant and Ajay Thakkar for assistance with instrumentation.

5.8 References

1. Lanyi JK & Schobert B (2007) Structural Changes in the L Photointermediate of Bacteriorhodopsin. *J. Mol. Biol.* 365(5):1379-1392.
2. Grigorieff N, Ceska TA, Downing KH, Baldwin JM, & Henderson R (1996) Electron-crystallographic Refinement of the Structure of Bacteriorhodopsin. *J. Mol. Biol.* 259(3):393-421.
3. Bullough PA & Henderson R (1999) The projection structure of the low temperature K intermediate of the bacteriorhodopsin photocycle determined by electron diffraction1. *J. Mol. Biol.* 286(5):1663-1671.
4. Subramaniam S, *et al.* (1999) Protein conformational changes in the bacteriorhodopsin photocycle1. *J. Mol. Biol.* 287(1):145-161.
5. Rothschild KJ (2016) The early development and application of FTIR difference spectroscopy to membrane proteins: A personal perspective. *Biomedical Spectroscopy and Imaging* 5(3):231-267.
6. Sonar S, *et al.* (1995) Site-Directed Isotope Labeling and FTIR Spectroscopy - The Tyr-185/Pro-186 Peptide-Bond of Bacteriorhodopsin is Perturbed During the Primary Photoreaction. *J. Am. Chem. Soc.* 117(46):11614-11615.
7. Ludlam CFC, *et al.* (1995) Site-Directed Isotope Labeling and ATR-FTIR Difference Spectroscopy of Bacteriorhodopsin - The Peptide Carbonyl Group of Tyr-185 is Structurally Active During the Br- N-Transition. *Biochemistry* 34(1):2-6.
8. Morgan JE, Vakkasoglu AS, Lugtenburg J, Gennis RB, & Maeda A (2008) Structural Changes Due to the Deprotonation of the Proton Release Group in the M-Photointermediate of Bacteriorhodopsin as Revealed by Time-Resolved FTIR Spectroscopy. *Biochemistry* 47(44):11598-11605.
9. Bondar A-N, Fischer S, & Smith JC (2011) Water pathways in the bacteriorhodopsin proton pump. *The Journal Of Membrane Biology* 239(1-2):73-84.
10. Bondar AN, Elstner M, Suhai S, Smith JC, & Fischer S (2004) Mechanism of primary proton transfer in bacteriorhodopsin. *Structure* 12(7):1281-1288.
11. Jaroniec CP, Tounge BA, Herzfeld J, & Griffin RG (2001) Frequency selective heteronuclear dipolar recoupling in rotating solids: Accurate C-13-N-15 distance measurements in uniformly C-13,N-15-labeled peptides. *J. Am. Chem. Soc.* 123(15):3507-3519.
12. Herzfeld J & Lansing JC (2002) Magnetic resonance studies of the bacteriorhodopsin pump cycle. *Annu. Rev. Biophys. Biomol. Struct.* 31:73-95.
13. Petkova AT, *et al.* (2002) Tryptophan interactions in bacteriorhodopsin: A heteronuclear solid-state NMR study. *Biochemistry* 41(7):2429-2437.
14. Hu JG, *et al.* (1998) Early and late M intermediates in the bacteriorhodopsin photocycle: A solid-state NMR study. *Biochemistry* 37(22):8088-8096.
15. Hu JG, Griffin RG, & Herzfeld J (1994) Synergy in the Spectral Tuning of Retinal Pigments - Complete Accounting of the Opsin Shift in Bacteriorhodopsin. *Proc. Natl. Acad. Sci. U. S. A.* 91(19):8880-8884.
16. McDermott AE, *et al.* (1991) Mechanism of Proton Pumping in Bacteriorhodopsin by Solid-State NMR - The Protonation State of Tyrosine in the Light-Adapted and M-States. *Biochemistry* 30(34):8366-8371.
17. Smith SO, *et al.* (1989) Solid-State C-13 NMR of the Retinal Chromophore in Photointermediates of Bacteriorhodopsin - Characterization of 2 Forms of M. *Biochemistry* 28(1):237-243.
18. Degroot HJM, Harbison GS, Herzfeld J, & Griffin RG (1989) Nuclear Magnetic-Resonance Study of the Schiff-Base in Bacteriorhodopsin - Counterion Effects on the N-15 Shift Anisotropy. *Biochemistry* 28(8):3346-3353.

19. Mak-Jurkauskas ML, *et al.* (2008) Energy transformations early in the bacteriorhodopsin photocycle revealed by DNP-enhanced solid-state NMR. *Proc. Natl. Acad. Sci. U. S. A.* 105(3):883-888.
20. Metz Gn, Siebert F, & Engelhard M (1992) Asp85 is the only internal aspartic acid that gets protonated in the M intermediate and the purple-to-blue transition of bacteriorhodopsin A solid-state13C CP-MAS NMR investigation. *FEBS Lett.* 303(2):237-241.
21. Degroot HJM, *et al.* (1990) Solid-State C-13 and N-15 NMR-Study of the Low pH Forms of Bacteriorhodopsin. *Biochemistry* 29(29):6873-6883.
22. Luecke H, Schobert B, Richter H-T, Cartailler J-P, & Lanyi JK (1999) Structure of bacteriorhodopsin at 1.55 Å resolution *J. Mol. Biol.* 291(4):899-911.
23. Engelhard M, *et al.* (1990) High resolution 13C-solid state NMR of bacteriorhodopsin: assignment of specific aspartic acids and structural implications of single site mutations. *Eur. Biophys. J.* 18(1):17-24.
24. Eisenstein L, *et al.* (1987) FTIR difference studies on apoproteins. Protonation states of aspartic and glutamic acid residues during the photocycle of bacteriorhodopsin. *J. Am. Chem. Soc.* 109(22):6860-6862.
25. Mogi T, Stern LJ, Marti T, Chao BH, & Khorana HG (1988) Structure-function studies on bacteriorhodopsin. IX. Substitutions of tryptophan residues affect protein-retinal interactions in bacteriorhodopsin. *Proc. Natl. Acad. Sci. U. S. A.* 85(12):4148-4152.
26. Soppa J & Oesterhelt D (1989) Bacteriorhodopsin mutants of Halobacterium sp. GRB. I. The 5-bromo-2'-deoxyuridine selection as a method to isolate point mutants in halobacteria. *J. Biol. Chem.* 264(22):13043-13048.
27. Rothschild KJ, Zagaeski M, & Cantore WA (1981) Conformational changes of bacteriorhodopsin detected by Fourier transform infrared difference spectroscopy. *Biochem. Biophys. Res. Commun.* 103(2):483-489.
28. Siebert F, Mantele W, & Kreutz W (1982) Evidence for the protonation of two internal carboxylic groups during the photocycle of bacteriorhodopsin: Investigation of kinetic infrared spectroscopy. *FEBS Lett.* 141(1):82-87.
29. Braiman MS, *et al.* (1988) Vibrational spectroscopy of bacteriorhodopsin mutants: light-driven proton transport involves protonation changes of aspartic acid residues 85, 96, and 212. *Biochemistry* 27(23):8516-8520.
30. Gerwert K, Hess B, Soppa J, & Oesterhelt D (1989) Role of aspartate-96 in proton translocation by bacteriorhodopsin. *Proc. Natl. Acad. Sci. U. S. A.* 86(13):4943-4947.
31. Metz G, Siebert F, & Engelhard M (1992) High-resolution solid state carbon-13 NMR of bacteriorhodopsin: characterization of [4-13C]Asp resonances. *Biochemistry* 31(2):455-462.
32. Farrar MR, *et al.* (1993) Solid-State NMR-Study of Epsilon-C-13 Lys-Bacteriorhodospin - Schiff-Base Photoisomerization. *Biophys. J.* 65(1):310-315.
33. Harbison GS, Herzfeld J, & Griffin RG (1983) Solid-State N-15 Nuclear Magnetic-Resonance Study of the Schiff-Base in Bacteriorhodopsin. *Biochemistry* 22(1):1-5.
34. Lakshmi KV, *et al.* (1993) Internuclear Distance Measurement in a Reaction Intermediate - Solid-State C-13 NMR Rotational Resonance Determination of the Schiff-Base Configuration in the M-Photointermediate of Bacteriorhodopsin. *J. Am. Chem. Soc.* 115(18):8515-8516.
35. Ni QZ, *et al.* (2013) High Frequency Dynamic Nuclear Polarization. *Acc. Chem. Res* 46(9):1933-1941.
36. Can TV, Ni QZ, & Griffin RG (2015) Mechanisms of dynamic nuclear polarization in insulating solids. *J. Magn. Reson.* 253:23-35.
37. Ni QZ, *et al.* (2017) Peptide and Protein Dynamics and Low-Temperature/DNP Magic Angle Spinning NMR. *J. Phys. Chem. B* 121(19):4997-5006.

38. Bajaj VS, Mak-Jurkauskas ML, Belenky M, Herzfeld J, & Griffin RG (2010) DNP enhanced frequency-selective TEDOR experiments in bacteriorhodopsin. *J. Magn. Reson.* 202:9-13.
39. Gochnaue MB & Kushner DJ (1969) Growth and Nutrition of Extremely Halophilic Bacteria. *Canadian Journal of Microbiology* 15(10):1157-1160.
40. Batey RT, Inada M, Kujawinski E, Puglisi JD, & Williamson JR (1992) Preparation of Isotopically Labeled Ribonucleotides for Multidimensional NMR-Spectroscopy of RNA. *Nucleic Acids Res.* 20(17):4515-4523.
41. Oesterhelt D & Stoeckenius W (1974) Isolation of the Cell Membrane of Halobacterium Halobium and Its Fractionation into Red and Purple Membrane. *Methods Enzymol.* 31:667-678.
42. Sauvee C, *et al.* (2013) Highly Efficient, Water-Soluble Polarizing Agents for Dynamic Nuclear Polarization at High Frequency. *Angew. Chem. Int. Ed.* 52(41):10858-10861.
43. Balashov SP & Ebrey TG (2001) Trapping and Spectroscopic Identification of the Photointermediates of Bacteriorhodopsin at Low Temperatures. *Photochem. Photobiol.* 73(5):453-462.
44. Barnes AB, *et al.* (2009) Cryogenic sample exchange NMR probe for magic angle spinning dynamic nuclear polarization. *J. Magn. Reson.* 198:261–270.
45. Barnes AB, Nanni EA, Herzfeld J, Griffin RG, & Temkin RJ (2012) A 250 GHz gyrotron with a 3 GHz tuning bandwidth for dynamic nuclear polarization. *J. Magn. Reson.* 221:147-153.
46. Jawla S, *et al.* (2013) Continuously Tunable 250 GHz Gyrotron with a Double Disk Window for DNP-NMR Spectroscopy. *Journal of Infrared Millimeter and Terahertz Waves* 34(1):42-52.
47. Bennett AE, Rienstra CM, Auger M, Lakshmi KV, & Griffin RG (1995) Heteronuclear decoupling in rotating solids. *Journal of Chemical Physics* 103(16):6951-6958.
48. Bennett AE, *et al.* (1998) Homonuclear radio frequency-driven recoupling in rotating solids. *J. Chem. Phys.* 108(22):9463-9479.
49. Griffiths JM, *et al.* (1994) Dipolar Correlation NMR-Spectroscopy of a Membrane-Protein. *J. Am. Chem. Soc.* 116(22):10178-10181.
50. Jaroniec CP, *et al.* (2001) Measurement of dipolar couplings in a uniformly C-13,N-15- labeled membrane protein: Distances between the Schiff base and aspartic acids in the active site of bacteriorhodopsin. *J. Am. Chem. Soc.* 123(51):12929-12930.
51. Jaroniec CP, Filip C, & Griffin RG (2002) 3D TEDOR NMR Experiments for the Simultaneous Measurement of Multiple Carbon−Nitrogen Distances in Uniformly 13C,15N-Labeled Solids. *J. Am. Chem. Soc.* 124(36):10728-10742.
52. Bousché O, Sonar S, Krebs MP, Khorana HG, & Rothschild KJ (1992) Time-resolved fourier transform infrared spectroscopy of the bacteriorhodopsin mutant Tyr-185 →E: Asp-96 reportonates during O formation; Asp-85 and Asp-212 deprotonate during O decay *Photochem. Photobiol.* 56(6):1085-1095.
53. Holz M, *et al.* (1989) Replacement of aspartic acid 96 by asparagine in bacteriorhodopsin slows both the decay of the M intermediate and the associated proton movement *Proc. Natl. Acad. Sci. U. S. A.* 86(7):2167-2171.
54. Schobert B, Cupp-Vickery J, Hornak V, Smith SO, & Lanyi JK (2002) Crystallographic Structure of the K Intermediate of Bacteriorhodopsin: Conservation of Free Energy after Photoisomerization of the Retinal. *J. Mol. Biol.* 321(4):715-726.
55. Edman K, *et al.* (2004) Deformation of helix C in the low temperature L-intermediate of bacteriorhodopsin. *J. Biol. Chem.* 279(3):2147-2158.

56. Hu JGG, Sun BQQ, Petkova AT, Griffin RG, & Herzfeld J (1997) The predischarge chromophore in bacteriorhodopsin: A N-15 solid-state NMR study of the L photointermediate. *Biochemistry* 36(31):9316-9322.
57. Herzfeld J & Tounge B (2000) NMR probes of vectoriality in the proton-motive photocycle of bacteriorhodopsin: evidence for an 'electrostatic steering' mechanism. *Biochimica Et Biophysica Acta-Bioenergetics* 1460(1):95-105.
58. Oka T, *et al.* (1999) Conformational Change of Helix G in the Bacteriorhodopsin Photocycle: Investigation with Heavy Atom Labeling and X-Ray Diffraction. *Biophys. J.* 76(2):1018-1023.

Chapter 6: In-Situ Characterization of Pharmaceutical Formulations by Dynamic Nuclear Polarization Enhanced MAS NMR

Adapted from Q.Z. Ni, F.Y. Yang, T.V. Can, I. Sergeyev, S. M. D'Addio, S. K. Jawla, Y. Li, M. P. Lipert, W. Xu, R. Williamson, A. Leone, R. G. Griffin, Y.C. Su, Journal of Physical Chemistry B 121 (2017) 8132

A principal advantage of magic angle spinning (MAS) NMR spectroscopy lies in its ability to determine molecular structure in a non-invasive and quantitative manner. Accordingly, MAS should be widely applicable to studies of the structure of active pharmaceutical ingredients (API) and formulations. However, the low sensitivity encountered in spectroscopy of natural abundance APIs present at low concentration has limited the success of MAS experiments. Dynamic nuclear polarization (DNP) enhances NMR sensitivity and can be used to circumvent this problem agent able paramagnetic polarizing can be incorporated into the system without altering the integrity of solid dosages. Here, we demonstrate that DNP polarizing agents can be added *in*-situ during the preparation of amorphous solid dispersions (ASDs) via spray drying and hot-melt extrusion so that ASDs can be examined during drug development. Specifically, the dependence of DNP enhancement on sample composition, radical concentration, relaxation properties of the API and excipients, types of polarizing agents and proton density, has been thoroughly investigated. Optimal enhancement values are obtained from ASDs containing 1% w/w radical concentration. Both polarizing agents TOTAPOL and AMUPol provided reasonable enhancements. Partial deuteration of the excipient produced 3x higher enhancement values. With these parameters, an ASD containing posaconazole and vinyl acetate yields a 32-fold enhancement which presumably results in a reduction of NMR measurement time by ~1,000. This boost in signal intensity enables the full assignment of the natural abundance pharmaceutical formulation through multidimensional correlation experiments

6.1 Introduction

The stability, solubility, and bioavailability of active pharmaceutical ingredients (APIs) are key determining factors of pharmaceutical formulation performance. Drug molecules can undergo undesired phase transformations, such as amorphous and crystalline interconversion, salt formation, and disproportionation induced by chemical, physical and pharmaceutical processes - transformations that often result in significant alterations in drug bioavailability. As a consequence analysis by differential scanning calorimetry (DSC), thermogravimetric analysis (TGA), powder X-ray diffraction (PXRD), Raman, and mass spectrometry are routinely employed to monitor the physicochemical properties of an API during drug formulation. In addition to these techniques, magic angle spinning (MAS) NMR can shed light on atomic scale molecular structures, quantify various solid-state forms, and probe molecular dynamics and chemical interactions in a nondestructive and noninvasive manner.[1-7] Although powerful, high throughput measurements by MAS are limited due to the inherently low sensitivity. Detection becomes even more challenging in enabled formulations that contain small amounts of poorly soluble API dispersed in a polymeric matrix for enhancing bioavailability. Furthermore, MAS detection on nuclei other than ^{1}H suffers from both the low natural abundance and the low gyromagnetic ratios of ^{13}C and ^{15}N when compare to ^{1}H , making it impractical to perform multidimensional correlation experiments in a reasonable amount of time for exploration of subtle molecular information.

The sensitivity of NMR can be improved by 2-3 orders of magnitude[8-14] by using dynamic nuclear polarization (DNP), which transfers the high polarization of unpaired electrons to nearby nuclei such as ^{1}H, ^{13}C, and ^{15}N via microwave irradiation of the electron-nuclear transitions. The maximum theoretical enhancement factor is given by $\varepsilon_{max}= g_e/g_n$ =658 where g_e and g_n are the gyromagnetic ratios of the electron and nuclei, respectively. Thus, even a fraction of this translates into a time saving of months or years, enabling many otherwise infeasible experiments to be performed.[15, 16] The recent developments of high-power microwave sources, NMR probes for cryogenic MAS, biradical polarizing agents, and new sample preparation methods, have enabled DNP to be successfully applied to investigate the dynamics and structures of microcrystalline peptides, membrane proteins, amyloid fibrils, natural products and catalytic materials.[17-29]

Recent studies have demonstrated the considerable potential of DNP in applications to pharmaceutical chemistry.[30-36] The major challenge to successful DNP experiments lies in developing a suitable method of introducing polarizing agents into to the sample for optimum signal enhancement without sample disruption. A number of methods for preparing DNP

pharmaceutical samples have been reported, including polymer film casting and glass forming methods.[34, 37]. In addition, Emsley and coworkers have successfully demonstrated an innovative impregnation method on the pharmaceutical formulations with an organic solvent (*1,1,2,2*-tetrachloroethane) containing polarizing agents.[24] Enhancements in the range of 40-90 were obtained for commercial formulations containing cetirzine dihydrochloride and excipients povidone, magnesium stearate, hypromellose, and lactose. These enhancements allow rapid characterization via one- and two-dimensional MAS spectra of these formulations with drug loading <10%. Very interestingly, molecular contacts between the API and povidone were evident in the ^{1}H -^{15}N correlation spectra. However, the use of organic solvents to dissolve radicals and impregnate formulations of interest can result in perturbations of physical and chemical properties of the components in a formulation. Indeed, in a study of theophylline, the impregnation strategy has been found to induce phase conversions that require further improved for broader application.[36] Beyond this, the use of solvents requires that polarizing agents have significantly different solubility from other components in the formulation, which limits the practical applications. Therefore, it is preferable to avoid solvents when incorporating polarizing agents into the sample.

The formulation of amorphous solid dispersions (ASDs) is desirable since it enhances drug solubility and bioavailability.[38] Therefore, there is a strong need for new tools to monitor and study the chemical and physical stability during the formulation development to ensure a stable product is delivered to the clinic. DNP can play an essential role in enhancing the capacity and efficiency of MAS NMR during early drug development and provide information on the risks related to drug phase changes in ASDs. Therefore, we have designed a protocol for the preparation of DNP samples with the goals of (1) introducing polarizing agents in a non-invasive manner to maintain the integrity of the sample and (2) utilizing intensity enhancement for rapid measurements to inform on formulation development. Our strategy is to evaluate the *in-situ* incorporation of the polarizing agents during the processes of spray drying (SD) and hot-melt extrusion (HME). These two processes are widely applied for preparing ASDs in the pharmaceutical industry. Briefly, in SD, a solution containing API, polymeric excipient, and free radicals, is sprayed against the flow of warm air that rapidly evaporates the solvent and produces a dried powder. In HME, samples are made by mechanically mixing the solid components at elevated temperatures, which creates an intimately combined melt of all the components that is subsequently cooled and milled into a powder.

In our proposed method for sample preparation, the radicals are co-dissolved or co-mixed with formulation components for SD and HME processes, respectively. In this report, a clotrimazole-copovidone binary dispersion was used as a model system to investigate the dependence of signal enhancement on the following parameters: concentration and type of polarizing agent, proton density, and ASD methods. The optimized conditions were then adopted to prepare an ASD composed of posaconazole and ^{2}H-vinyl acetate, giving a maximum DNP enhancement of 32. Our results also show no observable structure perturbation or any phase conversion of drug substance. We show that the large signal intensity increase assists in the full assignment of posaconazole resonances from two-dimensional homo- and heteronuclear correlation experiments. To the best of our knowledge, this is the first documented DNP study investigating pharmaceutical formulations prepared by spray drying and hot-melt extrusion.

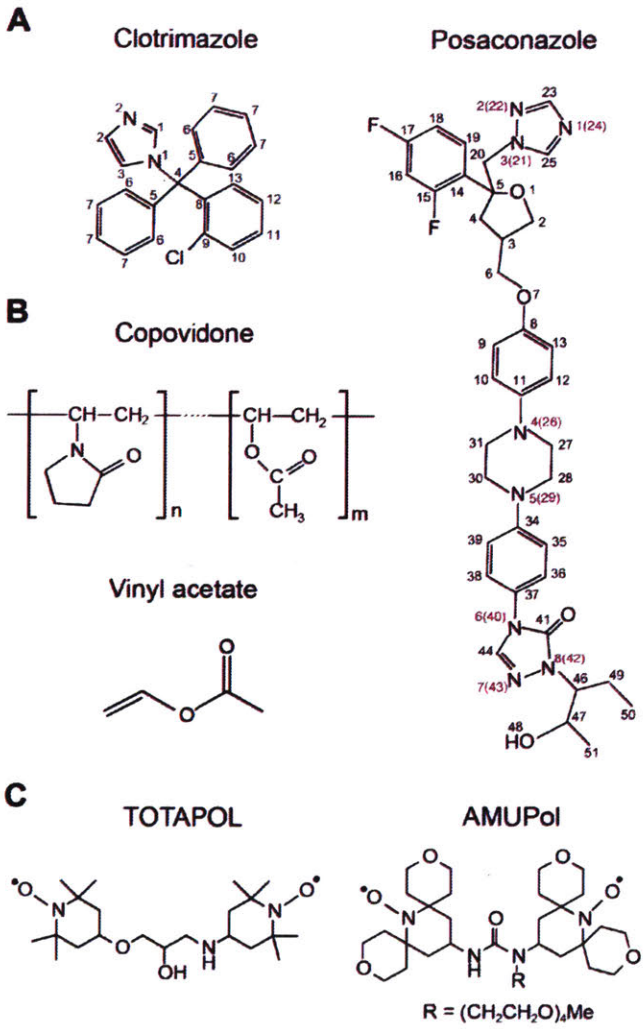

Figure 6.1: (A) Chemical structures of the two APIs clotrimazole and posaconazole, (B) the polymeric excipients copovidone (n:m = 1.2) and vinyl acetate, and (C) the biradical polarizing agents TOTAPOL and AMUPol. All atoms in clotrimazole and posaconazole are labeled for NMR resonance assignments in the subsequent DNP-enhanced experiments.

6.2 EXPERIMENTAL:

6.2.1 Materials

Molecular structures of the materials (API's, polymers and biradical polarizing agents) used in our study are shown in **Figure 6.1.** Copovidone Kollidon® VA64, an amorphous random copolymer of 1-viny-2-pyrrolidone and vinyl acetate (60:40 mass ratio and 45-70 kDa molecular weight), was obtained from BASF. Vinyl acetate (VA) was purchased from Polymer Source, Inc. The API clotrimazole and posaconazole were products of Spectrum Chemical Inc. and Merck Research Laboratories (MRL), respectively. TOTAPOL [39] and

AMUPol [40] are biradical polarizing agents and were both evaluated to enhance MAS NMR signal intensities. TOTAPOL was
available from Dynupol, Inc., and AMUPOL was a gift from and Dr. Olivier Ouari and Prof. Paul Tordo (Aix-Marseille Université). Methanol (HPLC grade from Sigma-Aldrich) was used as a solvent for the spray-drying process. All chemicals were used as received.

6.2.2 Sample preparation

Solid dispersions of all samples were prepared by either spray drying or hot-melt extrusion (**Figure 6.2**). In both cases, a binary physical mixture of API and polymer at a desired weight ratio was prepared by blending in a Turbula mixer. The drug loading (API to polymer mass ratio) was 20% in all preparations, except for the 1% (w/w) drug loading of clotrimazole-copovidone ASD reported in the Supplementary Information (**Figure 6.10),** which showcases the capability of DNP to detect very weak signals. Typically, ~100 g of the mixture was sealed in a 500 mL glass bottle and blended for 1 hr at room temperature. The mixture then underwent spray drying or hot-melt extrusion processes as described below. Pure API and polymer samples were made with the same protocol.

Spray drying was conducted on a ProCepT 4M8-TriX Formatrix spray dryer equipped with a 0.6 mm bifluid nozzle. First, a solution of polymer and API in methanol (~20-40 mg/ml) with the desired amount of radical (0-2% weight ratio in the dried product) was prepared. The solution was then sprayed against a stream of air flowing at 0.4 m^3/min. The solution was fed into the atomizing nozzle at a rate of 5 mL/min and atomized using compressed air at 70 psi. The inlet and outlet temperatures were 353 K and 323 K, respectively. The dried powders were collected and stored at room temperature in 10 mL amber glass bottles in a desiccator.

Hot-melt extrusion (HME) was performed with a customized micro twin screw extruder (MP&R™ Model ME7.5) equipped with co-rotating conveying screws which have a diameter and length/diameter ratio (L/D) of 7.5 mm and 15:1, respectively.[41, 42] In a typical process, ~3 g of the blended binary physical mixture at a desired radical content were fed into the extruder by a vibratory feeder. The barrel temperature was set at 418 K and the screw frequency was 100 rpm. The hot-melt extrudates were collected, allowed to cool, milled into powder via a benchtop mill (Polymix PX-MFC 90 D), and stored in a desiccator at room temperature.

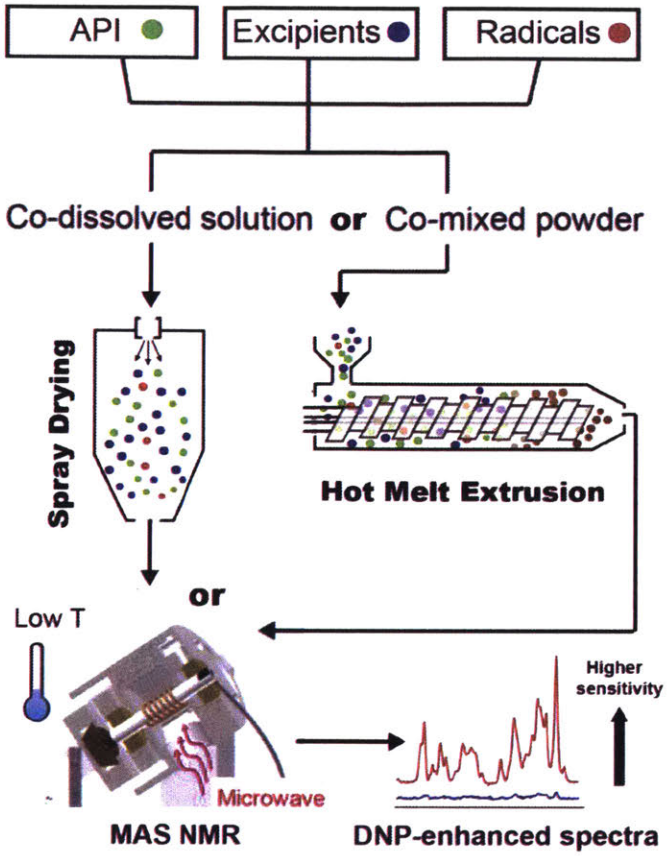

Figure 6.2: (a) Pulse sequence for the frequency-swept integrated solid effect. ^{1}H signals are detected with a solid echo. (b) During the sweep, the spin system undergoes three adiabatic events including DQ and ZQ at A and B, respectively, as well as electron spin inversion at O. The semicircle represents the relationship $\omega_{0I}^2 = \Omega^2 + \omega_{1S}^2$, which is satisfied at A and B where Ω is the microwave frequency offset. The inversion leads to the constructive addition of DNP enhancement at A and B, thus the name integrated solid effect.

6.2.3 DNP/NMR experiments

In order to assess the optimum sample condition, ^{1}H-^{13}C/^{15}N cross polarization (CP) experiments were performed on a home-built DNP/NMR instrument operating at 250 GHz/380 MHz with ~14 W of microwave power.[43, 44] Spectra were recorded using a triple resonance (^{1}H, ^{13}C and ^{15}N) cryogenic MAS probe equipped with a sample exchange system[45] on a home-built NMR spectrometer operating at 9 T at T=85 K. Approximately 45 mg of each powder sample was packed into a 4 mm sapphire rotor. The spinning frequency is $\omega_r/2\pi$ = 5.5 kHz unless stated otherwise. $\omega_{1H}/2\pi$ = 50 kHz was employed during CP and a TPPM decoupling field $\omega_{1H}/2\pi$ = 100 kHz was used during acquisition. T_{1H} was measured using saturation recovery sequence (**Figure 6.11**). Enhancement factors (ε) were calculated by comparing the signals obtained with and without microwave irradiation.

Further characterization by 2D correlation MAS was carried out on a 263 GHz/400 MHz system (consisting of an Avance III HD console, Ascend 9.4 T NMR magnet, and 263 GHz gyrotron) and a 395 GHz/600 MHz system (Avance III HD console, Ascend Aeon 14.1 T magnet, and 395 GHz gyrotron). The microwave power at the sample was ~10 W on both systems. Approximately 20 mg of each powder sample was packed into 3.2 mm sapphire rotors. At 400 MHz and 600 MHz, $\omega_r/2\pi$ = 9 kHz and 12.5 kHz, respectively. Two kinds of 2D NMR experiments were performed, including ^{13}C-^{13}C refocused INADEQUATE (Incredible Natural Abundance Double Quantum Transfer Experiment) of clotrimazole and ^{1}H-^{13}C and ^{1}H-^{15}N HETCOR (Heteronuclear Correlation) of posaconazole. The refocused INADEQUATE spectra were acquired with a recycle delay of 2 s, 80 t_1 increments, and 384 scans per increment, for a total experiment time of ~17 hr. The HETCOR spectra of posaconazole were acquired with a recycle delay of 3 s, 64 t_1 increments, and 256 scans per increment, for a total experiment time of approximately 14 hr. Both short and long contact time (0.45 ms and 1.5 ms, respectively) HETCOR spectra were acquired to assist with assignments. The sample temperature during these experiments was 99 ± 2 K, as calibrated using KBr.[46] 2D spectra were processed with zero-filling to double the size and a Gaussian window function centered at 0.1 and 50 Hz of broadening, in both the direct and indirect dimensions. Quadrature detection in the indirect dimension was accomplished using the States-TPPI scheme. All DNP/NMR pulse sequences are included in **Figure 6.11**.

6.3 RESULTS AND DISCUSSION:

6.3.1 Polarizing agent concentration

The enhancement and ^{1}H relaxation properties of spray-dried samples with increasing concentrations of TOTAPOL (0%, 0.5%, 0.75%, 1% and 2%, w/w) were measured and are shown in **Figure 6.3**. Three different sample compositions were used, including pure API clotrimazole (**Figure 6.3A**), pure polymer copovidone (**Figure 6.3B**), and a clotrimazole/copovidone binary formulation (**Figure 6.3C**). We found that for samples containing clotrimazole (**Figure 6.3A** and **3C**), the optimal radical concentration was 1%. We note that both SD and HME involve elevated temperatures especially HME (418 K, *vide supra*), which can potentially lead to thermal degradation of nitroxide radicals. However, the TGA analysis (data not shown) showed that TOTAPOL and AMUPol did not undergo thermal degradation until temperatures of 516 K and 526 K, respectively, which is significantly higher than the processing conditions. Furthermore, EPR spectra (**Figure 6.12)**

share the same characteristics as the published data suggesting that the nitroxides remained intact through the SD and HME processes.[47] EPR spectra also showed no sign of radical aggregation. To evaluate the possibilities of sample perturbations induced by the addition of radicals, we have compared ASDs with and without TOTAPOL using ssNMR and PXRD, shown respectively in **Figure 6.13** and **Figure 6.14**. No chemical shift change is observed in the ^{13}C NMR spectra and the X-ray powder pattern also confirms the amorphous nature of the ASDS, suggesting no amorphous to crystalline conversion.

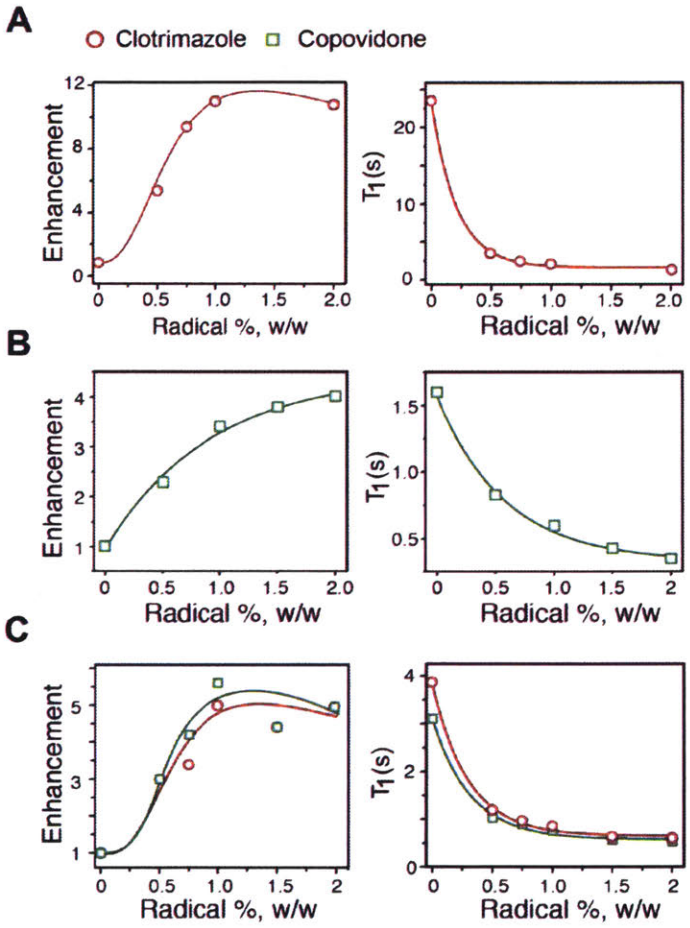

Figure 6.3: Dependence of DNP enhancement and spin-lattice relaxation property on radical concentration for clotrimazole (A), copovidone (B), and spray dried clotrimazole-copovidone ASD (C). Enhancement and T_1 measurements are shown in the left and right columns, respectively.

Note also that, to date, DNP applications usually involve solutions of polarizing agents and require 5-10 mM of biradical.[8] The optimum concentration in our method is 2-3 times higher, with 1% weight ratio corresponding to roughly 20 mM of biradical. This may be due

to the spatial distribution of the radical in the solid state, where not all radicals are in close proximity to the polymer and/or API.

In **Figure 6.3B**, the enhancement of copovidone signal monotonically increased with increasing TOTAPOL and did not saturate at 2% TOTAPOL concentration. We attribute this to polymer motions and hence, the very short T_1 (1.6 s) of ^1H in copovidone in the absence of radical. In comparison, pure clotrimazole has much longer T_1 (24 s). However, both components in the clotrimazole/copovidone mixture exhibit essentially the same proton T_1 of ~3.5 s (**Figure 6.3C**), suggesting a good miscibility of the components, which is an indicator of stable pharmaceutical formulations.[48] The miscibility is further supported by the fact that the DNP enhancement is uniform throughout the samples regardless of the radical concentration. A good miscibility in a solid-state mixture is required for efficient ^1H-^1H spin diffusion, which in turn results in a uniform T_1 and DNP enhancement. Thus, the DNP enhancement may be a useful indicator of the miscibility of pharmaceutical formulations. Both the enhancement and T_1 values of the combined dispersion are roughly equal to the weighted arithmetic average of the two individual components, indicating that the nitroxide is evenly distributed amongst both members.

An optimum radical concentration is determined based on several parameters. On one hand, higher polarizing agent concentrations provide a denser electron pool, which leads to higher enhancement values. On the other hand, the electrons in the nitroxides are paramagnetic species and lead to paramagnetic relaxation enhancement (PRE) effect. This effect shortens the spin-lattice (T_1) and spin-spin relaxation (T_2) times of nearby nuclei. As a consequence, the PRE effect on T_2 leads to line broadening, loss of resolution and the inability to acquire multidimensional NMR experiments that require T_2 for polarization transfer.[45, 49] Therefore, the optimal polarizing agent concentration is a balance of maximizing electron to proton polarization transfer while minimizing PRE effects.

6.3.2 Proton density

We have investigated the impact of proton density by comparing spray dried intermediates containing either protonated or deuterated vinyl acetate (VA). Both samples were loaded with 20% API clotrimazole and 1% TOTAPOL. Deuterated VA resulted in a greater than threefold improvement in the DNP enhancement (12 vs. 3.6, **Figure 6.4A**), similar to the result found previously in other sample preparation methods.[50-52] In experiments based on CP and detection on low gamma nuclei such as ^{13}C or ^{15}N, the benefit of diluting ^{1}H in the solvent is twofold. First, it reduces the ratio between the populations of protons and electrons. Second, diluting the ^{1}H bath lengthens the intrinsic proton T_1 of an undoped sample by attenuating ^{1}H-^{1}H dipole interactions and/or dynamics. The remaining ^{1}H concentration is sufficient to disperse the electron polarization via spin diffusion and transferring that polarization to ^{13}C or ^{15}N via CP. Previous work from Griffin's group has established glass-forming matrix containing glycerol-d_8/D_2O/H_2O (60/30/10, v/v) as a solvent of choice to form a frozen glassy matrix at T < 220 K, and it is used in the

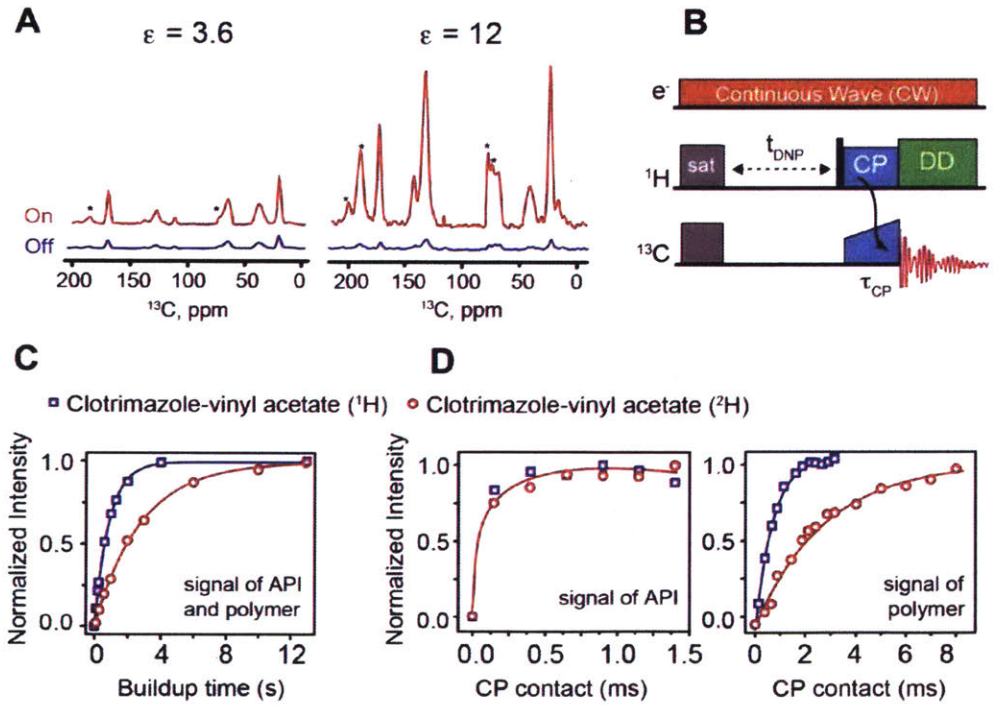

Figure 6.4: (A) Enhancement spectra of clotrimazole-vinyl solid dispersion samples: ^{1}H vinyl acetate (left) and ^{2}H vinyl acetate (right). (B) Pulse sequence for measuring the dependence of polarization transfer on DNP buildup time, t_{DNP} and CP contact time, t_{CP}. Build-up curves of DNP (C) and CP (D) for ^{1}H vinyl acetate (blue) and ^{2}H vinyl acetate (red) containing dispersions. In (C), API and polymer exhibit identical t_{DNP}. In (D), CP buildup curves for API and polymer are shown on the left and right, respectively. All data were obtained using 50 kHz of proton spin lock during CP and 100 kHz ^{1}H dipolar decoupling during acquisition at

majority of DNP biological applications.[50, 53] Subsequent studies have explored the use of organic solvents for applications involving insoluble materials; nevertheless, a deuteration level of ~90% remains standard.[49, 54-57] In addition, Akbey *et al.* obtained a 3-5 fold larger enhancement using perdeuterated then back exchanged SH3 protein instead of protonated samples.[52]

In **Figure 6.4B-D,** we study the effect of deuteration on polarization transfer processes during DNP and CP. The pulse sequence for measuring these polarization dynamics is shown in **Figure 6.4B**. After saturation (sat) irradiation, the magnetization of protons is enhanced by DNP and then transferred to ^{13}C via CP for detection. DNP buildup curves in **Figure 6.4C** showed that the polarization for the protonated vinyl acetate containing sample reached equilibrium at ~ 4 s, much faster than that for the deuterated one (~ 12 s). This is as expected since protonated polymer has denser ^{1}H matrix for more efficient spin diffusion. As shown in **Figure 6.4D**, we observed essentially the same CP buildup curve for the signals from the clotrimazole (left curves in **D**), whereas signals of protonated and deuterated VA displayed different CP dynamics (right curves in **D**). Deuterated VA required significantly longer CP contact time (8 ms vs. 3 ms) which strongly suggests intermolecular CP from ^{1}H of the API to the ^{13}C of the deuterated polymer. Previously, such information was obtained via ^{1}H-^{1}H and ^{19}F-^{1}H spin diffusion between API and polymer in formulations.[2] Our result opens up a new possibility of obtaining intermolecular contact between API and polymer in pharmaceutical formulations using deuterated polymer excipients.

6.3.3 Hot-melt extrusion vs. spray drying

With the full optimization of DNP enhancement for ASDs prepared via SD, our next goal is to investigate the enhancement performance on dispersions prepared by different techniques. Of particular interest is HME, a low-cost and environmentally friendly method developed over the last three decades for preparing polymer-based ASDs of low solubility drugs. Different from the SD process, where the radical-containing ASD is produced by rapidly evaporating the volatile methanol solvent into hot air and has the advantage of a lower processing temperature which minimizes the thermal degradation of nitroxide radicals, the HME process involves mechanically mixing various ingredients at an elevated processing temperature, thus requiring no solvent and no specific solubility of API, polymer or DNP radical.

Figure 6.5 compares the DNP enhancement and T_1 relaxation of clotrimazole/copovidone ASDs produced by HME and SD, each with various TOTAPOL concentrations. The HME curve shows that the enhancement reaches a maximum at 0.5%

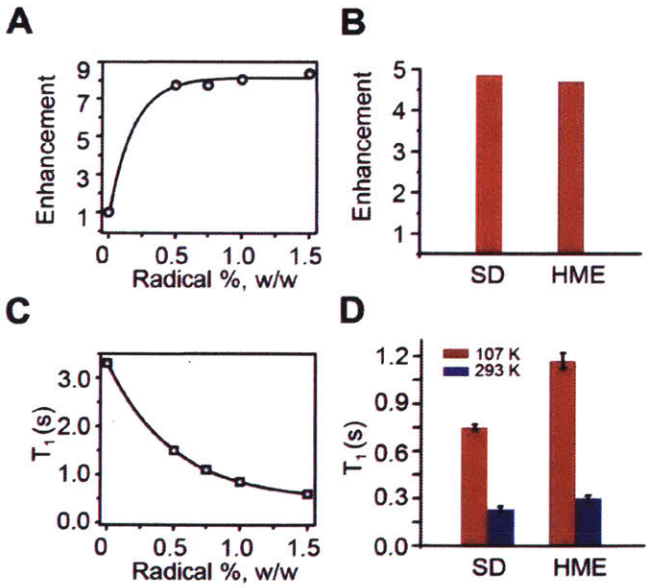

Figure 6.5. (A) DNP enhancement of extruded clotrimazole/copovidone dispersion with varying (w/w) concentrations of TOTAPOL. (B) Similar enhancement of clotrimazole-copovidone with 1% TOTAPOL prepared via SD and HME. (C) T_1 of the HME samples, measured using a saturated recycle delay value with ^{1}H-^{13}C CP experiments with 50 kHz of proton spin lock during CP and 100 kHz ^{1}H decoupling during acquisition at 380 MHz, 90 K. (D) Room temperature (blue) and low temperature (red) T_1 values of Clotrimazole-copovidone with 1% TOTAPOL prepared by SD and HME.

(w/w) radical concentration and remains saturated as the radical concentration is increased, presumably allowing for a greater range of optimal radical concentration than the SD method. Nevertheless, **Figure 6.5B** shows that both of these enabled formulation methods yield comparable DNP performances, ε=5 for clotrimazole/copovidone ASD with 1% TOTAPOL.

HME T_{1H} measurement exhibits a slightly weaker PRE effect on the relaxation at a higher nitroxide concentration in **Figure 6.5C.** Due to slower molecular motions at the colder temperatures, T_{1H} values are roughly 4 times longer at cryogenic temperature than at ambient temperatures as shown in **Figure 6.5D**. With 1% TOTAPOL (w/w), the T_1 values are approximately 1 s at 107 K for both HME and SD (as reported in **Figure 6.3**). The absolute value of T_1 is an indicator of factors such as particle size, humidity, API-polymer interaction resulting from the dispersion processes as well as the PRE effect. The fact that different processes are suitable for *in-situ* DNP sample preparation diversifies the collection of pharmaceutical compounds and formulations accessible by our approach. Overall, the two ASD methods yielded similar DNP performances, suggesting the forgiving nature of introducing polarizing agents in wet and dry manners. Furthermore, it permits selection of the method based on its advantages.

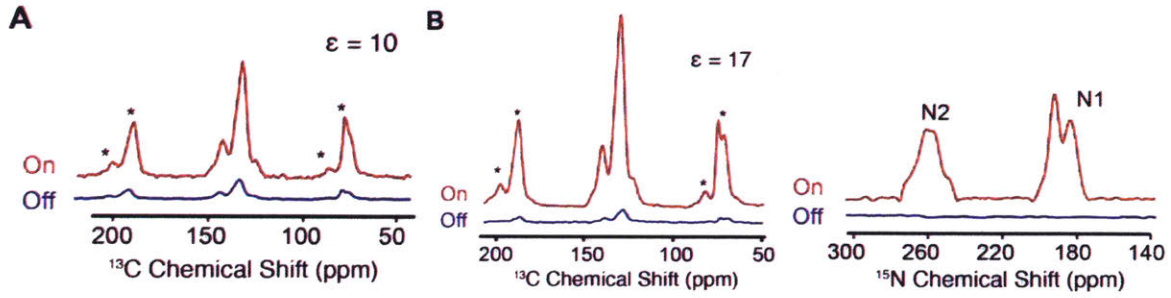

Figure 6.6 DNP-enhanced natural-abundance ^{13}C and ^{15}N CP-MAS spectra showing enhancements of (A) clotrimazole doped with 1% TOTAPOL and at 90 K and (B) 1% AMUPol at 104 K. Enhancements are 10 and 17 at 380 MHz, respectively. The ^{13}C spectra were acquired with 8 scans, recycle delay of 4 s and the ^{15}N spectrum was collected with recycle delay of 3 seconds and 8k scans.

6.3.4 Enabling multidimensional MAS NMR spectroscopy for analyzing pharmaceutical formulation

In the previous sections, DNP enhancements of various clotrimazole samples conditions were investigated, including the concentration and types of polarizing agents, proton density, and dispersion techniques. In this section, we present DNP/NMR structural

investigations of the samples prepared by the enabled formulation methods. To this end, we first further improved the DNP enhancement by using AMUPol instead of TOTAPOL as the polarizing agent. **Figure 6.6** shows the ^{13}C spectrum of clotrimazole doped with 1% TOTAPOL and ^{13}C, ^{15}N of the same API doped with 1% AMUPol taken at 380 MHz. The enhancement with AMUPol was 17, which roughly doubled that obtained with TOTAPOL.

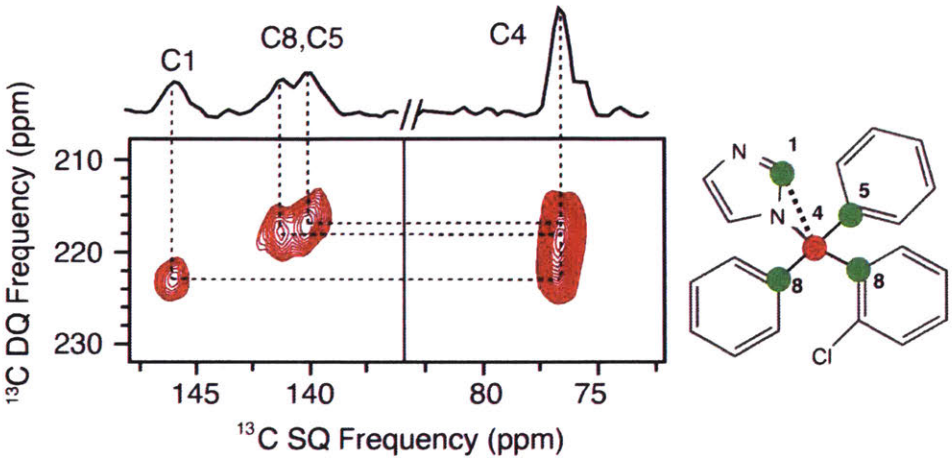

Figure 6.7 2D ^{13}C-^{13}C refocused INADEQUATE spectrum of clotrimazole showing intramolecular contacts among ^{13}C resonances as marked in the molecular structure on the right. The full spectrum is included in the **Figure 6.15**. The 2D spectrum was acquired in 17 hr at 106 K on 400 MHz, 384 scans per increment, 2 s recycle delay and 80 t_1 increments of a 27.7 us.

Our result is in good agreement with previous studies that established AMUPol as the radical of choice for DNP applications at ~ 100 K.[10, 40, 58] The superior performance of AMUPol facilitates the detection of low natural abundance and low gamma nuclei such as ^{15}N. In the 1D ^{1}H-^{15}N CP of **Figure 6.6**, both nitrogen atoms on the imidazole group can be assigned. The doubling of N1 and broadening of N2 suggest that the molecules may adopt two different amorphous forms.[59]

The large improvement in the sensitivity facilitates 2D ^{13}C-^{13}C homonuclear correlation experiments as shown in **Figure 6.7**. The homonuclear ^{13}C-^{13}C spectrum of clotrimazole was acquired using refocused-INADEQUATE, a pulse sequence establishing ^{13}C-^{13}C correlations from magnetization transfer through J-couplings.[24, 33, 60, 61] In **Figure 6.7**, correlations of C4 with C1, C5, C8 are identified based on previous assignments. The contacts between aromatic carbons are shown in the full 2D refocused-INADEQUATE in **Figure S6**. The optimized parameters provide this successful a example of investigating intramolecular carbon-carbon correlations of natural abundant drugs using DNP-enhanced

MAS NMR.

These optimized sample conditions (*vide supra*) were also applied to the study of the commercialized drug posaconazole, which is a triazole antifungal drug (trade name Noxafil).[62, 63] An ASD containing the API posaconazole and polymeric excipient ^{2}H-vinyl acetate with 1% AMUPol was prepared via spray drying. The DNP-enhanced ^{13}C spectra are shown in **Figure 6.8**. An enhancement of 25 was obtained for the posaconazole ASD, determined from the microwave-on and -off spectra spinning at 9 kHz in **Figure 6.8A**. Previous studies have suggested the enhancement dependence on MAS frequencies.[10, 64, 65] Further optimization exhibited a maximum enhancement of 32 at $\omega_r/2\pi$ = 5kHz, as shown in **Figure S7**. Compared to clotrimazole/^{2}H-vinyl acetate, higher DNP enhancement was achieved for posaconazole/^{2}H-vinyl acetate ASD, likely due to differing molec ular interactions and packings between radicals and APIs. Deuteration of the polymer not only improves the enhancement by a factor of 3-4, but also simplifies the analysis of API signals by suppressing signals originated from the polymer. The ^{15}N spectrum in **Figure 6.8B** was acquired in 1 hr, while without DNP enhancement, it would have taken almost a month to achieve the comparable sensitivity for the same amount of samples. All eight ^{15}N atoms in the drug molecule can be seen and tentatively assigned according to previous publications.[63] To complete the resonance assignments and establish the intramolecular correlations, 2D heteronuclear experiments were conducted as illustrated in **Figure 6.9**.

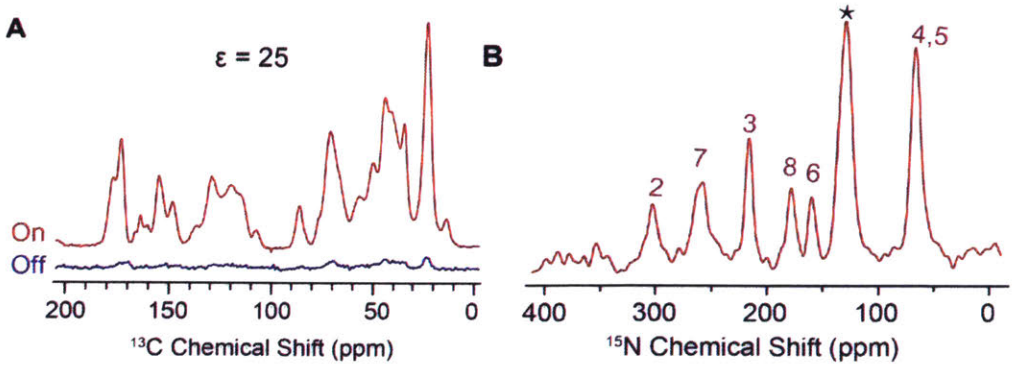

Figure 6.8 DNP-enhanced (A) ^{13}C and (B) ^{15}N CP-MAS spectra of natural abundance posaconazole-deuterated vinyl acetate ASD. Both experiments were conducted with $\omega_r/2\pi$ = 9 kHz. The enhancement value dependence on spinning frequency is presented in **Figure 6.16**. The ^{13}C spectrum was recorded with 128 scans, recycle delay of 10 s. The ^{15}N spectrum was acquired with 1024 scans, recycle delay of 4 s.

Pharmaceutical solids are often disordered and multicomponent systems, leading to low resolution in spectroscopic investigations. To obtain unambiguous and high-resolution information for structural elucidations, it is best to use 2D MAS NMR techniques to establish intra- and intermolecular correlations. However, multidimensional correlation becomes extremely challenging and often practically infeasible for low-γ spins, such as ^{13}C and ^{15}N rich drug molecules. DNP-enhanced ^{13}C- and ^{15}N-detected correlation experiments were performed as shown in **Figure 9A** and **B**, respectively. Taking 2D ^{13}C-^{1}H HETCOR in

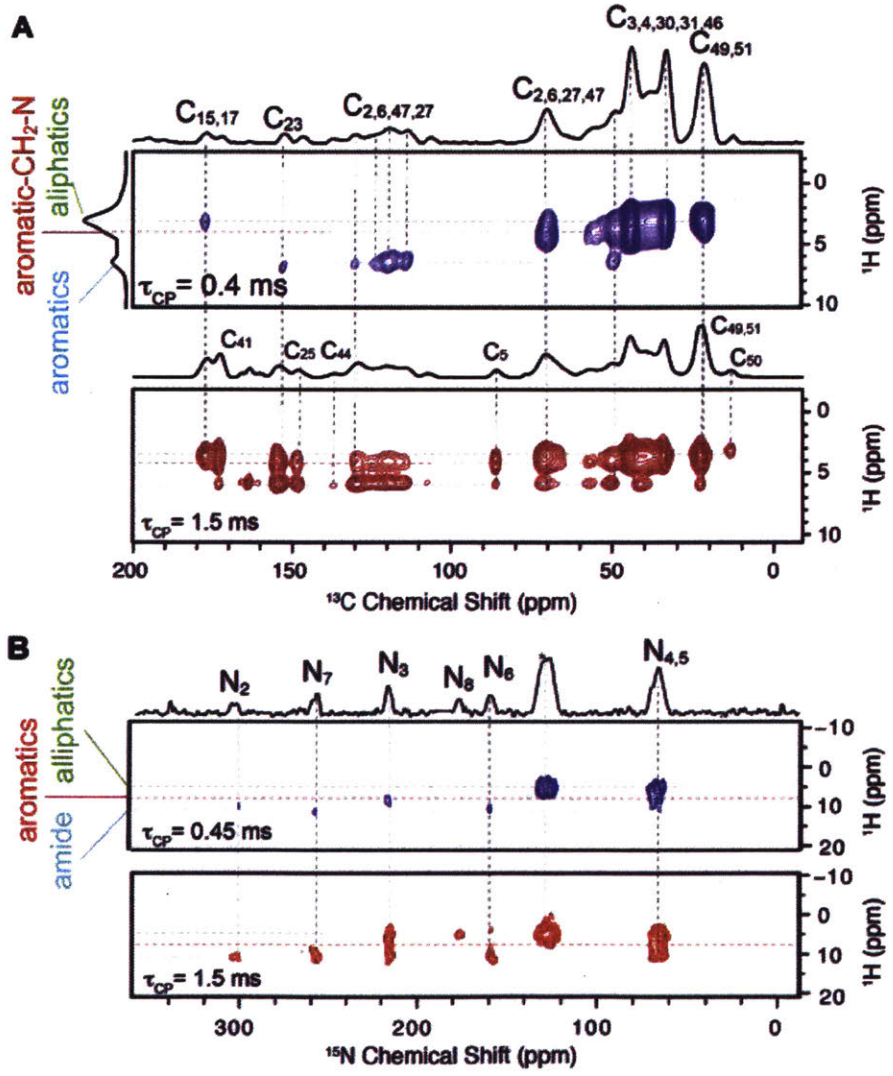

Figure 6.9 2D DNP-enabled heteronuclear correlation spectra of natural abundance posaconazole-^{2}H vinyl acetate ASD: (A) ^{13}C-^{1}H and (B) ^{15}N-^{1}H spectra with short and long mixing times. HETCOR pulse sequence is shown in **Figure 6.11**. Each HETCOR experiment was acquired in 7 hours at 106 K with 3 s recycle delay, 64 t1 increments, and 256 scans per increment at $\omega_r/2\pi$ = 9kHz. The ^{13}C-^{1}H and ^{15}N-^{1}H HETCOR spectra were acquired with FSLG homonuclear decoupling at 400 MHz and 600 MHz, respectively.

Figure 6.9A, for example, the spectra were collected with 0.4 ms contact times for correlations of short distances and 1.5 ms for long distances. In the ^{1}H dimension, three types of functional groups including aliphatic, aromatic-N, and aromatic protons can be assigned. At the short mixing time (blue), the cross peaks between adjacent protons and carbon are observed, e.g., cross peaks between C3, 4, 30, 31 and aliphatic protons; C18, 19 and aromatic protons. Giving a longer spin diffusion transfer (red), ^{13}C-^{1}H cross peaks of those at a farther distance appear, e.g., aliphatic C27 and aromatic protons. Distance information is encoded in these correlations at short and long diffusion times, facilitating the assignments of most carbons. [62]

2D ^{1}H-^{15}N HETCOR spectra were also acquired at short (0.45 ms) and long (1.5 ms) mixing times. (Figure 9B) Cross peaks are observed between all eight nitrogen atoms and their neighboring protons including aliphatic, aromatic, and amide protons. Given the fact that ^{15}N has lower γ (-4.316 MHz/T) and natural abundance (0.368%) among the spins of interest in pharmaceutical molecules, it is worth emphasizing the success of acquiring these 2D spectra in 7 hrs, a reasonably short period of time for practical analysis. These results have shown DNP as a powerful technique for enhancing ssNMR signal intensities for investigating structures and probing interactions of natural abundance drugs and formulations.

6.4 CONCLUSION

In summary, our study has served as the first documented example of an *in-situ* preparation of DNP samples to support structural investigations of practical formulation processes. Polarizing radicals have been successfully incorporated during routine pharmaceutical production of solid dispersions including SD and HME. The DNP enhancement has been optimized by investigating the sample and its relaxation parameters. Partial deuteration of ASDs results in more than a threefold increase in enhancement value. An optimum enhancement of 20-30 was obtained and enables detection of low drug loading (i.e. 1%) formulations and the 2D homonuclear ^{13}C-^{13}C and heteronuclear ^{13}C-^{1}H and ^{15}N-^{1}H correlations for structural investigations of pharmaceutical formulations.

6.5 ACKNOWLEDGMENT

This research was supported by Merck-MIT scientific collaboration funding to R.G.G. and Y.S., and by National Institute of Health Grants EB-002804, EB-002026, EB004866 and EB001965.

6.6 SUPPORTING INFORMATION

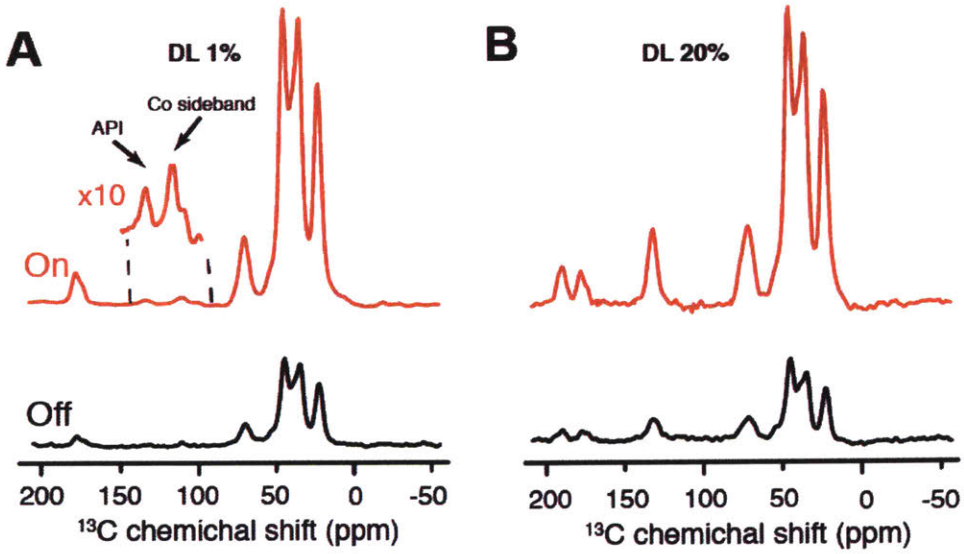

Figure 6.10 DNP enhanced microwave (mw)-on and -off spectra of clotrimzaole-copovidone amorphous solid dispersions (ASD) at drug loadings (DL) of 1% (A) and 20% (B). All samples contain 1% TOTAPOL. A signal enhancment of 4 is obtained. The MW-on spectra were aquired with 2048 scans and a recycle delay (RD) of 2 seconds, at 93 K at 380 MHz (^{1}H Lamor frequency).

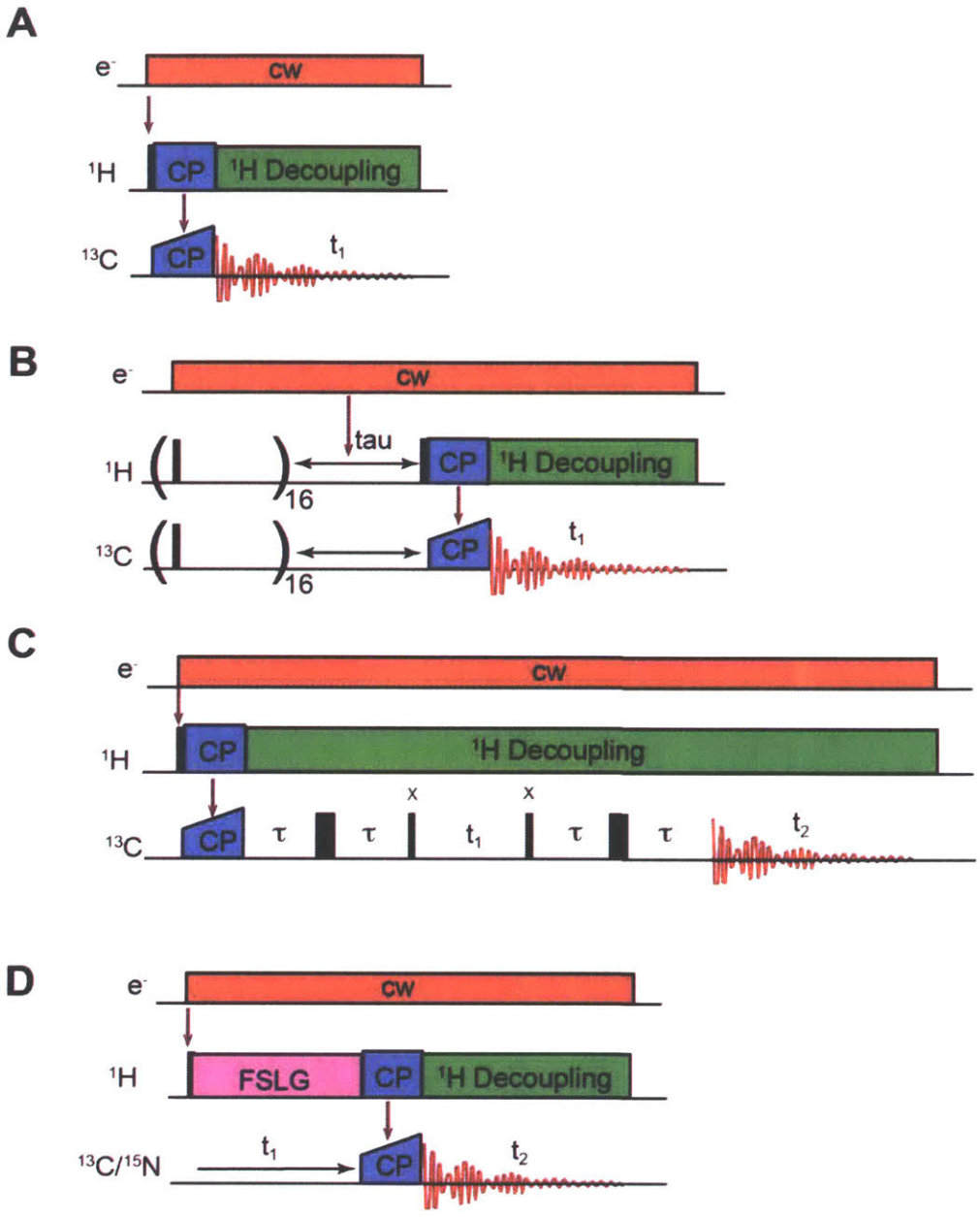

Figure 6.11 Pulse sequences utilized in this study: (A) ^{1}H-^{13}C cross polarization MAS. (B) Time-dependent T_{DNP} buildup and T_1. (C) Refocused INADEQUATE (Incredible Natural Abundance Double Quantum Transfer Experiment) and (D). HETCOR (Heteronuclear Correlation spectroscopy).

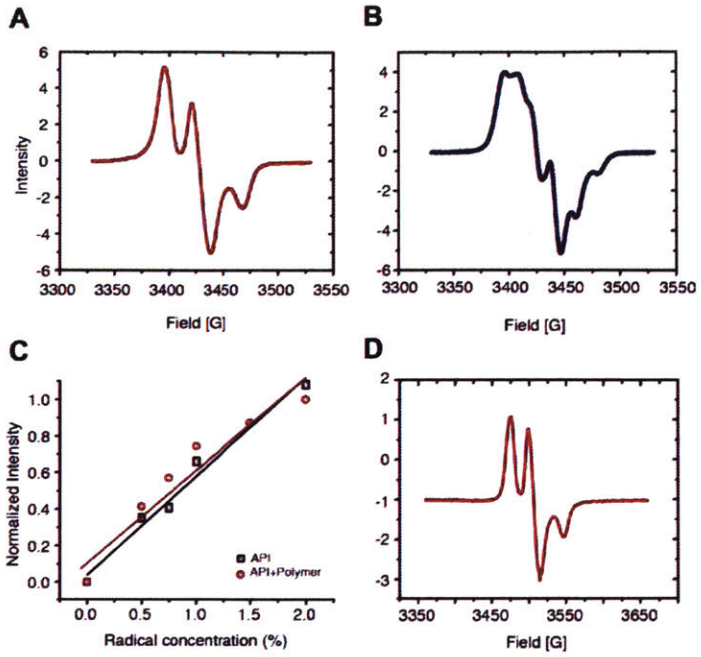

Figure 6.12. EPR characterization of radicals in CLT-copovidone ASDs in this study. (A) Spray dried dispersion containing 1%TOTAPOL. (B) Spray dried dispersion containing 1% AMUPol. (C) Normalized signal intensities of spray dried formulations of CLT (black) and CLT/copovidone (red) with varying weight percentages of TOTAPOL concentrations. (D) Hot melt extrusion formulation containing 0.5% TOTAPOL. All EPR spectra were acquired at 9 GHz.

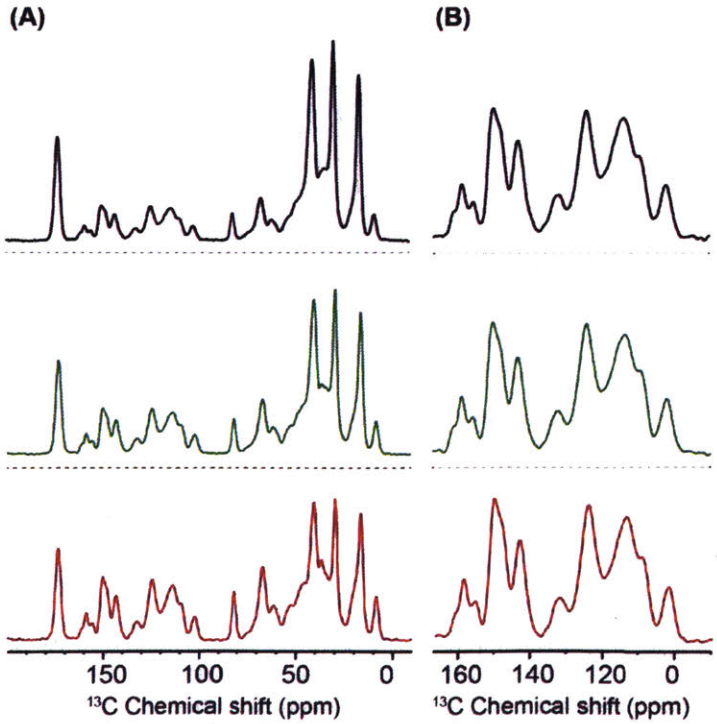

Figure 6.13. ^{13}C CP-MAS spectra of Posaconazole-PVP amorphous solid dispersions doped with 0% (black), 1% (green) and 2% (red) TOTAPOL: (A) full spectra and (B) enlarged region of API peaks.

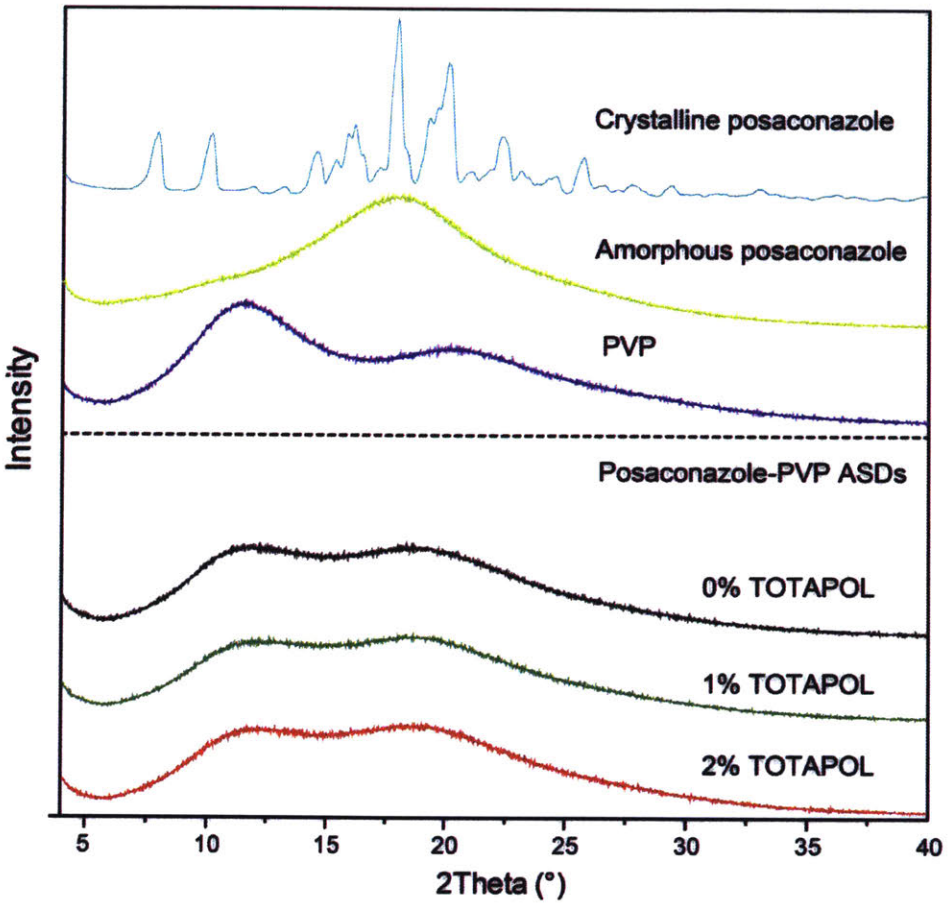

Figure 6.14 X-ray powder diffraction patterns of crystalline (blue) and amophours (yellow) posaconzaole, PVP (blue), and posaconazole-PVP amorphous solid dispersions doped with 0% (black), 1% (green) and 2% (red) TOTAPOL.

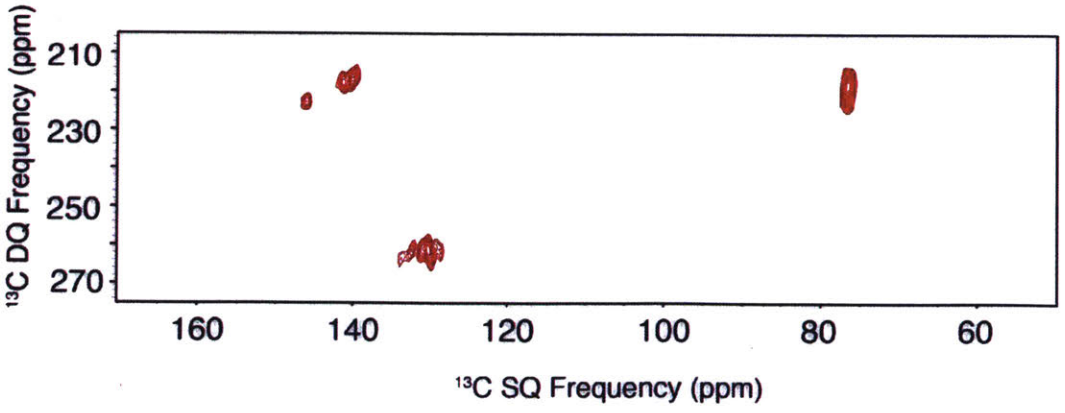

Figure 6.15 Full spectrum of ^{13}C -^{13}C refocused INADEQUATE correlation experiment of Clotrimazole doped with 1% AMUPol. The 2D spectrum was acquired in 17 hr at 106 K on 400 MHz, 384 scans per increment, 2 s recycle delay and 80 t_1 increments with 27.7 s t_1 increment.

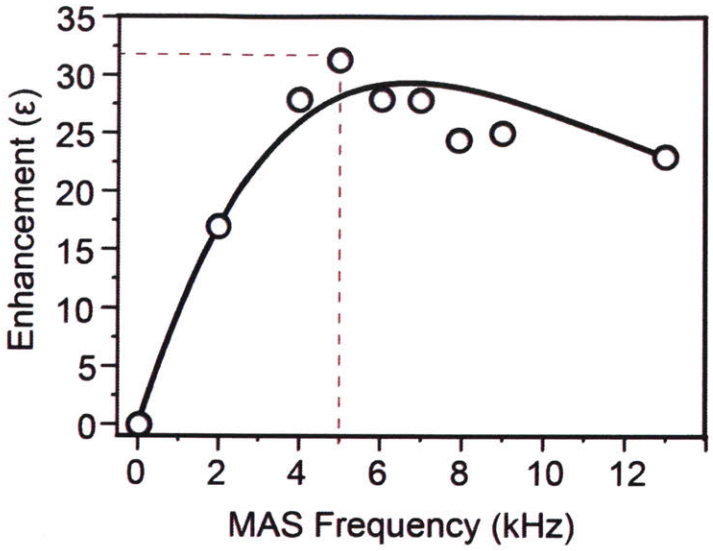

Figure 6.16 MAS frequency dependence of DNP enhancement of ^{13}C intensity for posaconazole-^{2}H vinyl doped with 1% AMUPol.

6.7 REFERENCES:

1. Paudel, A.; Geppi, M.; Van den Mooter, G. Structural and Dynamic Properties of Amorphous Solid Dispersions: The Role of Solid-State Nuclear Magnetic Resonance Spectroscopy and Relaxometry. *J. Pharm. Sci.* **2014,** *103,* 2635-2662.
2. Pham, T. N.; Watson, S. A.; Edwards, A. J.; Chavda, M.; Clawson, J. S.; Strohmeier, M.; Vogt, F. G. Analysis of Amorphous Solid Dispersions Using 2d Solid-State Nmr and 1h T1 Relaxation Measurements. *Mol. Pharm.* **2010,** *7,* 1667-1691.
3. Nie, H.; Su, Y.; Zhang, M.; Song, Y.; Leone, A.; Taylor, L. S.; Marsac, P. J.; Li, T.; Byrn, S. R. Solid-State Spectroscopic Investigation of Molecular Interactions between Clofazimine and Hypromellose Phthalate in Amorphous Solid Dispersions. *Mol. Pharm.* **2016,** *13,* 3964-3975.
4. Zencirci, N.; Griesser, U. J.; Gelbrich, T.; Apperley, D. C.; Harris, R. K. Crystal Polymorphs of Barbital: News About a Classic Polymorphic System. *Mol. Pharm.* **2014,** *11,* 338-350.
5. Watts, A. E.; Maruyoshi, K.; Hughes, C. E.; Brown, S. P.; Harris, K. D. M. Combining the Advantages of Powder X-Ray Diffraction and Nmr Crystallography in Structure Determination of the Pharmaceutical Material Cimetidine Hydrochloride. *Cryst. Growth Des.* **2016,** *16,* 1798-1804.
6. Griffin, J. M.; Martin, D. R.; Brown, S. P. Distinguishing Anhydrous and Hydrous Forms of an Active Pharmaceutical Ingredient in a Tablet Formulation Using Solid-State Nmr Spectroscopy. *Angew. Chem. Int. Ed.* **2007,** *46,* 8036-8038.
7. Tatton, A. S.; Pham, T. N.; Vogt, F. G.; Iuga, D.; Edwards, A. J.; Brown, S. P. Probing Intermolecular Interactions and Nitrogen Protonation in Pharmaceuticals by Novel 15n-Edited and 2d 14n-1h Solid-State Nmr. *CrystEngComm* **2012,** *14,* 2654-2659.
8. Su, Y.; Andreas, L.; Griffin, R. G. Magic Angle Spinning Nmr of Proteins: High-Frequency Dynamic Nuclear Polarization and 1h Detection. *Annu. Rev. Biochem.* **2015,** *84,* 465-497.
9. Ni, Q. Z.; Daviso, E.; Can, T. V.; Markhasin, E.; Jawla, S. K.; Swager, T. M.; Temkin, R. J.; Herzfeld, J.; Griffin, R. G. High Frequency Dynamic Nuclear Polarization. *Acc. Chem. Res.* **2013**.
10. Can, T. V.; Ni, Q. Z.; Griffin, R. G. Mechanisms of Dynamic Nuclear Polarization in Insulating Solids. *J. Magn. Reson.* **2015,** *253,* 23-35.
11. Can, T. V.; Walish, J. J.; Swager, T. M.; Griffin, R. G. Time Domain Dnp with the Novel Sequence. *J. Chem. Phys.* **2015,** *143,* 054201.
12. Barnes, A. B.; De Paëpe, G.; van der Wel, P. C. A.; Hu, K.-N.; Joo, C.-G.; Bajaj, V. S.; Mak-Jurkauskas, M. L.; Sirigiri, J. R.; Herzfeld, J.; Temkin, R. J., et al. High-Field Dynamic Nuclear Polarization for Solid and Solution Biological Nmr. *Appl. Magn. Reson* **2008,** *34,* 237-263.
13. Lee, D.; Hediger, S.; De Paëpe, G. Is Solid-State Nmr Enhanced by Dynamic Nuclear Polarization? *Solid State Nucl. Magn. Reson.* **2015,** *66–67,* 6-20.
14. Smith, A. N.; Long, J. R. Dynamic Nuclear Polarization as an Enabling Technology for Solid State Nuclear Magnetic Resonance Spectroscopy. *Anal. Chem.* **2016,** *88,* 122-132.
15. Ravera, E.; Corzilius, B.; Michaelis, V. K.; Luchinat, C.; Griffin, R. G.; Bertini, I. Dnp-Enhanced Mas Nmr of Bovine Serum Albumin Sediments and Solutions. *J. Phys. Chem. B* **2014,** *118,* 2957-2965.
16. Becker-Baldus, J.; Bamann, C.; Saxena, K.; Gustmann, H.; Brown, L. J.; Brown, R. C. D.; Reiter, C.; Bamberg, E.; Wachtveitl, J.; Schwalbe, H., et al. Enlightening the Photoactive Site of Channelrhodopsin-2 by Dnp-Enhanced Solid-State Nmr Spectroscopy. *Proc. Natl. Acad. Sci. U.S.A.* **2015,** *112,* 9896-9901.

17. Smith, A. N.; Caporini, M. A.; Fanucci, G. E.; Long, J. R. A Method for Dynamic Nuclear Polarization Enhancement of Membrane Proteins. *Angew. Chem. Int. Ed. Engl.* **2015,** *54,* 1542-1546.
18. Daube, D.; Aladin, V.; Heiliger, J.; Wittmann, J. J.; Barthelmes, D.; Bengs, C.; Schwalbe, H.; Corzilius, B. Heteronuclear Cross-Relaxation under Solid-State Dynamic Nuclear Polarization. *J. Am. Chem. Soc.* **2016,** *138,* 16572-16575.
19. Hoff, D. E.; Albert, B. J.; Saliba, E. P.; Scott, F. J.; Choi, E. J.; Mardini, M.; Barnes, A. B. Frequency Swept Microwaves for Hyperfine Decoupling and Time Domain Dynamic Nuclear Polarization. *Solid State Nucl. Magn. Reson.* **2015,** *72,* 79-89.
20. Cheng, C. Y.; Han, S. I., Dynamic Nuclear Polarization Methods in Solids and Solutions to Explore Membrane Proteins and Membrane Systems. In *Annu. Rev. Phys. Chem.*, Johnson, M. A.; Martinez, T. J., Eds. Annual Reviews: Palo Alto, 2013; Vol. 64, pp 507-532.
21. Wang, T.; Park, Y. B.; Caporini, M. A.; Rosay, M.; Zhong, L. H.; Cosgrove, D. J.; Hong, M. Sensitivity-Enhanced Solid-State Nmr Detection of Expansin's Target in Plant Cell Walls. *Proc. Natl. Acad. Sci. U.S.A.* **2013,** *110,* 16444-16449.
22. Kobayashi, T.; Perras, F. A.; Slowing, I. I.; Sadow, A. D.; Pruski, M. Dynamic Nuclear Polarization Solid-State Nmr in Heterogeneous Catalysis Research. *ACS Catal.* **2015,** *5,* 7055-7062.
23. Kubicki, D. J.; Rossini, A. J.; Purea, A.; Zagdoun, A.; Ouari, O.; Tordo, P.; Engelke, F.; Lesage, A.; Emsley, L. Amplifying Dynamic Nuclear Polarization of Frozen Solutions by Incorporating Dielectric Particles. *J. Am. Chem. Soc.* **2014,** *136,* 15711-15718.
24. Rossini, A. J.; Widdifield, C. M.; Zagdoun, A.; Lelli, M.; Schwarzwalder, M.; Coperet, C.; Lesage, A.; Emsley, L. Dynamic Nuclear Polarization Enhanced Nmr Spectroscopy for Pharmaceutical Formulations. *J. Am. Chem. Soc.* **2014,** *136,* 2324-2334.
25. Mak-Jurkauskas, M. L.; Bajaj, V. S.; Hornstein, M. K.; Belenky, M.; Griffin, R. G.; Herzfeld, J. Gradual Winding of the Bacteriorhodopsin Chromophore in the First Half of Its Ion-Motive Photocycle: A Dynamic Nuclear Polarization Enhanced Solid State Nmr Study. *Proc. Natl. Acad. Sci. U. S. A.* **2008,** *105,* 883-888.
26. Mollica, G.; Dekhil, M.; Ziarelli, F.; Thureau, P.; Viel, S. Quantitative Structural Constraints for Organic Powders at Natural Isotopic Abundance Using Dynamic Nuclear Polarization Solid-State Nmr Spectroscopy. *Angew. Chem.-Int. Edit.* **2015,** *54,* 6028-6031.
27. Eva Pump; Jasmine Viger-Gravel; Edy Abou-Hamad; Manoja K. Samantaray; Bilel Hamzaoui; Andrei Gurinov; Dalaver H. Anjum; David Gajan; Anne Lesage; Anissa Bendjeriou-Sedjerari, et al. Reactive Surface Organometallic Complexes Observed Using Dynamic Nuclear Polarization Surface Enhanced Nmr Spectroscopy. *Chem. Sci.* **2017,** *8,* 284-290.
28. Märker, K.; Paul, S.; Fernández-de-Alba, C.; Lee, D.; Mouesca, J.-M.; Hedigerabc, S.; Paëpe*ab, G. D. Welcoming Natural Isotopic Abundance in Solid-State Nmr: Probing Π-Stacking and Supramolecular Structure of Organic Nanoassemblies Using Dnp. *Chem. Sci.* **2017**.
29. Ni, Q. Z.; Markhasin, E.; Can, T. V.; Corzilius, B.; Tan, K. O.; Barnes, A. B.; Daviso, E.; Su, Y.; Herzfeld, J.; Griffin, R. G. Peptide and Protein Dynamics and Low-Temperature/Dnp Magic Angle Spinning Nmr. *The Journal of Physical Chemistry B* **2017,** *121,* 4997-5006.
30. Veinberg, S. L.; Johnston, K. E.; Jaroszewicz, M. J.; Kispal, B. M.; Mireault, C. R.; Kobayashi, T.; Pruski, M.; Schurko, R. W. Natural Abundance N-14 and N-15 Solid-State Nmr of Pharmaceuticals and Their Polymorphs. *Phys. Chem. Chem. Phys.* **2016,** *18,* 17713-17730.
31. Elisei, E.; Filibian, M.; Carretta, P.; Colombo Serra, S.; Tedoldi, F.; Willart, J. F.; Descamps, M.; Cesaro, A. Dynamic Nuclear Polarization of a Glassy Matrix Prepared by

Solid State Mechanochemical Amorphization of Crystalline Substances. *Chem. Commun.* **2015,** *51,* 2080-2083.
32. Hirsh, D. A.; Rossini, A. J.; Emsley, L.; Schurko, R. W. Cl-35 Dynamic Nuclear Polarization Solid-State Nmr of Active Pharmaceutical Ingredients. *Phys. Chem. Chem. Phys.* **2016,** *18,* 25893-25904.
33. Märker, K.; Pingret, M.; Mouesca, J.-M.; Gasparutto, D.; Hediger, S.; De Paëpe, G. A New Tool for Nmr Crystallography: Complete 13c/15n Assignment of Organic Molecules at Natural Isotopic Abundance Using Dnp-Enhanced Solid-State Nmr. *J. Am. Chem. Soc.* **2015,** *137,* 13796-13799.
34. Le, D.; Casano, G.; Phan, T. N. T.; Ziarelli, F.; Ouari, O.; Aussenac, F.; Thureau, P.; Mollica, G.; Gigmes, D.; Tordo, P., et al. Optimizing Sample Preparation Methods for Dynamic Nuclear Polarization Solid-State Nmr of Synthetic Polymers. *Macromolecules* **2014,** *47,* 3909-3916.
35. Ong, T. C.; Mak-Jurkauskas, M. L.; Walish, J. J.; Michaelis, V. K.; Corzilius, B.; Smith, A. A.; Clausen, A. M.; Cheetham, J. C.; Swager, T. M.; Griffin, R. G. Solvent-Free Dynamic Nuclear Polarization of Amorphous and Crystalline Ortho-Terphenyl. *J. Phys. Chem. B* **2013,** *117,* 3040-3046.
36. Pinon, A. C.; Rossini, A. J.; Widdifield, C. M.; Gajan, D.; Emsley, L. Polymorphs of Theophylline Characterized by Dnp Enhanced Solid-State Nmr. *Mol. Pharmaceutics* **2015,** *12,* 4146-4153.
37. Afeworki, M.; Schaefer, J. Mechanism of Dnp-Enhanced Polarization Transfer across the Interface of Polycarbonate Polystyrene Heterogeneous Blends. *Macromolecules* **1992,** *25,* 4092-4096.
38. Yihong Qiu, Y. C., Geoff G.Z. Zhang, *Developing Solid Oral Dosage Forms: Pharmaceutical Theory and Practice.* Elsevier Science Bv: Amsterdam, 2009; p 1-943.
39. Song, C.; Hu, K.-N.; Joo, C.-G.; Swager, T. M.; Griffin, R. G. Totapol: A Biradical Polarizing Agent for Dynamic Nuclear Polarization Experiments in Aqueous Media. *Journal of the American Chemical Society* **2006,** *128,* 11385-11390.
40. Sauvee, C.; Rosay, M.; Casano, G.; Aussenac, F.; Weber, R. T.; Ouari, O.; Tordo, P. Highly Efficient, Water-Soluble Polarizing Agents for Dynamic Nuclear Polarization at High Frequency. *Angew. Chem.-Int. Edit.* **2013,** *52,* 10858-10861.
41. Yang, F.; Su, Y.; Zhang, J.; DiNunzio, J.; Leone, A.; Huang, C.; Brown, C. D. Rheology Guided Rational Selection of Processing Temperature to Prepare Copovidone-Nifedipine Amorphous Solid Dispersions Via Hot Melt Extrusion (Hme). *Mol. Pharm.* **2016,** *13,* 3494-3505.
42. Yang, F.; Su, Y.; Zhu, L.; Brown, C. D.; Rosen, L. A.; Rosenberg, K. J. Rheological and Solid-State Nmr Assessments of Copovidone/Clotrimazole Model Solid Dispersions. *Int. J. Pharm.* **2016,** *500,* 20-31.
43. Barnes, A. B.; Nanni, E. A.; Herzfeld, J.; Griffin, R. G.; Temkin, R. J. A 250 Ghz Gyrotron with a 3 Ghz Tuning Bandwidth for Dynamic Nuclear Polarization. *J. Magn. Reson.* **2012,** *221,* 147-153.
44. Bajaj, V. S.; Farrar, C. T.; Hornstein, M. K.; Mastovsky, I.; Vieregg, J.; Bryant, J.; Elena, B.; Kreischer, K. E.; Temkin, R. J.; Griffin, R. G. Dynamic Nuclear Polarization at 9t Using a Novel 250 Ghz Gyrotron Microwave Source. 2003. *J. Magn. Reson.* **2011,** *213,* 404-409.
45. Barnes, A. B.; Mak-Jurkauskas, M. L.; Matsuki, Y.; Bajaj, V. S.; van der Wel, P. C. A.; DeRocher, R.; Bryant, J.; Sirigiri, J. R.; Temkin, R. J.; Lugtenburg, J., et al. Cryogenic Sample Exchange Nmr Probe for Magic Angle Spinning Dynamic Nuclear Polarization. *J. Magn. Reson.* **2009,** *198,* 261-270.

46. Thurber, K. R.; Tycko, R. Measurement of Sample Temperatures under Magic-Angle Spinning from the Chemical Shift and Spin-Lattice Relaxation Rate of Br-79 in Kbr Powder. *J. Magn. Reson.* **2009,** *196,* 84-87.
47. Mance, D.; Gast, P.; Huber, M.; Baldus, M.; Ivanov, K. L. The Magnetic Field Dependence of Cross-Effect Dynamic Nuclear Polarization under Magic Angle Spinning. *J. Chem. Phys.* **2015,** *142,* 10.
48. Yuan, X.; Sperger, D.; Munson, E. J. Investigating Miscibility and Molecular Mobility of Nifedipine-Pvp Amorphous Solid Dispersions Using Solid-State Nmr Spectroscopy. *Mol. Pharm.* **2014,** *11,* 329-337.
49. Takahashi, H.; Fernández-de-Alba, C.; Lee, D.; Maurel, V.; Gambarelli, S.; Bardet, M.; Hediger, S.; Barra, A.-L.; De Paëpe, G. Optimization of an Absolute Sensitivity in a Glassy Matrix During Dnp-Enhanced Multidimensional Solid-State Nmr Experiments. *J. Magn. Reson.* **2014,** *239,* 91-99.
50. Hu, K.-N.; Song, C.; Yu, H.-h.; Swager, T. M.; Griffin, R. G. High-Frequency Dynamic Nuclear Polarization Using Biradicals: A Multifrequency Epr Lineshape Analysis. *J. Chem. Phys.* **2008,** *128,* 052321.
51. Hu, K.-N.; Yu, H.-h.; Swager, T. M.; Griffin, R. G. Dynamic Nuclear Polarization with Biradicals. *J. Am. Chem. Soc.* **2004,** *126,* 10844-10845.
52. Akbey, Ü.; Franks, W. T.; Linden, A.; Lange, S.; Griffin, R. G.; Rossum, B.-J. v.; Oschkinat, H. Dynamic Nuclear Polarization of Deuterated Proteins. *Angew. Chem.-Int. Edit.* **2010,** *49,* 7803-7806.
53. Rosay, M.; Weis, V.; Kreischer, K. E.; Temkin, R. J.; Griffin, R. G. Two-Dimensional C-13-C-13 Correlation Spectroscopy with Magic Angle Spinning and Dynamic Nuclear Polarization. *J. Am. Chem. Soc.* **2002,** *124,* 3214-3215.
54. Liao, S. Y.; Lee, M.; Wang, T.; Sergeyev, I. V.; Hong, M. Efficient Dnp Nmr of Membrane Proteins: Sample Preparation Protocols, Sensitivity, and Radical Location. *J. Biomol. NMR* **2016,** *64,* 223-237.
55. Kiswandhi, A.; Lama, B.; Niedbalski, P.; Goderya, M.; Long, J.; Lumata, L. The Effect of Glassing Solvent Deuteration and Gd3+ Doping on C-13 Dnp at 5 T. *RSC Adv.* **2016,** *6,* 38855-38860.
56. Perras, F. A.; Reinig, R. R.; Slowing, I. I.; Sadow, A. D.; Pruski, M. Effects of Biradical Deuteration on the Performance of Dnp: Towards Better Performing Polarizing Agents. *Phys. Chem. Chem. Phys.* **2016,** *18,* 65-69.
57. Lumata, L.; Merritt, M. E.; Kovacs, Z. Influence of Deuteration in the Glassing Matrix on 13c Dynamic Nuclear Polarization. *Phys. Chem. Chem. Phys.* **2013,** *15,* 7032-7035.
58. Bouleau, E.; Saint-Bonnet, P.; Mentink-Vigier, F.; Takahashi, H.; Jacquot, J.-F.; Bardet, M.; Aussenac, F.; Purea, A.; Engelke, F.; Hediger, S., et al. Pushing Nmr Sensitivity Limits Using Dynamic Nuclear Polarization with Closed-Loop Cryogenic Helium Sample Spinning. *Chem. Sci.* **2015,** *6.*
59. Mittapalli, S.; Mannava, M. K. C.; Khandavilli, U. B. R.; Allu, S.; Nangia, A. Soluble Salts and Cocrystals of Clotrimazole. *Cryst. Growth Des.* **2015,** *15,* 2493-2504.
60. Lesage, A.; Bardet, M.; Emsley, L. Through-Bond Carbon−Carbon Connectivities in Disordered Solids by Nmr. *J. Am. Chem. Soc.* **1999,** *121,* 10987-10993.
61. Cadars, S.; Sein, J.; Duma, L.; Lesage, A.; Pham, T. N.; Baltisberger, J. H.; Brown, S. P.; Emsley, L. The Refocused Inadequate Mas Nmr Experiment in Multiple Spin-Systems: Interpreting Observed Correlation Peaks and Optimising Lineshapes. *Journal of Magnetic Resonance* **2007,** *188,* 24-34.
62. Zhong, W.; Yang, X.; Tong, W.; Martin, G. E. Structural Characterization of a Novel Degradant of the Antifungal Agent Posaconazole. *J. Pharm. Biomed. Anal.* **2012,** *66,* 40-49.
63. Hilton, B. D.; Feng, W. Q.; Martin, G. E. Assignment of the N-15 Resonances of the Antifungal Agent Posaconazole. *J. Heterocycl. Chem.* **2011,** *48,* 948-951.

64. Hu, K. N.; Song, C.; Yu, H. H.; Swager, T. M.; Griffin, R. G. High-Frequency Dynamic Nuclear Polarization Using Biradicals: A Multifrequency Epr Lineshape Analysis. *J. Chem. Phys.* **2008,** *128,* 052302.
65. Chaudhari, S. R.; Berruyer, P.; Gajan, D.; Reiter, C.; Engelke, F.; Silverio, D. L.; Coperet, C.; Lelli, M.; Lesage, A.; Emsley, L. Dynamic Nuclear Polarization at 40 Khz Magic Angle Spinning. *Phys. Chem. Chem. Phys.* **2016,** *18,* 10616-10622.